AD-755 172

TRANSITION FROM DEFLAGRATION TO DETONATION IN GRANULAR EXPLOSIVES

Richard R. Bernecker, et al

Naval Ordnance Laboratory
White Oak, Maryland

13 December 1972

DISTRIBUTED BY:

NTIS

National Technical Information Service
U. S. DEPARTMENT OF COMMERCE
5285 Port Royal Road, Springfield Va. 22151

NOLTR 72-202

AD755172

TRANSITION FROM DEFLAGRATION TO DETONATION IN GRANULAR EXPLOSIVES

By
Richard R. Bernecker
Donna Price

13 DECEMBER 1972

D D C
FEB 9 1973
C

NOL

NAVAL ORDNANCE LABORATORY, WHITE OAK, SILVER SPRING, MARYLAND

NATIONAL TECHNICAL
INFORMATION SERVICE

APPROVED FOR PUBLIC RELEASE;
DISTRIBUTION UNLIMITED

NOLTR 72-202

125
R

UNCLASSIFIED
Security Classification

DOCUMENT CONTROL DATA - R & D

(Security classification of title, body of abstract and indexing annotation must be entered when the overall report is classified)

1. ORIGINATING ACTIVITY *(Corporate author)* Naval Ordnance Laboratory White Oak, Silver Spring, Maryland	2a. REPORT SECURITY CLASSIFICATION UNCLASSIFIED 2b. GROUP

3. REPORT TITLE

TRANSITION FROM DEFLAGRATION TO DETONATION IN GRANULAR EXPLOSIVES

4. DESCRIPTIVE NOTES *(Type of report and inclusive dates)*

5. AUTHOR(S) *(First name, middle initial, last name)*

Richard R. Bernecker and Donna Price

6. REPORT DATE	7a. TOTAL NO. OF PAGES	7b. NO. OF REFS
13 December 1972	115	31

8a. CONTRACT OR GRANT NO. b. PROJECT NO. MAT-03L-000/R011-01-01 c. d.	9a. ORIGINATOR'S REPORT NUMBER(S) NOLTR 72-202 9b. OTHER REPORT NO(S) *(Any other numbers that may be assigned this report)*

10. DISTRIBUTION STATEMENT

Approved for public release; distribution unlimited.

11. SUPPLEMENTARY NOTES	12. SPONSORING MILITARY ACTIVITY Naval Material Command

13. ABSTRACT

Deflagration to detonation transition (DDT) has been observed for 91/9 RDX/Wax over the range of 67 - 95% TMD. The initial process monitored was the propagation of a convective flame front through the porous charge. Some time after that a postconvective front was formed; it traveled at a greater speed and overtook the convective front. About 10 - 20 μsec after this intersection and 10 - 20 mm beyond it, detonation appeared. Details of this proposed mechanism and their variation with compaction are fully described in the report. A few experiments at 70% TMD were also made on 97/3 and 94/6 RDX/Wax and on ammonium picrate. Only the latter failed to undergo a transition to detonation in the apparatus used.

Details of illustrations in this document may be better studied on microfiche

UNCLASSIFIED

Security Classification

14. KEY WORDS	LINK A ROLE	LINK A WT	LINK B ROLE	LINK B WT	LINK C ROLE	LINK C WT
DDT						
Transition phenomena						
Detonation						
RDX/Wax						
Explosive D						

Ib

DD FORM 1 NOV 65 1473 (BACK)

(PAGE 2)

UNCLASSIFIED

Security Classification

TRANSITION FROM DEFLAGRATION TO DETONATION IN GRANULAR EXPLOSIVES

By:

Richard R. Bernecker and Donna Price

ABSTRACT: Deflagration to detonation transition (DDT) has been observed for 91/9 RDX/Wax over the range of 67 - 95% TMD. The initial process monitored was the propagation of a convective flame front through the porous charge. Some time after that a postconvective front was formed; it traveled at a greater speed and overtook the convective front. About 10 - 20 μsec after this intersection and 10 - 20 mm beyond it, detonation appeared. Details of this proposed mechanism and their variation with compaction are fully described in the report. A few experiments at 70% TMD were also made on 97/3 and 94/6 RDX/Wax and on ammonium picrate. Only the latter failed to undergo a transition to detonation in the apparatus used.

Approved by: J. C. Dacons, Acting Chief
ADVANCED CHEMISTRY DIVISION
CHEMISTRY RESEARCH DEPARTMENT
NAVAL ORDNANCE LABORATORY
Silver Spring, Maryland 20910

TRANSITION FROM DEFLAGRATION TO DETONATION IN GRANULAR EXPLOSIVES

This work was carried out under tasks MAT-03L-000/R011-01-01, IR-159 and ORDTASK ORD-332-004/UF00-354-314. The present results and conclusions on the transition from burning to detonation of granular explosives should be of interest in the area of explosive sensitivity especially as related to the problem of premature initiation.

ROBERT WILLIAMSON II
Captain, USN
Commander

Albert Lightbody
ALBERT LIGHTBODY
By direction

TABLE OF CONTENTS

		Page
I.	INTRODUCTION	1
II.	EXPERIMENTAL ARRANGEMENT AND PROCEDURE	
	A. DDT Tube	2
	B. Ignitor	2
	C. Explosive Materials	4
	D. Charge Loading	4
	E. Ionization Pins	5
	F. Strain Gages and Their Usage	5
	G. Instrumentation (General)	6
III.	EXPERIMENTAL RESULTS	
	A. Treatment of Experimental Results	7
	B. Detailed Experimental Results and Discussion of Each Shot	9
	1) Ammonium Picrate (Explosive D)	9
	2) RDX/Wax Series	14
	a) 91/9 RDX/Wax	14
	b) 94/6 RDX/Wax	42
	c) 97/3 RDX/Wax	42
IV.	DISCUSSION	
	A. Effect of Compaction in 91/9 RDX/Wax Mixture	44
	1) Convective Flame Front	44
	2) Detonation Velocity	50
	3) Time to Detonation	52
	4) Postconvective Wave	53
	5) Predetonation Column Length	58
	6) Rating for Sensitivity to DDT	62
	B. DDT Behavior for RDX/Wax Series at 70% TMD and for Ammonium Picrate	64
	C. DDT Mechanisms	
	1) DDT Mechanism for 91/9 RDX/Wax	65
	2) DDT Mechanisms for Explosives	67
V.	SUMMARY AND CONCLUSIONS	70
VI.	ACKNOWLEDGMENT	72
	REFERENCES	73
	GLOSSARY	75

TABLE OF CONTENTS, Cont'd.

Page

APPENDICES

A. Internal Pressure-Strain Calibration of DDT Tubes 77
B. Compilation of Supplementary Experimental Data 92
C. Permeability Measurements of Granular Explosives 108

ILLUSTRATIONS

Figure	Title	Page
1	DDT Tube with Bottom Closure	3
2	Tube Fragments Recovered from Ammonium Picrate Experiments	10
3	Distance-Time Data for 90.1% TMD Ammonium Picrate (Shot 226)	12
4	Strain Gage Voltage-Time Curves for 90.1% TMD Ammonium Picrate (Shot 226)	12
5	Distance-Time Data for 85.5% TMD 91/9 RDX/Wax (Shot 306)	17
6	Strain Gage Voltage-Time Curves for 85.5% TMD 91/9 RDX/Wax (Shot 306)	17
7	Oscilloscope Record for 85.5% TMD 91/9 RDX/Wax (Shot 306)	19
8	Oscilloscope Record for 90.1% TMD 91/9 RDX/Wax (Shot 305)	19
9	Distance-Time Data for 90.1% TMD 91/9 RDX/Wax (Shot 215)	21
10	Distance-Time Data for 90.1% TMD 91/9 RDX/Wax (Shot 305)	21
11	Strain Gage Voltage-Time Curves for 90.1% TMD 91/9 RDX/Wax (Shot 305)	21
12	Tube Fragments Recovered from 94.5% TMD 91/9 RDX/Wax Experiments	24
13	Distance-Time Data for 94.5% TMD 91/9 RDX/Wax (Shot 304)	25
14	Strain Gage Voltage-Time Curves for 94.5% TMD 91/9 RDX/Wax (Shot 304)	25
15	Strain Gage Voltage-Time Curves (Extended) for 94.5% TMD 91/9 RDX/Wax (Shot 304)	25
16	Distance-Time Data for 94.5% TMD 91/9 RDX/Wax (Shot 222)	29
17	Strain Gage Voltage-Time Curves for 94.5% TMD 91/9 RDX/Wax (Shot 222)	29

TABLE OF CONTENTS, Cont'd.

Figure	Title	Page
18	Distance-Time Data for 92.3% TMD 91/9 RDX/Wax (Shot 316)	30
19	Strain Gage Voltage-Time Curves for 92.3% TMD 91/9 RDX/Wax (Shot 316)	30
20	Distance-Time Data for 81.0% TMD 91/9 RDX/Wax (Shot 220)	32
21	Distance-Time Data for 81.0% TMD 91/9 RDX/Wax (Shot 317)	32
22	Strain Gage Voltage-Time Curves for 81.0% TMD 91/9 RDX/Wax (Shot 317)	32
23	Distance-Time Data for 78.8% TMD 91/9 RDX/Wax (Shot 315)	35
24	Strain Gage Voltage-Time Curves for 78.8% TMD 91/9 RDX/Wax (Shot 315)	35
25	Distance-Time Data for 76.5% TMD 91/9 RDX/Wax (Shot 312)	36
26	Strain Gage Voltage-Time Curves for 76.5% TMD 91/9 RDX/Wax (Shot 312)	36
27	Distance-Time Data for 74.3% TMD 91/9 RDX/Wax (Shot 307)	37
28	Strain Gage Voltage-Time Curves for 74.3% TMD 91/9 RDX/Wax (Shot 307)	37
29	Distance-Time Data for 74.3% TMD 91/9 RDX/Wax (Shot 224)	39
30	Tube Fragments Recovered from 74.3% TMD 91/9 RDX/Wax Experiments	39
31	Distance-Time Data for 69.8% TMD 91/9 RDX/Wax (Shot 225)	41
32	Strain Gage Voltage-Time Curves for 69.8% TMD 91/9 RDX/Wax (Shot 225)	41
33	Distance-Time Data for 70.3% TMD 94/6 RDX/Wax (Shot 214)	43
34	Distance-Time Data for 70.9% TMD 97/3 RDX/Wax (Shot 218)	43
35	Convective Front Velocity as a Function of Density for 91/9 RDX/Wax Mixture	45
36	Effect of Compaction on Permeability Coefficient for PETN	45
37	Detonation Velocity of 91/9 RDX/Wax as Function of Compaction	51
38	Time to Detonation and Relative Time to Detonation for 91/9 RDX/Wax as Function of Compaction	51
39	Postconvective Wave Velocity for 91/9 RDX/Wax as Function of Compaction	55
40	Longitudinal Sound Velocity for Various Explosives as Function of Compaction	55

TABLE OF CONTENTS, Cont'd.

Figure	Title	Page
41	Time Interval between Passage of Convective Front and PC Front, t_E, for 91/9 RDX/Wax as Function of Compaction for Locations at 41 mm and 80 mm	59
42	Time Interval between Passage of Convective Front and PC Front, t_E, for 91/9 RDX/Wax as Function of Compaction for $x = \ell/2$ Location	59
43	Predetonation Column Length for 91/9 RDX/Wax as a Function of Compaction	60
44	Proposed DDT Mechanism for 91/9 RDX/Wax Granular Charge	66
45	Effect of Compaction on DDT Parameters for 91/9 RDX/Wax	71
A1	Cross Section of Pressurized Cylindrical Tube	78
A2	The Wheatstone Bridge Circuit Schematic	78
A3	The Potentiometric Circuit Schematic	78
A4	Strain Gage Calibrations of DDT Tube	91
B1	Particle Size Distribution of RDX(X597)	93
B2	Strain Gage Voltage-Distance Data for 85.5% TMD 91/9 RDX/Wax (Shot 306)	94
B3	Strain Gage Voltage-Distance Data for 78.8% TMD 91/9 RDX/Wax (Shot 315)	94
B4	Strain Gage Voltage-Distance Data for 76.5% TMD 91/9 RDX/Wax (Shot 312)	95
B5	Strain Gage Voltage-Distance Data for 74.3% TMD 91/9 RDX/Wax (Shot 307)	95
B6	Strain Gage Voltage-Distance Data for 69.8% TMD 91/9 RDX/Wax (Shot 225)	95
B7	Variation of $(dE/dt)_Y$ Near Front of Postconvective Wave as Function of Compaction	97

Table	Title	Page
1	Summary of Ionization Probe Distance-Time Data for RDX/Wax Series	15
2	Summary of Postconvective Wave Velocities and Estimated Longitudinal Sound Velocities for 91/9 RDX/Wax	54
A-1	Calculated Strain Gage Sensitivity Factor for DDT Tube Used in Earlier NOL Work	83
A-2	Comparison of Experimental and Calculated Strain Gage Voltage Output for DDT Tube Used in Earlier NOL Work	86
A-3	Calculated Calibration Data for Internal Pressure Loading of Present DDT Tube	90

TABLE OF CONTENTS, Cont'd.

Table	Title	Page
B-1	Compilation of Distance-Time Data for 91/9 RDX/Wax ...	98
B-2	Compilation of Distance-Time Data for Miscellaneous Explosives	102
B-3	Particle Size Analysis of RDX(X597)	103
B-4	Measurements of Outer Diameter of Recovered DDT Tube (Ignitor End)	104
B-5	Measured Values of dE/dt Associated with the Front of the PC Wave for 91/9 RDX/Wax	105
B-6	Time Interval Between Passage of Convective Front and PC Wave at Various Locations for 91/9 RDX/Wax	107
C-1	Dependence of Permeability Coefficient on Compaction (16)	109
C-2	Permeability Coefficients for Miscellaneous Explosives (27)	113
C-3	Permeability Coefficients for Miscellaneous Explosives (7)	114

TRANSITION FROM DEFLAGRATION TO DETONATION IN GRANULAR EXPLOSIVES

I. INTRODUCTION

The ability of an explosive to undergo a transition to detonation from a purely burning mode is a fundamental and important characteristic of the explosive. The deflagration to detonation transition (abbreviated as DDT) was studied in detail for cast, shock-sensitive explosives some years ago at NOL (1-3). In these DDT studies, the sequence of events begins with mild thermal ignition of the explosive charge at one end of a closed tube. [The ignitor end (closed end) is called the near end of the tube for reference and any transition to detonation occurs beyond the near end of the tube]*. It was realized early in the work on DDT that containment of any combustion gases is a necessary but not sufficient requirement for a transition to detonation to occur for secondary explosives (1,4).

In the DDT studies for cast explosives, a model was successfully developed based on a mechanism which consisted of two distinct processes (1-3). Firstly, there must be a sufficiently rapid pressure increase in the ignition region to produce an incipient shock wave at some point beyond the ignition region. Secondly, the unburned explosive beyond the burning region must be sufficiently shock sensitive to be initiated by a shock wave equal in amplitude to the high pressure achieved in the burning region. In the case of porous explosives, preliminary experiments by Griffiths and Groocock (5) revealed that there is an additional heat transfer mode which may affect the transfer of energy from the ignition area into the unburned explosive. This mode was called convective burning and it depends in part on the permeability of the explosive charge. Thus, pores which are interconnected form a path allowing the penetration of hot combustion gases from the ignition region deep into the unburned explosive charge. Griffiths and Groocock observed optically the propagation of a convective flame front at a rate of about 1 mm/μsec for some distance within the charge before the formation of a detonation front. Consequently, there is a burning bed of explosive particles near the ignitor and it is possible for a retonation wave, as shown by Griffiths and Groocock, to travel backward toward the ignitor through this burning bed. Andreev long ago had postulated that penetration of hot combustion gases into the pores of the unburned explosive could lead to DDT (6). However, Andreev did not postulate the propagation of a convective front. Once ignition occurred within the pores, he assumed that a detonation wave

- - - - - - - - - - - - - - - - - - -

*The terminology "upstream" (and downstream) might be more succinct but has been used in opposite senses in the field of hydrodynamics. Therefore, such terminology will be avoided in the report.

would form a short distance beyond the point of inner pore ignition. However, the optical records of Griffiths and Groocock showed that the onset of detonation was some distance beyond the point at which convective burning began. Moreover, their experimental results raised the question as to the role convective burning plays in the DDT mechanism(s) for porous explosives.

The objectives of the present study are 1) to characterize the nature of any reaction fronts observed in the predetonation section of the explosive charge; 2) to attempt to deduce information about the DDT mechanism(s) in porous explosive charges from the experimental results; and 3) to observe whether transitions from burning to detonation could occur in certain relatively shock-insensitive explosives in the current experimental configuration.

II. EXPERIMENTAL ARRANGEMENT AND PROCEDURE

A. DDT Tube

The DDT tube is similar to that used in earlier work at this Laboratory (1,3); a schematic diagram of the tube is shown in Fig. 1. The main body is commercial seamless carbon mechanical steel (e.g. AISI 1015). The average tensile strength and yield strength quoted for this material by the supplier were 80,000 psi and 65,000 psi, respectively. The ultimate tensile strength was quoted as approximately 90,000 psi.

The inner and outer diameters of the tube were selected in order that 1) the wall thickness be sufficiently great to maintain the high gas pressure generated in the ignitor region during experiments using charges with very low permeability and 2) the inner diameter be sufficiently large so that any diameter effect on convective burning (7) would be negligible and that the critical diameter for detonation (8) would be exceeded for most explosives of interest. The ID and OD of the tube were 16.27 ± 0.02 mm and 50.95 ± 0.03 mm, respectively. The overall tube length was 342.9 mm, but, because of the space occupied by the ignitor and ignitor bolt, the length of the explosive column was only 295.4 mm. A bottom closure assembly has been added to the DDT tube to prevent the flow of porous material from the tube during the predetonation period. The steel ignitor bolt had a cavity through which the ignitor leads were placed. Epoxy was used to eliminate all air pockets or channels at threaded surfaces and in the ignitor lead cavity. Epoxy was also used to provide a pressure seal around the ionization probes.

B. Ignitor

An ignitor was developed for this work to replace the single hot wire ignition system used in the earlier NOL work. The material selected was a mixture of boron and potassium nitrate (25/75) which is used frequently for ignition purposes. The adiabatic flame temperature for this mixture is 2810°K at 1000 psi.

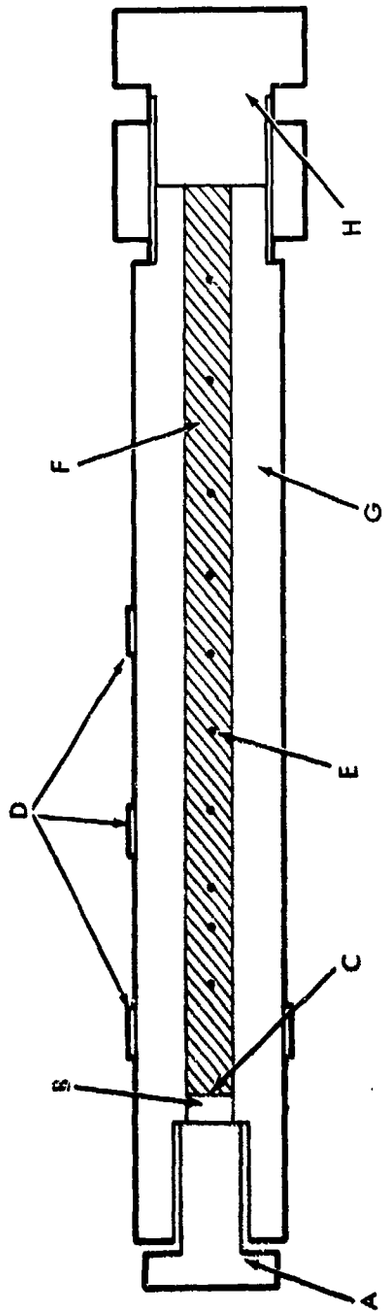

FIG. 1 DDT TUBE WITH BOTTOM CLOSURE.

(A - IGNITOR BOLT; B - IGNITOR; C - IGNITOR/EXPLOSIVE INTERFACE; D - STRAIN GAGES; E - IONIZATION PROBE LOCATION; F - EXPLOSIVE CHARGE; G - TUBE; H - BOTTOM CLOSURE)

The B/KNO_3 powder was mixed with a solvent (e.g., butyl acetate) to produce a thick paste which was loaded ("buttered") into the ignitor cup. The solvent was removed under vacuum with mild heating. A little over a third of a gram of B/KNO_3 was "buttered" over a 1 x 10 mil nichrome ribbon bridgewire (the depth of the ignition mixture was 6.3 mm). Approximately 30 volts (DC) were used to actuate the ignitor. The ignition cup was made from a thermally resistant plastic and was recovered intact after the shot in most instances.

C. Explosive Materials

1) Ammonium picrate

The ammonium picrate (Explosive D) was taken from a commercial lot of Explosive D (labelled X-720), which had a weight mean average particle size of 285μ.

2) RDX/Wax Series

a) 91/9 RDX/Wax

A large (10 kg) batch of 91/9 RDX/Wax was blended from a Class A RDX (X-597) and carnauba wax (N-134). The mixture (X-764) was prepared in a 30 gallon barrel blender using golf balls to provide some milling action during the tumbling process. The weight mean particle size of the wax was about 125μ while that of the RDX was about 200μ (see Appendix B for particle size analysis of the RDX material).

b) 94/6 and 97/3 RDX/Wax

Smaller size lots (1 kg per lot) of 94/6 and 97/3 RDX/Wax were prepared from the same RDX and carnauba wax described above. The mixtures were prepared in a chevron blender with golf balls. The 94/6 and 97/3 RDX/Wax mixtures were designated as X-759 and X-758, respectively.

D. Charge Loading

A special pressing assembly was built to produce high density charges in the DDT tube configuration. The assembly consisted of a combination tube holder and ram guide, the ram, and its retainer. The assembly was mounted on a 300 ton hydraulic press which provided adequate clearance for tube loading without disturbing the original tube position. Increments were loaded in the DDT tube by weighing a precise amount of explosive into the tube and pressing to a known thickness (12.70 mm) using external stops. The length to diameter ratio of an increment (12.7/16.27), therefore, was less than 1. All DDT tubes were x-rayed after loading and before instrumenting.

At low densities (less than 1.25 g/cc), the DDT tubes can be handpacked and this procedure was followed in several early experiments.

However, it must be noted that different permeabilities might be expected for the different preparations since the application of force is continuous in one case (with the 300 ton press) and discontinuous in the other case (handpacking).

E. Ionization Pins

Two types of ionization pins were used in this work. The first type was a commercial style used in regular detonation velocity measurements (Model CA-1040 made by EG and G*). However, the initial reaction front did not consistently trigger the first pin (i.e., pin closest to the ignitor) when a commercial ionization probe (IP) was used. Consequently, a custom made IP was fabricated from copper tubing (ID of 0.686 mm, OD of 0.813 mm--the latter is the same as the EG and G pins) and No. 24 Formvar coated copper wire (inner conductor). The smaller separation between the inner conductor and the sheath (about 0.05 mm for NOL pins vs 0.25 for EG and G pins) resulted in IPs which were more sensitive to flame fronts or weakly ionized gases. Consequently, the custom-made NOL IPs were used in the two IP holes closest to the ignitor while EG and G pins were used in the subsequent eight holes. The pins were spiralled along the charge length to reduce weakening the tube walls which must undergo gas loading during the DDT buildup period. The depth of the IPs into the charge (6.1 mm) was designed to yield velocity data near the axis of the charge and to avoid triggering of IPs by potential "flashdown" between the charge and tube walls in the more porous charges.

F. Strain Gages and their Usage

The strain gages are the same type used previously (31), i.e., BLH Electronics** Model C-14. Their resistance is nominally 2000 $\pm$ 10 ohms and their gage factor (9) (see Appendix A) is normally 3.4 to 3.5 in. ohm/ in. ohm. The dimension of the wire grid along the x coordinate (tube axis in our experiments) is 10.4 $\pm$ 0.2 mm.

The strain gages attached to the DDT tube were intended to monitor pressure buildup as previously done (1,3) and also to indicate, perhaps, the propagation of compressive waves within the explosive charge. Our strain gages, with their rather large cross section (i.e. 10.4 mm), are limited in their capacity to yield precision shock velocity data. However, the facts that 1) they can be mounted externally very easily (thus eliminating exposure to hot combustion gases) and 2) are relatively inexpensive led to their use as pseudo-velocity gages.

A recent publication (10) indicates that the head of convective flame front will have an average pressure of between 0.1 and 1.0 kbar

- - - - - - - - - - - - - - - - - - -

*EG and G, Inc., Santa Barbara Division, Goleta, California.

**BLH Electronics, Inc., Waltham, Mass.

associated with it, depending upon various factors such as convective rate, pore size, charge length, etc. Based upon a theoretically computed strain gage (SG) calibration of the present DDT tube (see Appendix A), we should expect between 1 and 6 millivolts output associated with the passage of such a flame front. However, the time-dependent elasticity effect (12) must be taken into account for both weak pressure fronts (flame fronts) and compressive waves*. By comparing the SG voltage output-time curves associated with known types of reaction fronts, we may be able to determine the characteristics expected for SG application under these rapid loading conditions. Consequently, our "a priori" knowledge of the type of strain gage E-t curves to anticipate during the passage of a front is rather limited. We do know from the earlier DDT work on cast explosives (1,3) that there is a rapid exponential increase in voltage (pressure) with time resulting from the generation of pressure in a confined linear (conductive) burning region. We can anticipate that this type of curve might be observed in our experiments with very low porosity (or high values of % TMD) charges.

G. Instrumentation (General)

1) Ionization Probe Control Box

The IP circuits consisted of 2 identical groups of capacitor discharge circuits which differed in the value of the discharging resistance. Thus, the ratios of discharge voltage of the first 5 circuits varied in the sequence of 3, 2, 1, 2.5, 1.5; the second group of 5 followed the same sequence. By using an A-B mode of an oscilloscope preamplifier, ten different coded discharges could be obtained on a single beam (3). The discharge voltage of the circuits was 28 v.

2) Strain Gage Circuits

Two different circuits were used to measure strain (pressure) along the DDT tube. A Wheatstone bridge circuit was used in the earlier work (3) to measure pressure increases in the ignition region of the tube; the same procedure was followed again. Two additional circuits were built following the potentiometric method (9) of measuring strain (see Appendix A for discussion of both Wheatstone and potentiometric circuits). The ballast resistance was 6000 Ω (i.e., three times the resistance of the strain gage). The input voltages for the three circuits were supplied by three separate regulated power supplies. The input voltages were set so that the resultant output, E, from each strain gage would represent the same amount of strain, ϵ (see Appendix A).

- - - - - - - - - - - - - - - - - - -

* Time-dependent elasticity results when the load (pressure) is applied suddenly. The resulting strain does not reach its maximum value instantaneously but approaches its final value exponentially (the departure from the baseline is approximately linear after the application of the load).

3) Oscilloscopes

The ionization probe signals were recorded on the upper beam of a Tektronix 551 dual beam oscilloscope while the output of the ignitor strain gage was recorded on the lower beam. Two 551 oscilloscopes were used because of triggering difficulties. Initially, one 551 scope (designated 551A) was triggered by the ignitor strain gage output on a 5 mv/cm sensitivity setting. The second 551 scope (designated 551B) was triggered by the discharge of the ionization probe closest to the ignitor; the sensitivity setting for the ignitor SG on this scope was 0.1 or 0.2 v/cm. The 551A scope did not trigger reproducibly. It either triggered prematurely because of extraneous noise or it triggered at the correct SG voltage setting but missed the first few IP discharges because of the low pressure associated with the initial reaction fronts emanating from the ignition region. Consequently, at times both 551 scopes were triggered by the IP closest to the ignitor.

The voltage outputs from strain gages positioned intermediate between the two ends of the tube but beyond the ignitor region were recorded on a Tektronix 454 oscilloscope operated in a chopped mode; this scope was triggered by the 551B oscilloscope.

III. EXPERIMENTAL RESULTS

A. Treatment of Experimental Data

1) Ionization Probes

The ionization probe discharges were recorded on the upper beams of the dual beam Tektronix 551 scopes as mentioned earlier. Because the IP discharges have both positive and negative displacements and only 4 vertical cm of the CRT was covered by the beam, sets of timing marks were placed on separate photos to avoid crowding and overlapping of IP and timing discharges. Time calibrations made before and after a shot were identical within experimental reading error so that in every other shot in a series, timing marks were taken only after a shot. The Polaroid records were read on a Universal telereader with a magnification factor of two. The timing marks (5, 10, or 50 μsec intervals) were fitted by least squares technique to an equation of the form

$$\text{Time} = aZ + bZ^2 + cZ^3 \qquad (1)$$

where a, b, c are least squares parameters
Z = counts of timing marks from the telereader.

When the time interval of interest covered only a small part of the total sweep time, "c" was set equal to zero. However, when the major part of the horizontal sweep time was used, a nonzero "c" value gave a better fit.

The subsequent position time graphs of the IP discharges indicated that the initial reaction front was accelerating. Consequently, the distance-time data for this front were fit to the equation

$$x_F = A + Bt + Ct^2 \tag{2}$$

where x_F = position of initial reaction front

using a least squares treatment again*. For the detonation front, the distance-time (x-t) data were fit to the equation

$$x_{DF} = F + Dt \tag{3}$$

where x_{DF} = position of the detonation front

The standard deviation of the overall fit of eqn. (2) to the experimental data was used to determine whether the x-t point just before detonation was consistent with the projected path of the initial reactive front. There were several occasions when this evaluation was helpful in interpreting the mechanism of transition to detonation (see text below). The rate of this first reactive front can be calculated at any time by differentiating eqn. (2) to yield

$$r_F = B + 2Ct = \frac{dx_F}{dt} \tag{4}$$

where B = rate at t = 0

2C = acceleration of front

In terms of x_F, we find that

$$r_F = [B^2 + 4C(x_F - A)]^{\frac{1}{2}} \tag{5}$$

For the detonation front, the overall fit of eqn. (3) was to determine whether the first x-t point of the detonation front should be used in measuring the steady-state detonation velocity (parameter D in eqn. (3)). Cases where there was some question about the classification of this point will be discussed later.

- - - - - - - - - - - - - - - - - - -

* The selection of eqn. (2) to fit the experimental x_F-t data was purely arbitrary. An exponential equation such as x_F = constant $\cdot$ e^{kt} was also tried but the fit of the data to the calculated exponential equation was much poorer than that to eqn. (2). The exponential equation was considered because it produces the relationship

$$dx_F/dt \propto x_F.$$

2) Strain Gages

The number of strain gages used in an experiment varied during the course of this work. The ignitor area strain gages (set of 2 used with the Wheatstone bridge) were always used and consistently positioned 20.3 ± 0.3 mm from the ignitor/explosive interface. The output from these strain gages was always recorded on the lower beams of the dual beam 551 scopes, although at different voltage sensitivities. In this manner the ignitor region strain (or pressure) is known unambigously relative to the IP x-t data (i.e., there was no question concerning the successful triggering of another oscilloscope used to record a strain gage (SG) output).

There is an unintentional feature of our experimental setup which allows cross checking of IP times with strain gage outputs from SGs beyond the ignition region. Namely, a small, variable (from experiment to experiment) voltage, ~ 20 mv, is superimposed on the SG records by the IP discharges*. Thus we could plot the IP x-t data using only the SG records as long as the SG output is on scale. In one case where the 551 scope sweep time was too short, we have gained additional information simply by analyzing the SG record which covered a longer time period. Using these superimposed signals, we can be certain that there was no premature or late triggering of the other SG scope (i.e., the Tektronix 454).

The voltage sensitivities of the SG oscilloscopes were determined by applying calibrated voltages to the oscilloscopes after a run. The time calibration was performed as described above (see "Ionization Probes").

B. Detailed Experimental Results and Discussion of Each Shot

1) Ammonium Picrate (Explosive D)

Two preliminary experiments were run with ammonium picrate, at 90.1% and 70.3% TMD. At the lower density (1.21 g/cc, Shot 217) a reaction front was observed only very close to the ignitor where the NOL IPs were located (the velocity for the 2.5 cm section was 0.11 mm/μsec). Other IPs (commercial design) beyond did not discharge even though the time scale was long enough for a 0.11 mm/μsec wave to reach at least four of these probes. A SG located 20 mm from the ignitor/explosive interface gave a nearly constant voltage of 1 mv throughout the observation period of 500 μsec. The recovered tube was intact except for the far end closure area (see Figure 2a). There was considerable plastic deformation of the tube walls in the ignitor region indicating that considerable internal pressure was generated before the tube ruptured at the far end closure (the weakest point of the tube).

- - - - - - - - - - - - - - - - - -

*This was also observed in the earlier work (15).

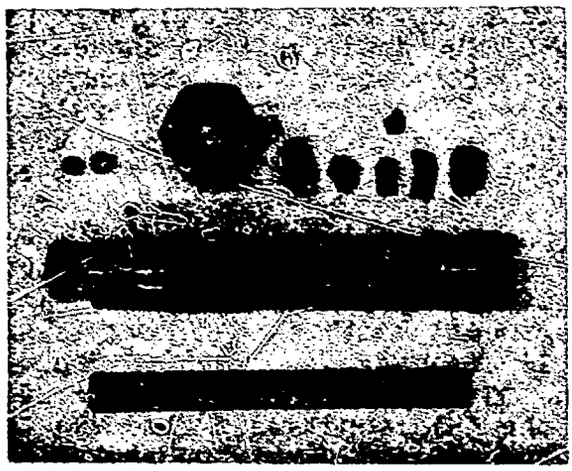

a

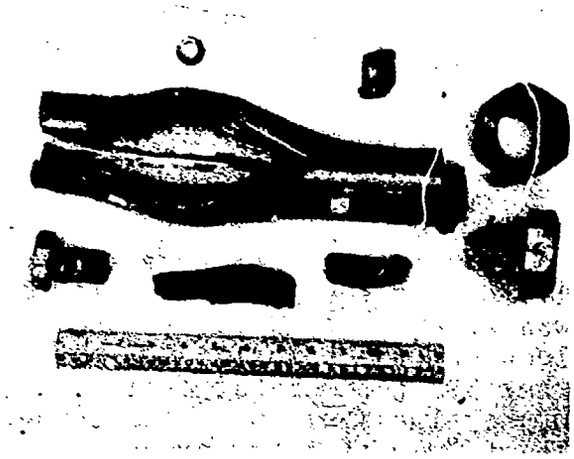

b

FIG. 2 TUBE FRAGMENTS RECOVERED FROM AMMONIUM PICRATE EXPERIMENTS.
a - 70.3% TMD CHARGE
b - 90.1% TMD CHARGE (IGNITION END AT LEFT IN PHOTOS)

The higher density experiment with ammonium picrate (ρ = 1.55 g/cc) yielded considerably more information about burning under confinement. Figure 3 shows the x-t data from the IPs while the SG voltage-time curves are shown in Figure 4. The recovered tube fragments are shown in Figure 2b and indicate that ammonium picrate did not undergo a transition to detonation at this density either. From Figure 2b we can see that the pressure buildup in the ignitor region is greater than that observed for the lower density (1.21 g/cc) since the tube walls have ruptured. However, a transition to detonation did not occur since the walls at the far end of the tube are largely intact. Hence, Figure 2b illustrates the type of behavior observed when a transition does not occur but when the pressure generated from confined burning exceeds the bursting pressure of the tube.

The above interpretation is consistent with the IP data of Figure 3 where we see an initially discontinuous reaction front. The reaction front for x > 130 mm* appears to be travelling at a near constant velocity of 0.58 mm/μsec. This velocity is definitely subsonic by a factor of 3 or 4 (see discussion in Section IVA4 of sound velocities in explosives) but is much faster than the velocity of a flame front (linear burning rate) where heat transfer is by conduction. The reaction front velocities, represented by the solid lines, in the ignitor region of the tube are 0.56 ± .01 mm/μsec, indicating that the same type of reaction front is observed throughout the tube but in a discontinuous manner**. The triangles shown in Figure 3 represent times at which there are marked changes in pressure at the strain gage locations at 20, 105, and 194 mm. In Figure 4, the SG located at 194 mm shows no voltage (pressure) increase until 475 μsec after the discharge of the ionization pin at 41.4 mm. After this interval, the voltage increases linearly but slowly with increasing time for 175 μsec. The same type of phenomenon is observed in the E-t curve for the 105 mm SG location except there are two times, 85 μsec and 290 μsec, at which the voltage increased suddenly. The first break at 85 μsec represents the first appearance of a pressure increase at the 105 mm location. The second pressure break at 280 μsec appears to be associated with the earlier part of the stable front detected downstream at x > 130 mm. The 20 mm SG location shows an initially decreasing E-t curve until 170 μsec. After this time the voltage increases linearly, as observed at the other SG locations, until a plateau is reached. A plateau appears to be reached at all SG locations although at different times (see discussion below).

- - - - - - - - - - - - - - - - - -

* As mentioned earlier, distance along the tube axis, x, is measured relative to the ignitor/explosive interface shown in Figure 1.

** Note that the NOL and the commercial IPs give the same velocity, well within experimental error (see Section IIE).

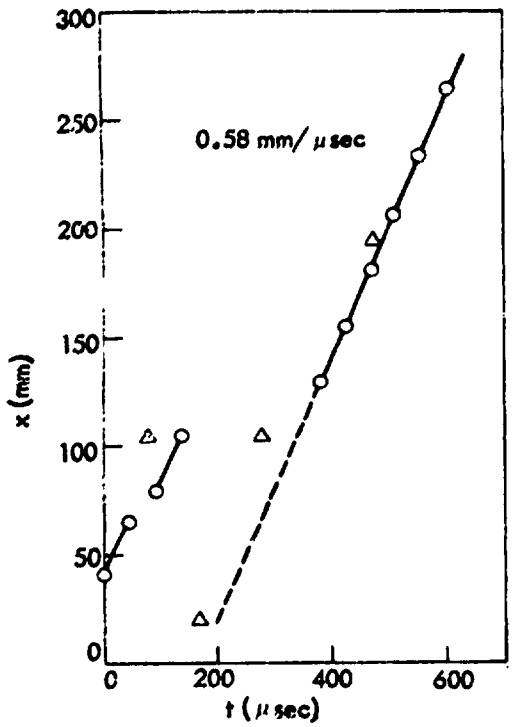

FIG. 3 DISTANCE - TIME DATA FOR 90.1% TMD AMMONIUM PICRATE (SHOT 226); DENSITY = 1.55 g/cc. (O IP DISCHARGE TIME; △ START OF SG VOLTAGE INCREASE)

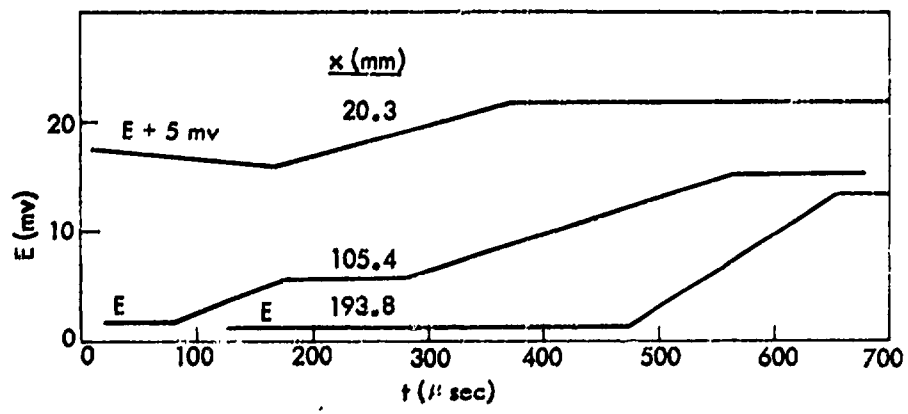

FIG. 4 STRAIN GAGE VOLTAGE - TIME CURVES FOR 90.1% TMD AMMONIUM PICRATE (SHOT 226); DENSITY = 1.55 g/cc.

When the IP and SG data in Figure 3 are analyzed jointly, it appears that the reaction front observed throughout the tube is a convective flame front. At 105 and 194 mm, we see that a slight increase in voltage (pressure) occurs before the passage of the reactive (convective) front. The pressure rise after the passage of the convective front is linear and mild. These features are consistent with the interpretation that the reactive front is a convective flame front. A convective flame front is an ignition wave which is propagated by the passage of hot combustion gases through the pores of the charge. The hot gases are forced into the pores because of confinement at the ignitor end of the tube. However, penetration of the gases into the charge does not result immediately in the formation of a convective flame front. The gases heat the pore walls and are consequently cooled themselves. It is the continuous flow of gases which raises the temperature of the pore walls until ignition in the pores occurs and produces what is now the head of the convective front. As a result of this process, we can expect that a strain gage at position x should record a pressure rise just before the flame front arrives at location x, as observed in Figure 3. From the SG measurements*, it appears that the convective front starts anew in the ignition region at least twice and the last time (dashed line followed by the solid line in Figure 3) is stable in its propagation.

There is a critical interplay between the pore distribution of the charge (characterized by permeability) and the gas pressure in the ignition region for convective burning. If the gas pressure is too low, convective burning does not occur (7) and the burning front is a conductive (linear) flame front. This conductive flame front is characterized by a very slow but complete consumption of the explosive in layers, in this case, perpendicular to the axis of the tube. The rate of conductive (linear) burning is less than 10^{-4} mm/μsec. Above a certain critical gas pressure in the ignition region, pore combustion commences (7). However, if the pressure in the ignition region is not maintained sufficiently long after the convective burning begins, it is conceivable that the convective front may cease to exist until adequately reinforced. The discontinuous nature of the convective front in Figure 3 suggests that at 90% TMD, we may be close to the convective combustion limit for our experimental arrangement. On the other hand, convective burning of ammonium picrate charges initially may be inherently unstable (16), due in part to the low adiabatic flame temperature of ammonium picrate, about 1790°K at 1000 psi. (It should be recalled that the IP data from the 70% TMD run discussed earlier also showed some peculiar behavior.)

- - - - - - - - - - - - - - - - - -

* In discussions concerning the arrival time of a reactive front at a SG location, we shall ignore the finite size of the SG and correlate the arrival time with the location at the center of the SG. In future work we hope to design experiments which will show the "effective" arrival time at a SG location (based on comparison of IP and SG data under "controlled" conditions).

By the time the convective flame front reaches the far end of the explosive charge, the gas pressure within the tube, as represented by the SG E-t curves in Figure 4, appears to be approximately independent of position along the tube axis. The 20 mm SG data show that pressure in the ignition region is approximately constant after 390 μsec. This may reflect a thermal transfer to the SG from the burning bed through the steel walls*. However, the data that we have concerning the thermal properties of the C-14 SG and the steel DDT tube indicate that a positive apparent strain should result from any heat transfer through the walls, a trend we do not observe. Consequently, the voltage plateaus seen in Figure 4 apparently are not the result of heat transfer to the SG and may be real effects arising from the convective burning phenomenon of ammonium picrate in our system. If the SGs register pressure effects only, it is evident that the entire tube became pressurized at about 2 kbar at approximately 650 μsec, that is when the convective flame front reached the end of the tube. The SG records also indicate the plastic flow leading to tube rupture (as shown in Figure 2b) started at about 900-950 μsec.

In summary, convective burning with its subsonic velocity has been observed at 90% TMD and probably at 70% TMD also. The pressure increase behind the convective front is mild and appears to reach a plateau (Figure 4). In the study of convective burning in propellant beds of cartridge charges for large gun ammunition (17), the pressure level behind the convective front appeared to be nearly constant along the length of the burning bed. However, the size of the bed particles was much larger and the porosity was much greater than in our 90% TMD ammonium picrate run. This plateau phenomenon deserves additional attention but at present is a minor point in the overall schedule of events in transitions to detonation as we shall see below. The principal observation from the ammonium picrate data is the absence of any large and rapid pressure increases, and the consequent absence of a transition to detonation. The presence of a precursor shock wave, required to initiate detonation, was not evident from either the IP or SG data.

2) RDX/Wax Series

a) 91/9 RDX/Wax

At present the custom blended 91/9 RDX/Wax mixture has been the most studied member of the RDX/Wax series. This mixture is one in a projected RDX/Wax series to study the DDT phenomena as the shock sensitivity of a composite explosive is reduced by increasing the wax content of the composite. The 91/9 RDX/Wax mixture has undergone transitions to detonation for densities ranging from 94.5 to 67.3% TMD. The ionization distance-time (x-t) data have been reduced according to eqns. (2) and (3) and the parameters as listed in Table 1. To present a more complete picture of DDT in

- - - - - - - - - - - - - - - - - - -

* See reference 9, p. 387 for a discussion of temperature effects on SG output.

TABLE 1

SUMMARY OF IONIZATION PROBE DISTANCE-TIME DATA FOR RDX/WAX SERIES

Shot No.	Density g/cc	Density %TMD	Convective Wave B[a] mm/μsec	Convective Wave 2Cx10^3[a] mm/μsec^2	ℓ cm	Detonation Parameters D mm/μsec	Detonation Parameters Δt_D[b] μsec	Detonation Parameters t_D[c] μsec
91/9 RDX/Wax (ρ_V = 1.68 g/cc)								
222	1.588	94.5	---[f]	---[f]		---[d]	---[d]	---[d]
304	1.588	94.5	1.51	0.0	15.5	8.40	77	104
316	1.551	92.3	0.95	0.0	14.5	7.68	100	145
215	1.513	90.1	0.57	5.1	12.5	7.93	91	201
305	1.513	90.1	0.59	3.8	12.0	7.60	86	191
306	1.437	85.5	0.54[e]	1.3	15.5	7.31	149	231
220	1.361	81.0	0.45	0.0	12.0	6.81	137	---
317	1.361	81.0	0.38	1.1	17.5	7.19	229	364
315	1.324	78.8	0.38	0.68	15.5	6.80	240	364
312	1.286	76.5	0.38	0.62	19.5	6.37	315	437
224	1.248	74.3	0.28	0.55	23.0[g]	---[f]	---[f]	---[f]
307	1.248	74.3	0.29	0.49	21.0	6.69	407	567
225	1.172	69.8	0.26	0.39	27.5[g]	---[f]	~610	787
221	1.13[h]	67.3	0.26	0.51	26.5[g]	---[f]	---[f]	---[f]
94/6 RDX/Wax (ρ_V = 1.72 g/cc)								
214	1.210[h]	70.3	0.36	0.82	13.5	6.59	182	321
97/3 RDX/Wax (ρ_V = 1.76 g/cc)								
218	1.248[h]	70.9	0.44	3.3	9.5	6.68	79	172

a) B and 2C from eqn. (2). B ≡ r at ~41 mm and t = 0 unless stated otherwise. 2C ≡ acceleration of convective front.
b) Time to detonation relative to discharge of 41 mm ionization probe.
c) Total time to detonation calculated using parameters B and C to extrapolate time to x = 0.
d) No transition to detonation observed.
e) B ≡ r at 28.7 mm. r = 0.59 at 41 mm.
f) Normal analysis of data not possible--see text.
g) Estimated from tube fragments.
h) Handpacked charges.

the 91/9 RDX/Wax mixture, we shall not discuss the data from the runs strictly according to decreasing density as they are listed in Table 1. Instead we shall discuss first those runs in which more insight concerning the DDT mechanism can be gained from the experimental data.

Density: 1.44 g/cc (85.5% TMD) The experimental x-t data obtained from the IPs for Shot 306 (ρ=1.44 g/cc) are shown in Figure 5. The IP discharge times define an initial reaction front accelerating mildly as it leaves the ignitor region. A much more rapid front (a detonation wave) is then observed propagating through the latter half of the charge at a velocity of 7.3 mm/μsec. Least squares analyses of the first six IP data points and the first seven IP data points (according to eqn. (2)) indicate that a slightly better statistical fit is found with the six data point set. The difference is small (i.e., based upon the six point set, the seventh point (130.0, 156.6) is 2.2 μsec "early") but is experimentally significant as discussed below. The velocity of the initial front is 0.56 mm/μsec at t=0 and 0.73 mm/μsec at 150 μsec based upon the least squares fit. Also shown in Figure 5 are three SG excursion times selected from the voltage-time curves for strain gages located at 20.2, 54.1 and 79.8 mm. Figure 6 contains the E-t data for these SG locations*. The E-t curves exhibit some of the features observed for ammonium picrate; namely, the appearance of pressure just ahead of the convective flame front and a mild monotonous pressure increase for a short time interval after the passage of the convective front. In addition, the present voltage-time curves exhibit a feature discussed below and observed in all cases where detonation occurred.

The voltage-time data for the 79.8 mm SG, which represents a typical behavior for a SG located beyond the ignitor region, shows no voltage (pressure) increase until approximately 83 μsec, just before the reaction front arrives at the 79.8 mm location. There is a gentle rise in pressure following this time, very similar to the ammonium picrate data. Consequently, we consider the first reaction front, as outlined by the IPs in Figure 5, to be a convective flame front based upon its low subsonic velocity and the mild initial pressure rise after its passage. However, we see that the voltages after the convective front passes do not approach a constant or maximum value, but instead show a somewhat exponential increase in voltage with increasing time. For the 79.8 mm SG, this postconvective excursion time, t_{PC},

- - - - - - - - - - - - - - - - - -

*The SG E-t curves for this shot and other shots to be discussed later do not cover the complete recording time. We have, instead, selected time intervals which show the important features related to the DDT mechanism. We have kept these data in the form of E-t rather than converting to P-t by using the calibration data of Appendix A because that calibration is a static one, and probably inapplicable to many dynamic ituations. Even when a dynamic calibration is made, the loading rate cannot be expected to cover all those encountered in the DDT studies. For example, the pre-excursion loading rate of Figure 6, 91/9 RDX/Wax, at 85.5% TMD, is about 6 x 10^3 kbar/sec and about the same as that of Figure 4 (ammonium picrate at 90.1% TMD). It is possible that the static calibration is applicable in both these cases, and yet inapplicable to the higher pressure and loading rates of the excursions in Figure 6.

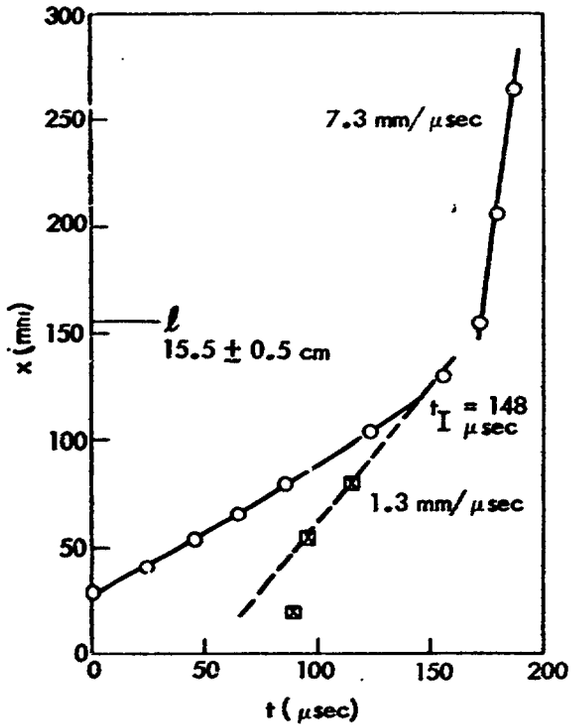

FIG. 5 DISTANCE - TIME DATA FOR 85.5% TMD 91/9 RDX/WAX (SHOT 306); DENSITY = 1.44 g/cc. (○ IP DISCHARGE TIME ⊠ SG EXCURSION TIME, t_{PC}.)

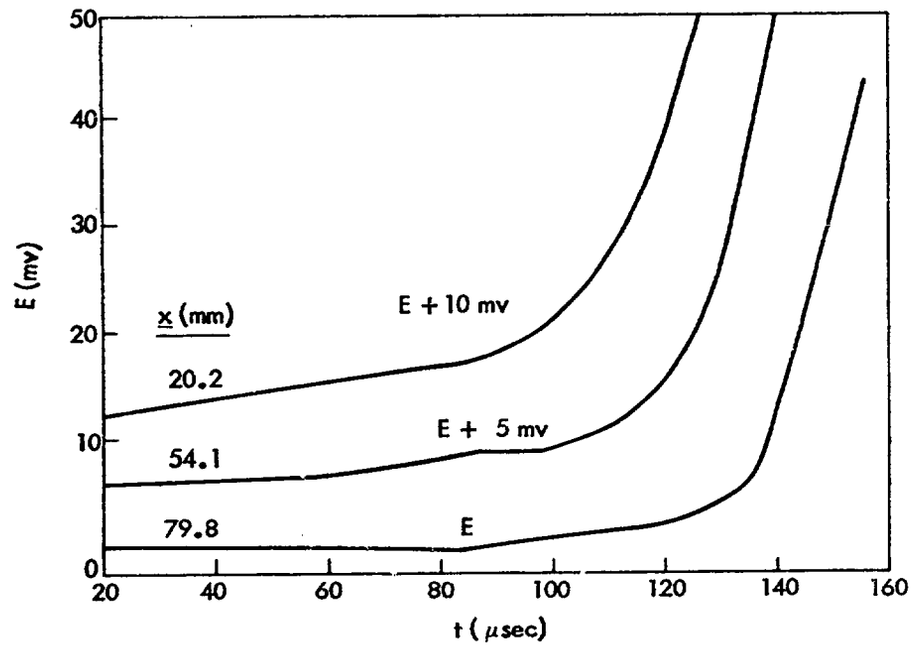

FIG. 6 STRAIN GAGE VOLTAGE - TIME CURVES FOR 85.5% TMD 91/9 RDX/WAX (SHOT 306); DENSITY = 1.44 g/cc.

is 116 ± 2 μsec (relative to the discharge of the first IP). Similar excursion times for the 20.2 and 54.1 mm SG locations are 88 ± 1 and and 96 ± 1 μsec, respectively. [Note that these excursions begin at voltages which are less than the voltage associated with the onset of the plastic yielding of the tube wall (see Appendix A) and that the pressure at which an excursion begins decreases for SGs located farther from the ignitor interface.] In every case where an excursion occurred, we have plotted only the time of that pressure increase, and not the much milder one occurring just before and after the convective front. (For ammonium picrate, only the latter occurred and was the one plotted in Figure 3.)

The combined IP and SG data shown in Figure 5 provide an insight into the behavior occurring in the predetonation region of the tube. After action of the ignitor, a convective flame front starts to propagate through the charge. Sometime after the passage of the convective front a more rapid increase in pressure is detected in a region where the explosive has been burning. It appears from the SG records that the block symbols in Figure 5 may represent the path (as shown by the dashed line) of a compressive wave or perhaps the passage of the first of a series of compressive waves. Its source must certainly lie in the confined burning of the explosive in the ignition region after the convective front passage. What exactly has caused it is not yet clear. For example, it is possible that an event such as a thermal explosion of some of the burning material could have occurred. In this case, the explosion should produce a compressive wave travelling at local sonic velocity. On the other hand, once the porous bed has been pressurized to a certain extent by the combustion gases, the pressure effect on the subsequent burning could lead to an acceleration of the build-up process, leading to an exponential pressure rise as was observed in the case for DDT in cast explosives (1-3). For either case, we can treat the SG excursion times as representing a compressive wave travelling, in this case, at a velocity of 1.3 mm/μsec. This velocity is faster than that of the convective front but slower than the sound velocity of the initial cold and unpressurized explosive (see Section IVC4 for a discussion of sound velocity data). We have called this compressive wave the postconvective (PC) wave.

The seventh IP discharge time which was 2.2 μsec "early" for the convective flame front lies in the path of the postconvective wave. This suggests that the PC wave has overtaken the convective flame front before the onset of detonation as shown in Figure 5. The time of intersection (t_I) of the convective front and the PC wave as shown in Figure 5 is about 148 μsec. This time coincides with the appearance of a large disturbance of several tenths of a volt which is induced on all three SG voltage-time records (Figure 7 shows this disturbance on the 20.2 mm SG record). The disturbance is apparently electromagnetic in nature since it is recorded at the same time (time uncertainty of ± 1 μsec) on all three SG records. The mechanism causing the disturbance is unknown but appears to be connected with the interaction of the PC wave and the convective flame front.

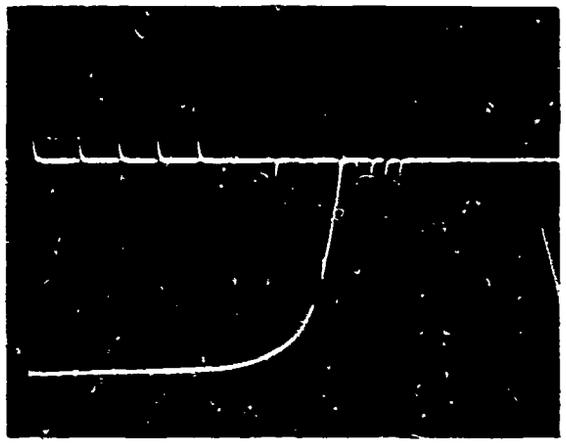

FIG. 7 OSCILLOSCOPE RECORD FOR 85.5% TMD 91/9 RDX/WAX (SHOT 306).

UPPER TRACE - IONIZATION PROBE DISCHARGES.

LOWER TRACE - VOLTAGE - TIME CURVE FOR 20.2 mm SG LOCATION. (NOTE LARGE ELECTROMAGNETIC SIGNAL ON LOWER TRACE BETWEEN SIXTH AND SEVENTH IP DISCHARGES.) MAXIMUM OBSERVED VOLTAGE OUTPUT IS ABOUT 450 mv.

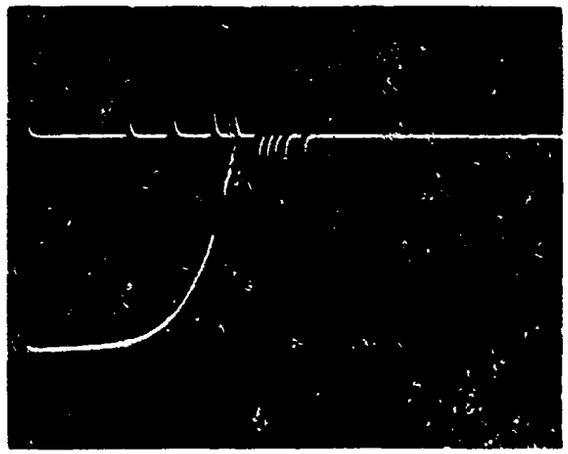

FIG. 8 OSCILLOSCOPE RECORD FOR 90.1% TMD 91/9 RDX/WAX (SHOT 305).

UPPER TRACE - IONIZATION PROBE DISCHARGES.

LOWER TRACE - VOLTAGE - TIME CURVE FOR 20.3 mm SG LOCATION. NOTE LARGE ELECTROMAGNETIC SIGNAL ON LOWER TRACE.

Finally it should be noted that the straight line for the PC wave depends only on two SG excursion times and the IP datum at 155 mm. The excursion time for the 20.2 mm SG location has been ignored. Its behavior is atypical of observations made at densities slightly higher and slightly lower than this run (see results below for Shots 305 and 317).

The point of onset of detonation is defined whenever possible by the extrapolation of the PC wave path into the path of the detonation wave. In this way we have obtained a value of 15.5 ± 0.5 cm. Analysis of the tube fragments confirmed this value; they showed the beginning of a tensile cracking pattern indicative of the detonation at 16.2 cm ± 0.5 cm. The length of the predetonation column, which we have defined by the symbol ℓ, for this experiment (charge density of 1.44 g/cc) is 15.5 cm.

Density: 1.51 g/cc (90.1% TMD) Two experiments were run at a density of 1.51 g/cc, Shots 215 and 305 in Table 1. Figures 9 and 10 show the position-time data for Shot 215 and Shot 305, respectively. Shot 215 yielded limited SG data because one SG was located in the detonation region. In both cases, the predetonation region indicates a mildly accelerating reaction front which we again will classify as a convective front. In Figure 9 (Shot 215), the fifth IP data point (117.6, 87.7), point A, does not belong to either the convective front or the detonation front. Consequently, it appears that point A is associated with the PC wave after it has intersected the convective flame front as discussed earlier for Shot 306. The time of intersection of the two fronts is 81 μsec as defined by the superimposed signal on the two SG records (SGs located at 20.3 and 206.5 mm). The SG signal at 20.3 mm was not recorded after this "EM" disturbance in spite of the fact that only two thirds of its voltage range (0 - 0.6 v) had been covered before the SG ceased recording*. The predetonation column length, ℓ, was estimated to be 12.5 ± 0.5 cm from the tube fragment markings and the IP data. The velocity of the PC wave is estimated to be 1.7 - 1.9 mm/μsec from the IP data, point A, the time of the SG disturbance (81 μsec), and the extrapolated convective path.

The IP data for Shot 305 (Figure 10) show several interesting features. Firstly, there is again an IP data point, point A in Figure 10, which is associated with neither the convective front nor the detonation front. Secondly, eleven IP discharges were recorded as shown in Figure 8. The fourth IP signal is equal in polarity and amplitude to the second IP signal. Apparently, the IP located at

- - - - - - - - - - - - - - - - - - -

*Such an event has occurred several times in the course of this work. Since the SG signal is off scale, the SG has "opened" or a lead to the gage has come loose. Although the latter can't be eliminated as an explanation, the coincidence with the "EM" disturbance time suggests that the "EM" disturbance puts an additional current burden on the SG circuit which can produce SG malfunction if the strain level is high.

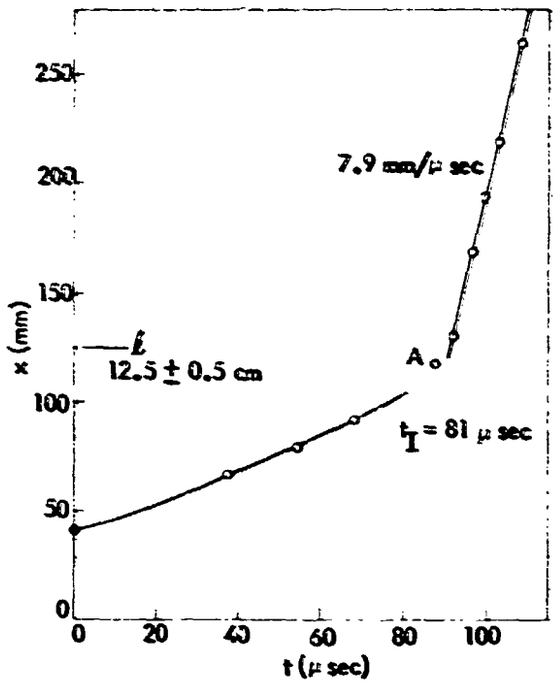

FIG. 9 DISTANCE-TIME DATA FOR 90.1% TMD 91/9 RDX WAX (SHOT 215); DENSITY = 1.51 g/cc. (O IP DISCHARGE TIME.)

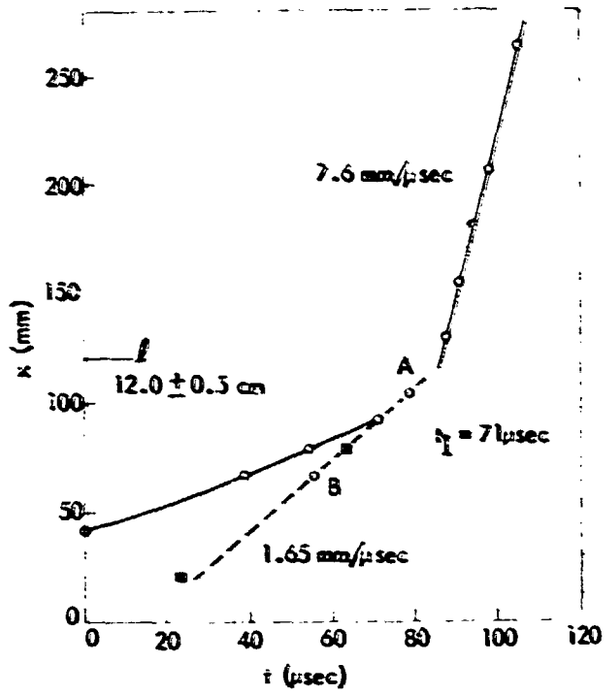

FIG. 10 DISTANCE-TIME DATA FOR 90.1% TMD 91/9 RDX/WAX (SHOT 305); DENSITY = 1.51 g/cc. (O IP DISCHARGE TIME; ⊠ SG EXCURSION TIME, t_{PC}.)

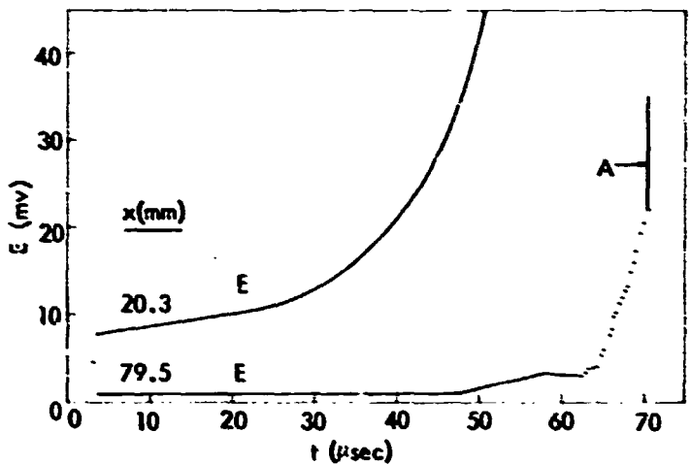

FIG. 11 STRAIN GAGE VOLTAGE-TIME CURVES FOR 90.1% TMD 91/9 RDX/WAX (SHOT 305); DENSITY = 1.51 g/cc. (A-ELECTROMAGNETIC DISTURBANCE)

66.6 mm discharged twice--once with the passage of the convective flame front and again with the passage of the PC wave (point B)*.

The SG voltage-time curves for Shot 305 are shown in Figure 11. Unfortunately, the early portion of the SG data from the 54.1 mm location was lost due to faulty triggering of its oscilloscope. However, E-t data were obtained for the 20.3 and 79.5 mm locations. The type of curve observed is very similar to those discussed earlier for the 85.5% TMD run (Shot 306). Exponential-like increases in voltage are first observed at 23 ± 1 and 63 ± 1 μsec for the 20.3 and 79.5 mm SG locations, respectively.

Thus, as shown in Figure 10, the ionization probe data (points A and B) together with the 79.5 mm SG excursion time define a straight line which represents the passage of the postconvective wave. The 20.3 mm SG excursion time does not fall on this line but does lie close to it. This is quite satisfactory since we do not have any real justification for assuming that the PC wave velocity must be constant over the entire length of the predetonation column length. Temperature variations within the porous burning bed of explosive and reinforcement of the PC wave from the ignitor end are just two factors which would influence the velocity of the postconvective wave as it propagates toward the far end of the tube.

The "EM" disturbance which appears to arise from the interaction of the convective flame front and PC wave is also seen in Figure 8. The time of this disturbance is 71 μsec and agrees very well with the PC wave front and the convective front intersection as outlined in Figure 10. The velocity of the PC wave in Figure 10 is 1.7 mm/μsec. ℓ is estimated to be 12.0 ± 0.5 cm based upon the two criteria mentioned earlier for Shot 306.

In the above discussions we have seen that IPs can define the path of the PC wave after it has intersected the convective front. However, IPs will not usually discharge on the passage of a pure shock front. In the work on DDT in cast explosives, IPs discharged some 10-20 μsec after the passage of a compressive front due to reaction initiated by the compressive front. Here we see that the PC wave propagates apparently at the same velocity in transiting from a burning porous bed into unburned explosive. It appears that the discharge of IPs at the time of passage of the PC wave in unburned explosive may be due to one or more of the following effects. IPs should discharge on the passage of a compressive front if a sufficient quantity of hot gases is present in the pores. Since convective burning was present just before the discharge of the fifth IP in Figures 9 and 10, this condition for discharge would be met. On the other hand, at points A (in Figures 9 and 10) we may have the situation where the convective flame front is being driven by the PC wave and is attached to the PC wave.

- - - - - - - - - - - - - - - - - - -

*It is unusual for an IP to discharge again showing its full amplitude since there is a large recharge time associated with our IP circuits (time constant ~ 1 sec). Thus, it must have been the peculiar nature of convective burning which allowed a second discharge. That is, the flame must have been weak and extinguished in the "pore" associated with the 66.6 mm IP location.

There is an analogy between the interaction of the PC wave and the convective front as observed here for porous solids and the transition to detonation phenomenon in gases. Lewis and von Elbe (18) discuss experiments of Dixon where the interaction of compressive waves running counter to or advancing from behind a gas flame front were photographically recorded. They show an excellent kinematographic record of a build-up to detonation in a CS_2-O_2 mixture. Compressive waves advancing from behind the gaseous flame front were obtained by placing the ignitor some distance from the closed end of the tube. Thus, burning could propagate in two directions from the point of ignition. On reaching the nearer end, the reflected pressure pulses combined to form a compressive wave which travelled through the burned gases and overtook the other flame front. At the intersection of the compressive wave and the other flame front, it was observed that the flame front accelerated (although its velocity was below that of the compressive front). A reflected compressive wave was formed at the point of intersection and travelled back into the burned gases. The interaction of the flame and compressive fronts did not produce immediate detonation although detonation did eventually occur at a time greater than the recording time period.

Density: 1.59 g/cc (94.5% TMD) Two experiments were run with 91/9 RDX/Wax at a density of 1.59 g/cc (94.5% TMD). A transition to detonation did not occur for the first run (Shot 222) as was evident from the tube fragments (see Figure 12a) and the IP data. A transition to detonation did occur in a subsequent experiment (Shot 304). We will discuss the successful experiment first and show later how Shot 222 differs from it. Figure 12b shows the fragments from the tube which underwent DDT. A comparison of Figures 12a and 12b shows that in the absence of diagnostic probe data it is sometimes quite easy to distinguish between an experiment which produced DDT and one which did not. Figure 12b is fairly typical of the type of tube fragments found after a DDT of well compacted charges. The main features of the recovered tube fragments that vary with charge density are length of intact tube and the size of fragments from the detonation region. The length of the recovered tube varies with the length of predetonation column length, ℓ, while the fragments from the detonation region increase in size with decreasing density.

The IP position-time data for Shot 304 are shown in Figure 13. In contrast to all the other experiments for 91/9 RDX/Wax except one (that at 92.3% TMD), Figure 13 shows that the initial reaction front (a convective flame front) is not accelerating as it propagates downstream. The velocity of the convective front does not vary much (+ .06 mm/μsec) when we consider either a 4 point, 5 point, or 6 point IP data set. The main uncertainty lies in defining the path of the convective front as used in the interpretation of the time, t_I. A detonation wave is observed in the latter half of the tube with a velocity of 8.40 mm/μsec. The SG voltage-time data are shown in Figure 14 of SG locations of 20.3, 79.5, and 104.9 mm. The 20.3 mm SG location data show that an exponential-type excursion may have occurred at about 10 μsec. However, the voltage level is near the

a

b

FIG. 12 TUBE FRAGMENTS RECOVERED FROM 94.5% TMD 91/9 RDX/WAX EXPERIMENTS. (a - SHOT 222; b - SHOT 304)

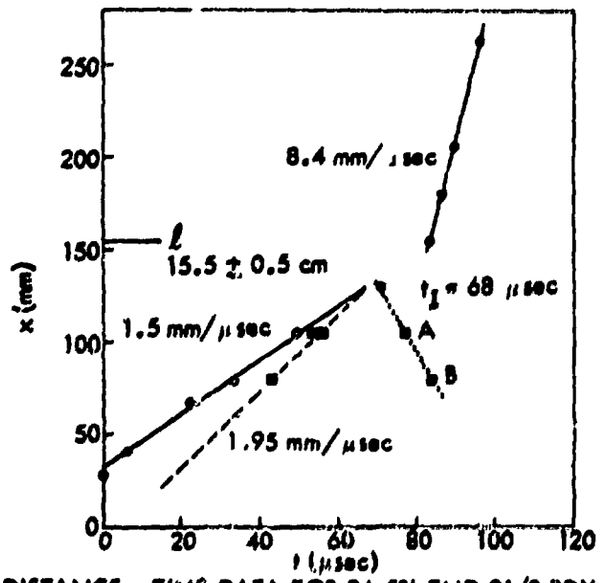

FIG. 13 DISTANCE - TIME DATA FOR 94.5% TMD 91/9 RDX/WAX (SHOT 304); DENSITY = 1.59 g/cc. (○ IP DISCHARGE TIME, ⊠ SG EXCURSION TIME, t_{PC} ■ SG EXTENDED VOLTAGE EXCURSION TIME.)

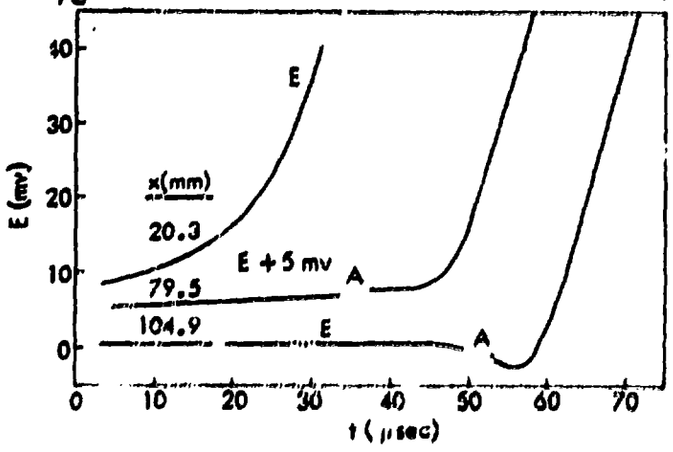

FIG. 14 STRAIN GAGE VOLTAGE - TIME CURVES FOR 94.5% TMD 91/9 RDX/WAX (SHOT 304); DENSITY = 1.59 g/cc. (A - IP DISTURBANCES SEEN ON CURVE.)

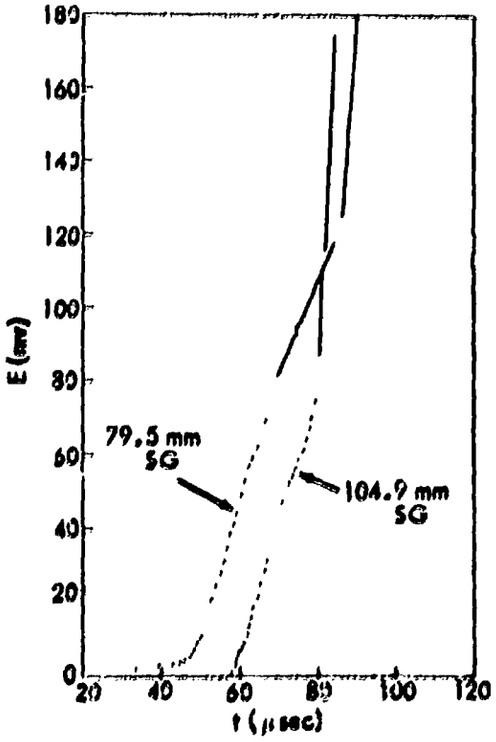

FIG. 15 STRAIN GAGE VOLTAGE - TIME CURVES (EXTENDED) FOR 94.5% TMD 91/9 RDX/WAX (SHOT 304)

linear elastic strain limit and it is difficult to determine whether a SG excursion has occurred or whether the voltage increase is due to plastic yielding of the tube walls. The voltage data for the 79.5 mm SG show the beginning of a mild pressure increase at 31 μsec, just before the passage of the convective front*. From 31 μsec to 42 μsec, there is the gentle pressure (voltage) increase associated with burning after the passage of the convective front. An exponential-type excursion then occurs at 43 μsec.

The voltage-time curve for the 104.9 mm SG is different from that observed in any of the previously discussed experiments. However, its characteristics have been observed in several runs for the SG located farthest from the ignitor and very close to the intersection of the convective flame front and the PC wave. The voltage level from zero time to about 49 μsec is constant. After 53 μsec, the voltage is apparently negative before it begins increasing at 56 μsec. Hence we have selected the excursion time as any time between 53 and 56 μsec and plotted both these times in Figure 13. The reason for the decrease in voltage is not clear but it may be explained qualitetively by assuming the formation of a strong compressive wave at some point between the ignitor and the 104.9 mm SG location.

A strain gage mounted on the outer surface of a cylindrical tube with the SG axis perpendicular to the tube axis will record tangential strain. However, the tangential strain, ϵ_t, is related to the tangential stress, σ_t, (and therefore to the internal pressure as discussed in Appendix A) in the elastic region by the equation

$$E\epsilon_t = (1-\nu^2)\sigma_t - \nu E\epsilon_x \qquad (6)$$

where E = modulus of elasticity
ν = Poisson's ratio
ϵ_x = axial strain

$$\text{or } \epsilon_t = f(p) - \nu\epsilon_x \qquad (7)$$

If an axial strain is present, the tangential strain will not be directly proportional to the internal pressure but will be smaller. This same type of behavior has been observed by Flynn (11,13) who used strain gages to monitor internal pressure during the firing of small bore and large bore guns. The axial strain arises, in those situa-

- - - - - - - - - - - - - - - - - -

*There is a hint that a mild voltage (pressure) increase is seen before 31 μsec (5-18 μsec). If it is real it could indicate some prepressurization of the pores by cooled combustion gases before the arrival of the convective front, something not seen earlier because of the higher permeability of the other charges.

tions, either from the rapid pressurization of the breech area by burning propellant or the motion of the projectile down the gun barrel. A negative excursion occurs in the voltage output (tangential SG circuit) for a short time period before the arrival of the projectile at the SG location. Flynn has attempted to eliminate this situation by using a special arrangement of five SGs so that the recorded voltage is proportional to $\epsilon_t + \nu\epsilon_x$ (or σ_t) (13). However, as of the time of this writing, Flynn has not correlated quantitatively projectile arrival time with the time of onset of the negative or positive excursions of his records.

We have not shown or discussed SG records much above 35 mv because of the uncertainty in the internal pressure-strain relationship for that voltage region. However, the SG records for locations of 79.5 and 104.9 mm in Shot 304 have shown a characteristic which is consistent to some extent with our interpretation of the interaction of the PC wave and the convective flame front. That is, the extended SG data suggest that a wave is travelling toward the ignitor. The extended SG data for the 79.5 and 104.9 mm locations are shown in Figure 15. The two SGs indicate that there are several fairly linear E-t regions after the excursion time. There is a pronounced increase in the E-t slope, however, at 84 and 77 μsec, respectively, for the 79.5 and 104.9 mm SG locations suggesting either a sudden pressure increase at that time or a sudden plastic yielding of the tube walls. The latter would seem to be eliminated by the absence of such a plastic effect in the other runs in this voltage region. In addition, the sudden change in slopes occur at different voltage levels for the two positions. Consequently, we have assumed that at 77 and 84 μsec, there were sudden pressure increases within the tube and these times have been plotted in Figure 13 along with the normal PC excursion times.

When the combined IP and SG data are displayed as shown in Figure 13, we observe the same type of build up process as discussed earlier for lower density experiments. A convective flame front propagates through the charge at a velocity of 1.51 mm/μsec; however, recall that it is not accelerating. Some time after the passage of the convective front, a PC wave is seen propagating at a velocity of 1.95 mm/μsec through the porous burning bed. Based upon the time an electromagnetic disturbance is observed on the voltage-time records for SG locations at 79.5 and 104.9 mm, the PC wave overtakes the convective front at 68 μsec and at 130 mm. However, the IP at this location does not discharge until almost 3 μsec later. It is possible that our selection of the intersection time is in error by one or two μsec. However, at this high density, there should be very small amounts of gas present in the pores to effect a discharge of the 130.05 mm IP (see section IVA1 for a discussion of the convective front and its dependence on compaction). In the absence of sufficient hot gases, there may be an induction time to IP discharge (as found for cast explosives (2)).

An error in the intersection time does not change the mechanistic picture which now suggests that a reflected shock originates as

a result of the interplay of the convective front and the PC wave. The reflected front as defined by points A and B in Figure 13 is consistent with the observations of Dixon as discussed by Lewis and von Elbe (18). The velocity of the reflected wave is 3.6 ± 0.4 mm/μsec, considerably faster than the PC wave. Attempts to find reflected waves in other runs yielded negative results, primarily because of the lack of sufficiently extended voltage records.

As mentioned earlier, another experiment with 91/9 RDX/Wax at 1.59 g/cc did not detonate (Shot 222). The IP distance-time data for Shot 222 are shown in Figure 16. At least three "reaction fronts" can be detected; their "velocities" have been designated in Figure 16.

The SG voltage-time data shown in Figure 17 are helpful in confirming the nature of these fronts. They show that an exponential-type increase occurs at 12 and 22 μsec for SG locations of 54.4 and 79.5 mm, respectively. When the SG data are combined with the IP data, as shown in Figure 16, it appears that the first reaction front (velocity ≤ 1.4 mm/μsec) is a convective flame front; its velocity is quite comparable to that observed in Shot 304 (Figure 13). However, it appears that a PC wave or, at least a compressive wave (shown by the dashed line in Figure 16), was formed much earlier than in Shot 304 and intersected the convective front at about 18 μsec. The velocity of the PC wave or compressive wave is about 2.5 mm/μsec based on the SG data. The discharge of the IPs beyond 80 mm appears to be associated with the passage of this compressive wave in a manner quite similar to that observed for DDT in cast explosives (2,3).

The results of Shots 222 and 304 for a density of 1.59 g/cc do not differ greatly in the early time period except that a compressive wave overtook a convective front much closer to the ignitor region in Shot 222. This seems to suggest that failure to detonate was due to inaccessible parameters, such as position and time of formation of the necessary precursor shock. The tube fragments, Figure 12a, show that a vigorous reaction did occur in the nondetonating run. As charge density approaches crystal density, the magnitude of the critical initiating shock for detonation (as defined in shock initiation studies) increases more rapidly for small increases in charge density than at lower densities (8). Thus, our conclusion is that detonation failed to be achieved in Shot 222 because of inadequate formation of any initiating precursor shock, as indicated by the premature compression wave.

Density: 1.55 g/cc (92.3% TMD) Since one of the 94.5% TMD shots did not undergo DDT, a subsequent experiment (Shot 316) was run at a slightly lower charge density (1.55 g/cc). A transition to detonation did occur as shown by the IP data in Figure 18. However, as found for Shot 304 (Figure 13), the convective front, which precedes the detonation front, is not accelerating in its propagation toward the far end of the tube.

The SG voltage-time curves for Shot 316 are shown in Figure 19 for SG locations of 54.0 and 79.1 mm. The 54.0 mm E-t data show some

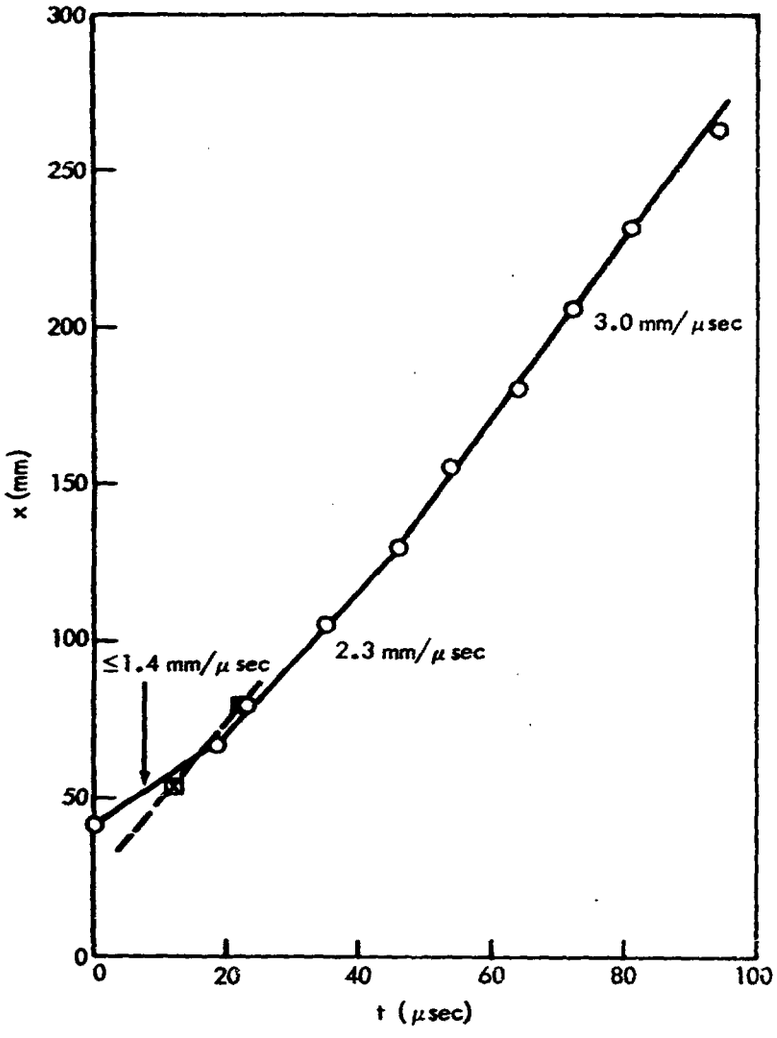

FIG. 16 DISTANCE - TIME DATA FOR 94.5% TMD 91/9 RDX/WAX (SHOT 222); DENSITY = 1.59 g/cc. (O IP DISCHARGE TIME, ⊠ SG EXCURSION TIME, t_{PC}.)

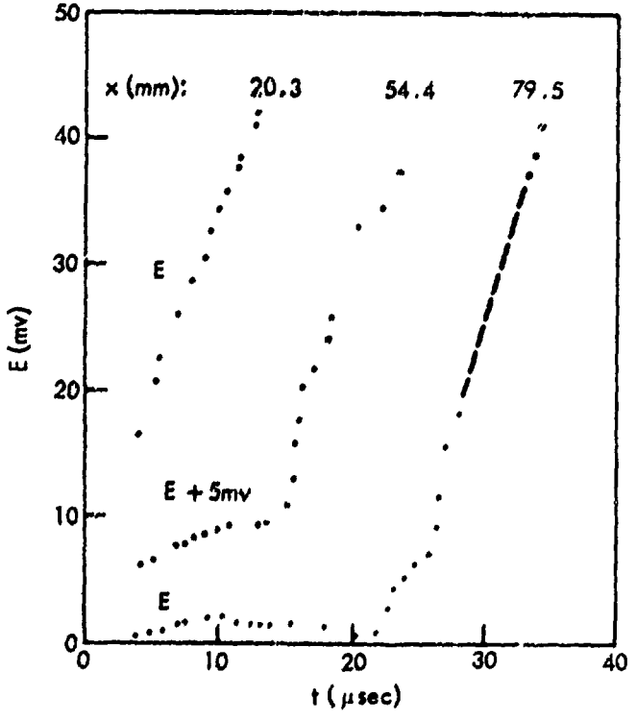

FIG. 17 STRAIN GAGE VOLTAGE - TIME CURVES FOR 94.5% TMD 91/9 RDX/WAX (SHOT 222).

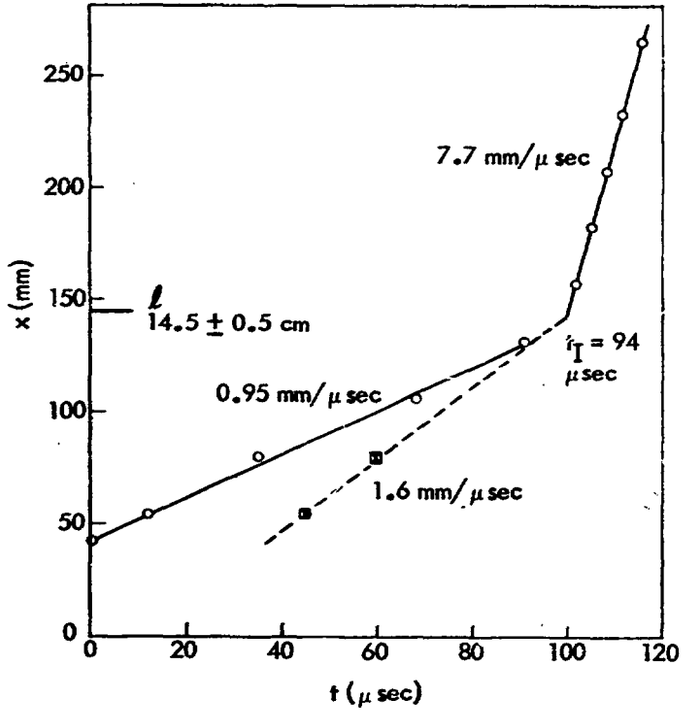

FIG. 18 DISTANCE-TIME DATA FOR 92.3% TMD 91/9 RDX/WAX (SHOT 316); DENSITY = 1.55 g/cc, (O IP DISCHARGE TIME ⊠ SG EXCURSION TIME, t_{PC}.)

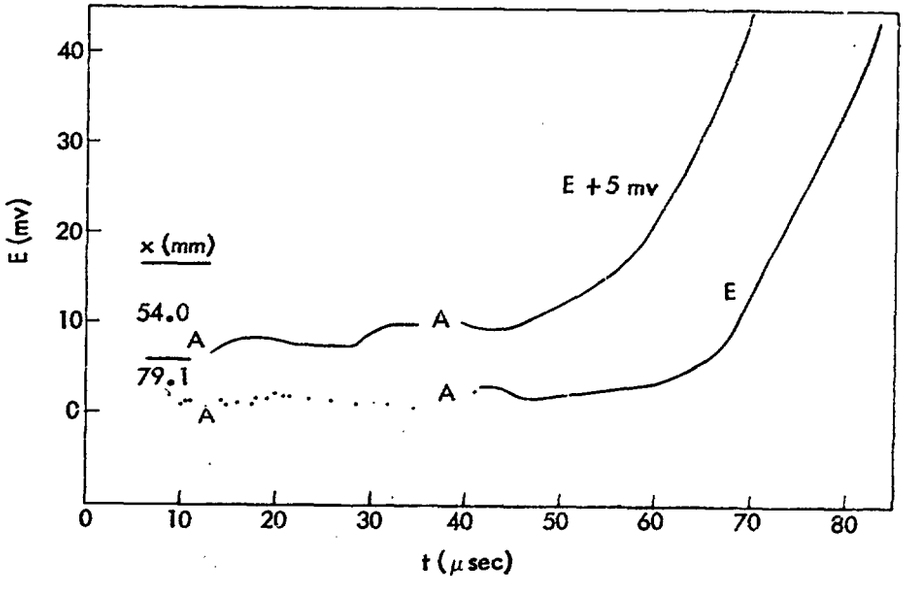

FIG. 19 STRAIN GAGE VOLTAGE - TIME CURVES FOR 92.3% TMD 91/9 RDX/WAX (SHOT 316) (A - IP DISTURBANCES SEEN ON CURVE).

rather distinct increases in voltage in the convective and postconvective burning time interval for this location. For example, the first voltage increase starts at about 12 μsec in good agreement with the arrival of the convective front (vel. = 0.95 mm/μsec) at the 54.0 mm location. Beyond 12 μsec, the voltage increases to a maximum (voltage increase is about 2.5 mv or 0.5 kbar) before it decreases slightly to a plateau region. At 28 μsec, there is another increase in SG voltage, again about a maximum of 2.5 mv, followed by a slight decrease to a plateau region. Following the second plateau, the PC wave excursion begins at about 45 μsec (for the 54.0 mm location).

The SG voltage data for the 79.1 mm location shows a small increase starting at about 17 μsec which reaches a maximum increase of about 1 mv before returning to its original "baseline". The next voltage increase begins at about 35 μsec (corresponding to the arrival of the convective front at the 79.1 mm location). The voltage increase associated with this excursion is about 2.5 mv (i.e., about the same magnitude as observed at 54.0 mm). As in the case of the 54.0 mm SG data the voltage reaches a maximum before leveling out after the passage of the convective front.

The 54.0 and 79.1 mm SG data are consistent to a degree with the developing picture of pressure (voltage) increases with the arrival of the convective front at a SG location. The small excursion (at 17 μsec for the 79.1 mm SG location) which is anomalous has been observed on several other shots at the SG location farthest from the ignitor. Such excursions are believed caused by some pressure disturbance originating in the near end of the tube and propagating through the steel confinement (i.e., it is analogous to SG records of Flynn (11).

When we consider the IP data and the PC wave excursion times as determined from Figure 19, we again observe that the PC wave (velocity ~ 1.6 mm/μsec) intersects the convective front at about 94 μsec as seen in Figure 18. The time of intersection of the two fronts again is in good agreement with the recording of an electromagnetic disturbance on the SG records at this time (i.e., 94 μsec).

Density: 1.36 g/cc (81.0% TMD) Two experiments were with 91/9 RDX/Wax at a density of 1.36 g/cc (81.0% TMD). The first run, Shot 220, did not yield any SG data. The ionization probe data, shown in Figure 20, reveal a convective flame front which appears to be travelling at a constant velocity of 0.45 mm/μsec. A detonation wave was observed about 12 cm beyond the ignitor interface and had a velocity of 6.8 mm/μsec.

The second experiment at this density, Shot 317, yielded a more complete picture of the buildup to detonation and also showed different behavior in the predetonation region of the charge. Figure 21 shows the IP data along with the PC excursion times derived from the SG data (Figure 22). The initial reaction front, a convective flame front, has a velocity of 0.38 mm/μsec at zero time. In contrast to Shot 220, Figure 20, the convective front is definitely

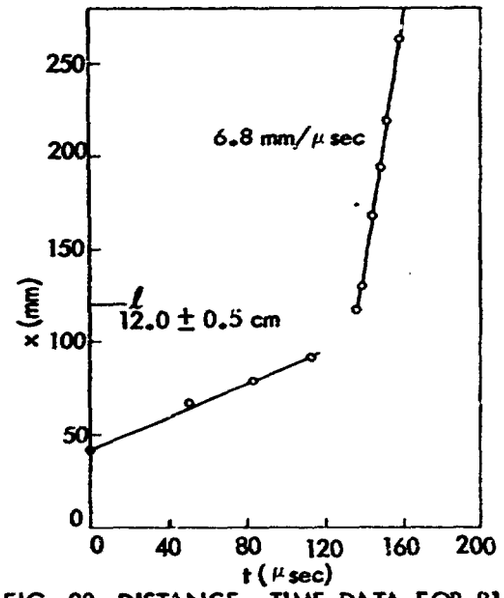

FIG. 20 DISTANCE - TIME DATA FOR 81.0% TMD 91/9 RDX/WAX (SHOT 220); DENSITY = 1.36 g/cc. (○ IP DISCHARGE TIME) TIME.)

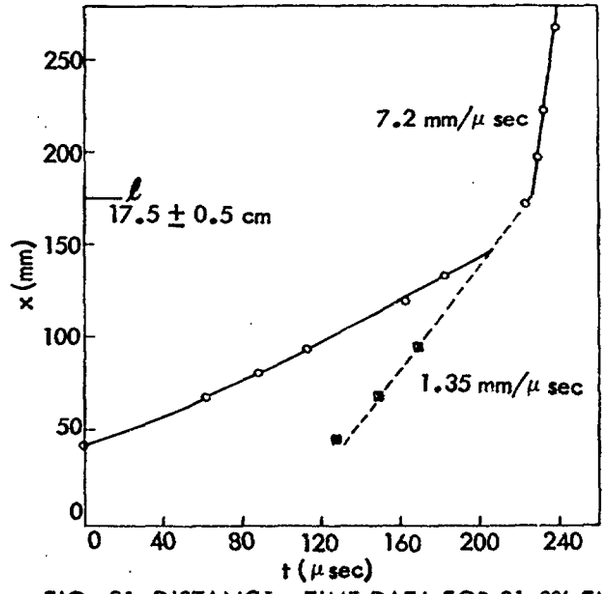

FIG. 21 DISTANCE - TIME DATA FOR 81.0% TMD 91/9 RDX/WAX (SHOT 317): DENSITY = 1.36 g/cc. (○ IP DISCHARGE, ⊠ SG EXCURSION TIME, t_{PC}.)

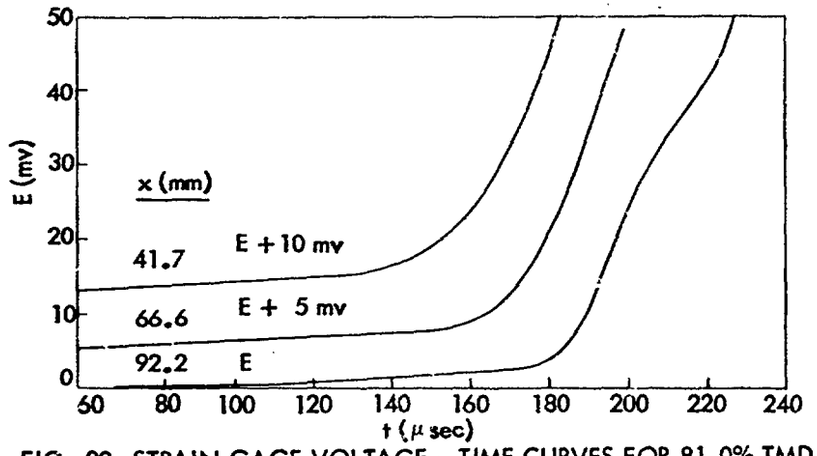

FIG. 22 STRAIN GAGE VOLTAGE - TIME CURVES FOR 81.0% TMD 91/9 RDX/WAX (SHOT 317).

accelerating: its velocity is 0.61 mm/μsec at 210 μsec, a time just before the projected intersection of the convective and PC fronts. However, no electromagnetic disturbance was observed on any SG record for this run.

The strain gage voltage-time curves for Shot 317, shown in Figure 22, reveal the same features discussed earlier for the convective front and the PC excursion. PC excursion times of 128, 149 and 170 μsec have been selected for the 41.7, 66.6 and 92.2 mm SG locations, respectively. One distinct feature noted in Figure 22, however, is the decrease in dE/dt in the time interval of 200 to 220 μsec for the 92.2 mm SG location. Although not shown completely in the figure, at times beyond 220 μsec, dE/dt does increase even more rapidly than it did earlier (i.e., at 190-200 μsec) for the 92.2 mm location. At present we have no explanation for this sigmoid behavior of voltage with increasing time for the 92.2 mm location. There is the possibility that this behavior indicates a large axial strain in the steel tube. The 66.6 mm SG location would show less deviation from a tangential strain value (see equation 5) simply because the pressure at 66.6 mm is 2 to 3 kbar (20 mv) higher than at 92.2 mm at 200 μsec. The 66.6 mm SG record does show a sigmoid characteristic (i.e., having a point of inflection) at higher voltage (at about 60 mv at 210 μsec). Thus, the voltage-time curves from the two strain gages at 66.6 and 92.2 mm are qualitatively similar. The bends in the curves occur at widely different voltages suggesting that the time associated with the bend is the more important characteristic.

The postconvective wave for this shot is defined by the dashed straight line in Figure 21 which passes through the SG excursion time points for the 66.6 and 92.2 mm locations and also through the seventh IP discharge time. (As discussed earlier for Shots 306 and 305, this seventh IP point is not associated with the projected path of the convective front nor with the path of the detonation wave.) The velocity of the PC wave is 1.35 mm/μsec. The excursion time for the 41.7 mm SG location does not lie on the path of the PC wave but does lie close to it (this contrasts with Shot 305 (density of 85.5% TMD), Figure 9).

The point of transition to detonation in Figure 21 is selected as 17.5 cm. This value contrasts sharply with the 12.0 cm found for the same density in the earlier run (Shot 220). The time from discharge of the 41 mm IP to the onset of detonation is about 230 μsec for Shot 317 but only 137 μsec for Shot 220. In addition, the convective front was accelerating in Shot 317 but not in Shot 220. Thus, it is quite evident from these data that the buildup process leading to detonation in these two experiments is quite different. Based upon comparison of ℓ values and the nature of the convective front for experiments at low and high densities, we believe that Shot 317 is more representative of DDT for a density of 81.0% TMD.

Density: 1.32 g/cc (78.8% TMD) To check the widely divergent results for 91/9 RDX/Wax at a charge density of 81.0% TMD (see

above), a run (Shot 315) was made at a slightly lower density, 1.32 g/cc (78.8% TMD). The distance-time data (IPs and SG excursion times) are displayed in Figure 23 and show initially a mildly accelerating convective front propagating downstream. The convective flamefront accelerates from 0.38 mm/μsec (t = 0) to 0.53 mm/μsec (t = 235 μsec). The velocity of the detonation wave, as shown by the IP data, is 6.8 mm/μsec. The SG voltage-time curves for this run are shown in Figure 24. Again the E-t curves display general characteristics associated with the convective front and the post convective front. The excursion times for the PC front selected from Figure 24 are 149, 169 and 197 μsec for SG locations at 53.9, 79.9, and 104.9 mm, respectively. When these excursion times are plotted in the x-t plane, i.e., Figure 23, the three SG locations define again the path of the PC wave. The velocity of the PC wave at this density is the lowest observed, 1.1 mm/μsec. The path of the PC wave was defined by the three excursion times, in addition to the electromagnetic disturbance observed on the SG records at 235 μsec.

The length of the predetonation column is approximately 15.5 cm and the time from discharge of the 41 mm IP to the onset of detonation is about 240 μsec. These data for this 78.8% TMD run (Shot 315) are much more consistent with Shot 317 (81.0% TMD) than with Shot 220 (81.0% TMD)--see above.

Density: 1.29 g/cc (76.5% TMD) Shot 312 (1.29 g/cc) underwent a transition to detonation at about 19.5 cm. The IP data, shown in Figure 25, indicate that the velocity of the convective front increased from 0.38 mm/μsec at 40 mm to 0.56 mm/μsec at 180 mm. The SG excursion times shown in Figure 25 were selected from the voltage-time SG records displayed in Figure 26.

The E-t curves in Figure 26 show the typical behavior of pressure (voltage) increases associated first with the convective front and then the PC front. However, the curves also show, for the first time, that the voltage curves, for different SG locations along the tube, intersect at a voltage (pressure) level less than 40 mv (<4.5 kbar). Specifically in Figure 26, we see that the output of the 79.5 mm SG exceeds the output of the 20.1 mm SG after about 265 μsec. This observation is discussed in more detail in Appendix B.

The postconvective wave in Figure 25, as defined by the two strain gages farthest from the ignitor, intersects the convective flame front just prior to the onset of detonation. The velocity of the PC wave at 1.6 mm/μsec, however, is now faster than the estimated sound velocity of the original cold, unpressurized explosive charge (see section IVA.4 for a discussion of sound velocities at various compactions).

Density: 1.25 g/cc (74.3% TMD) The IP data for the 1.25 g/cc experiment (Shot 307) are shown in Figure 27. A detonation wave is not observed until 405 μsec after the discharge of the IP at 41.2 mm. The convective flame front is observed propagating slowly in the predetonation column of explosive. Initially the convective velocity

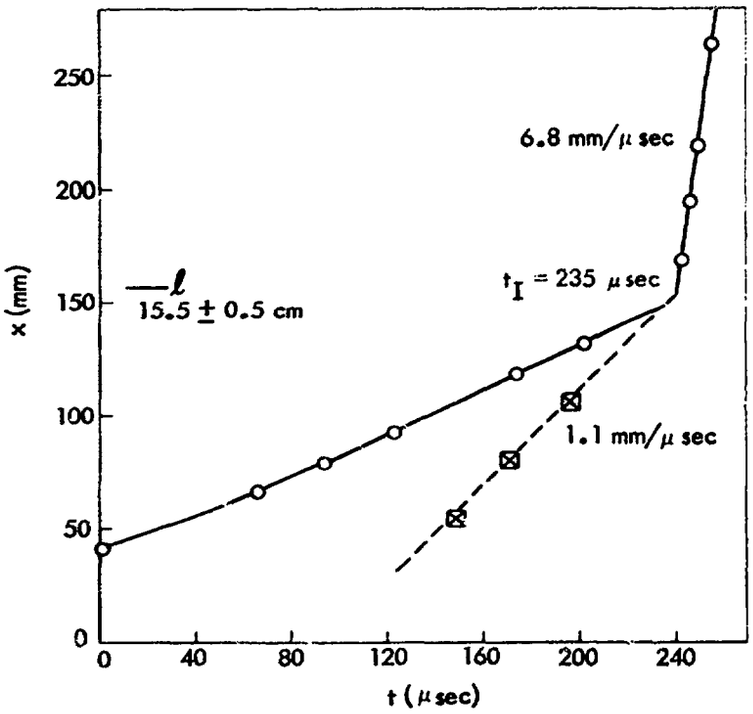

FIG. 23 DISTANCE-TIME DATA FOR 78.8% TMD 91/9 RDX/WAX (SHOT 315); DENSITY = 1.32 g/cc, (O IP DISCHARGE TIME, ⊠ SG EXCURSION TIME, t_{PC}.)

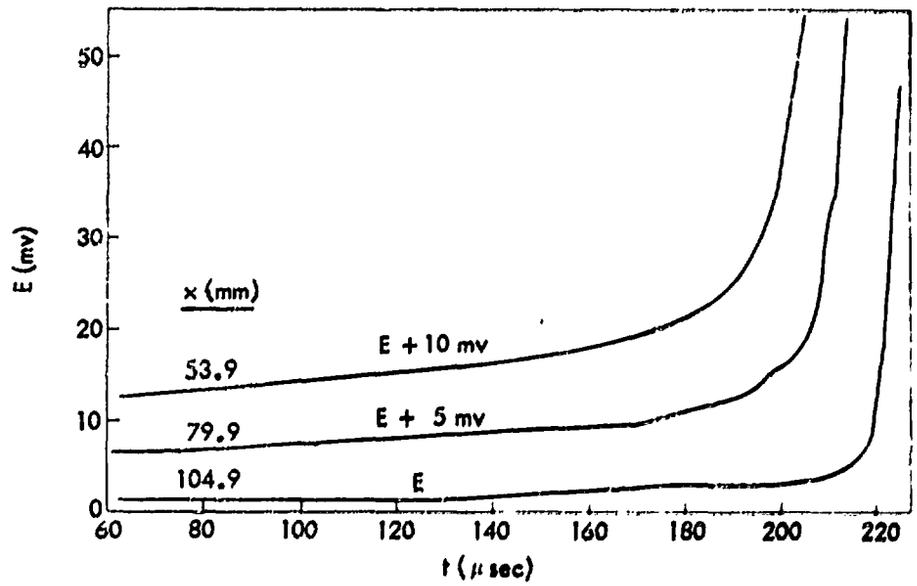

FIG. 24 STRAIN GAGE VOLTAGE - TIME CURVES FOR 78.8% TMD 91/9 RDX/WAX (SHOT 315).

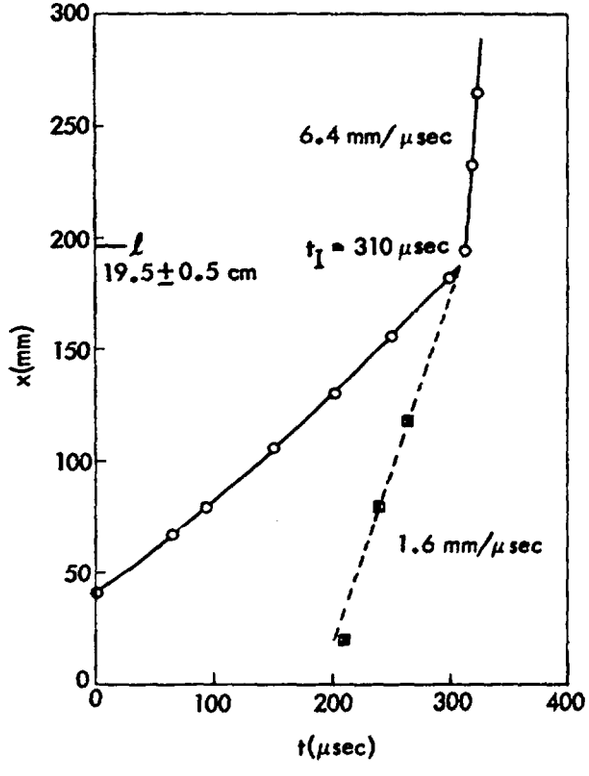

FIG. 25 DISTANCE - TIME DATA FOR 76.5% TMD 91/9 RDX/WAX (SHOT 312); DENSITY = 1.29 g/cc. (○ IP DISCHARGE TIME, ⊠ SG EXCURSION TIME, t_{PC}.)

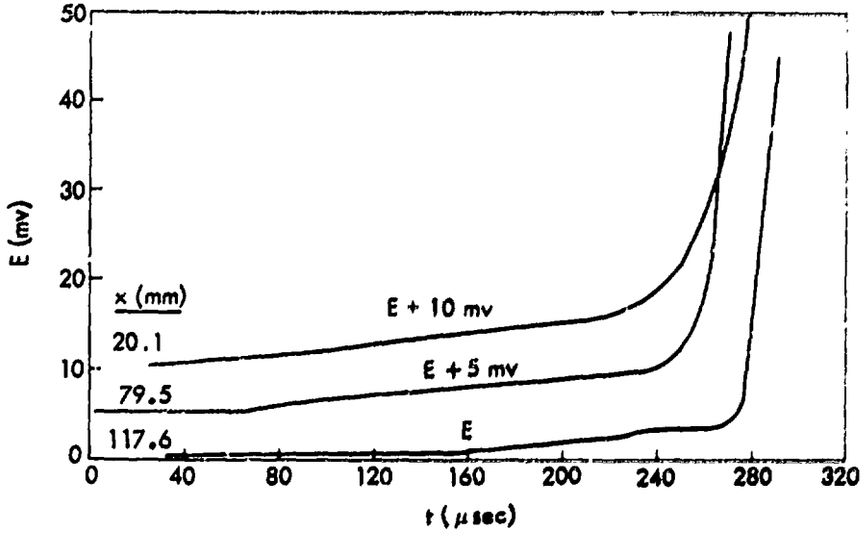

FIG. 26 STRAIN GAGE VOLTAGE - TIME CURVES FOR 76.5% TMD 91/9 RDX/WAX (SHOT 312)

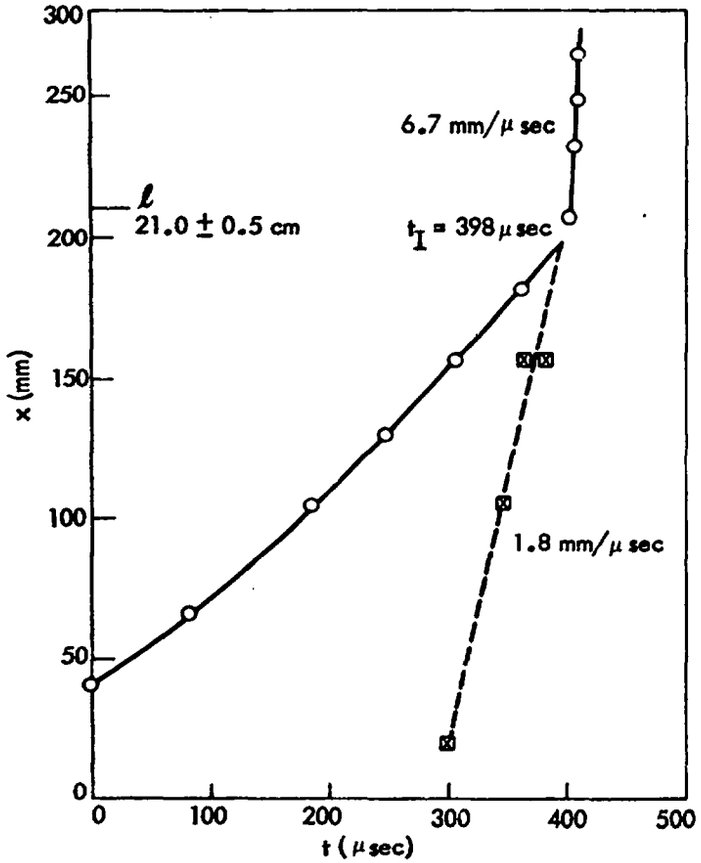

FIG. 27 DISTANCE - TIME DATA FOR 74.3% TMD 91/9 RDX/WAX (SHOT 307); DENSITY = 1.25 g/cc. (○ IP DISCHARGE TIME, ⊠ SG EXCURSION TIME, t_{PC}.)

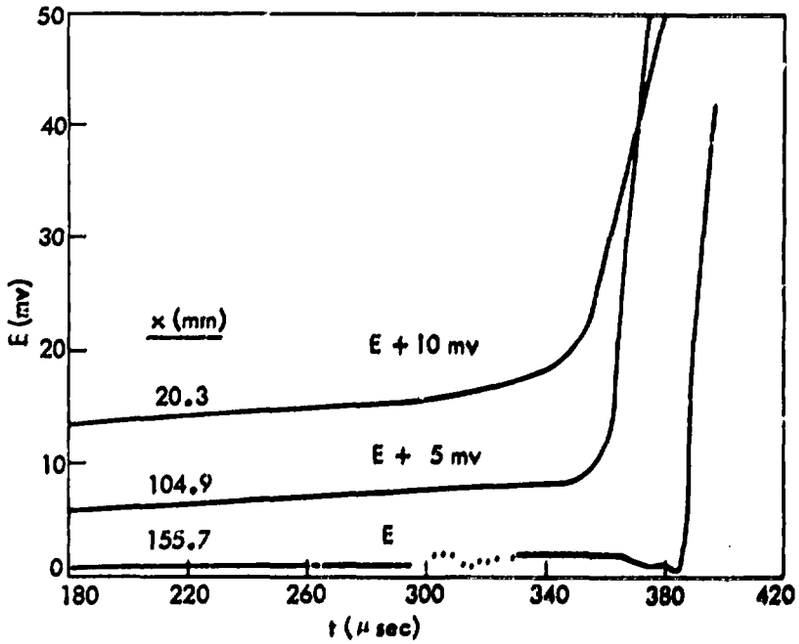

FIG. 28 STRAIN GAGE VOLTAGE - TIME CURVES FOR 74.3% TMD 91/9 RDX/WAX (SHOT 307)

is 0.29 mm/μsec and then increases to 0.49 mm/μsec before the onset of detonation. The SG voltage-time data over a selected time interval is shown in Figure 28. The SG data for locations of 20.3 and 104.9 mm are typical of the general case discussed earlier. The voltage increases just before the arrival of the convective front at the SG locations (these portions of the curve are not shown). The beginning of the exponential-type increase in pressure is observed at 300 and 348 μsec for the 20.3 and 104.9 mm SG, respectively. The SG at 155.7 mm shows some peculiar features such as those discussed earlier for Shot 304. For this SG location, there is an increase in voltage at 300 μsec, just before the passage of the convective front as expected. However, this "pressure" is relieved and the E-t data show small perturbations about a straight line until 366 μsec. After that the voltage decreases until 384 μsec at which time a rapid positive excursion begins. The excursion time for the 155.7 mm SG can be any time between 366 and 384 μsec, as discussed earlier for Shot 304*.

The combined IP and SG data of Figure 27 show the pattern of a PC wave travelling through the burning explosive bed sometime after the passage of the convective flame front. We have used the electromagnetic disturbance time, in this case (398 μsec) to define the path of the PC wave between 120 and 190 mm. Using the electromagnetic disturbance time, along with the two other SG excursion times, we see that the excursion time for the 155.7 mm SG is indeed between the two selected times, 366 and 384 μsec. The velocity of the postconvective wave is 1.8 mm/μsec, considerably faster than the convective flame rate and the sound velocity of the cold, unpressurized explosive bed. This latter observation is different from all the previous PC velocity observations except for Shot 312. That is, only above 78.8% TMD is the velocity of the postconvective wave less than the estimated sound velocity of the original explosive charge.

The SG voltage-time data in Figure 28 also show that the output of the 104.9 mm SG exceeds the output of the 20.3 mm SG after about 367 μsec. This intersection of E-t curves occurred in the 76.5% TMD experiment also.

An earlier run had been made at a density of 1.25 g/cc (Shot 224). However, the IP data were incomplete, extending only to 180 mm from the ignitor/explosive interface, as seen in Figure 29. The tube fragments showed the tensile cracking pattern beginning at 23.5 cm. Hence we have assigned an ℓ value of 23.0 ± 1.0 for this run. This is 2 cm longer than found in Shot 307 for the same density. We have compared the IP data for these two runs and found that they are very similar except for the first IP data point. Displacing the time coordinate 18 (± 2) μsec for Shot 224 showed almost identical convective front paths for tube distances greater than 60 mm. Thus, for

- - - - - - - - - - - - - - - - - -

*Note that this negative decrease in the E-t curve just before the arrival of the PC wave occurs when the distance between the SG and the point of intersection of the convective and PC fronts is small. In this shot, this distance is about 4 cm. For the 1.29 g/cc experiment (see Figure 26) where there was no negative decrease, the distance between the SG farthest from the ignitor and the point of intersection of the fronts is about 7 cm.

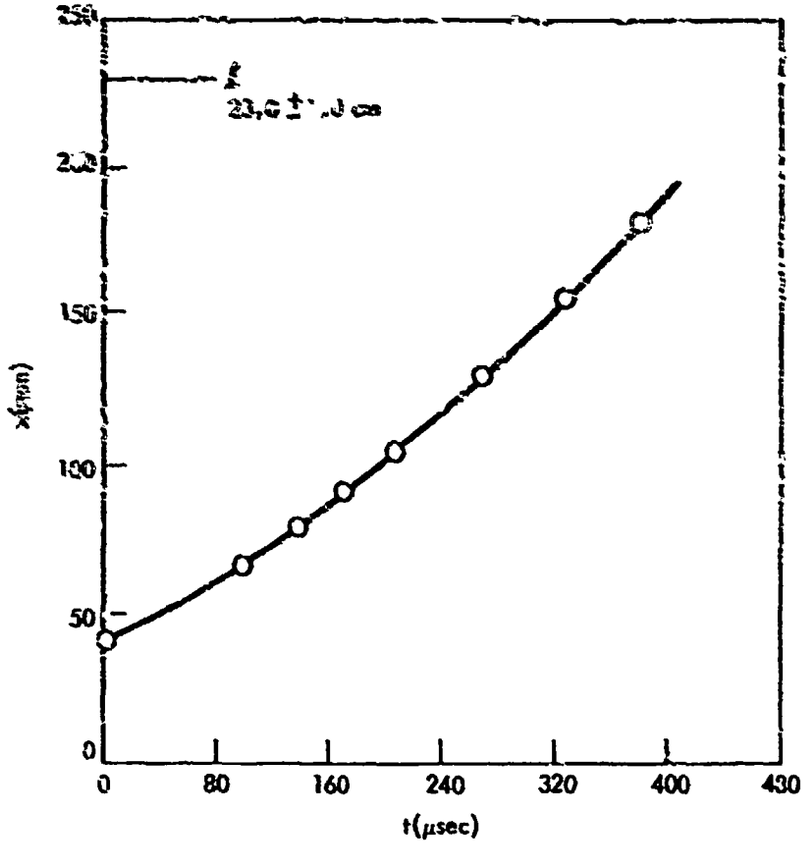

FIG. 29 DISTANCE - TIME DATA FOR 74.3% TMD 91/9 RDX/WAX (SHOT 224); DENSITY = 1.25 g/cc (⊙IP DISCHARGE TIME)

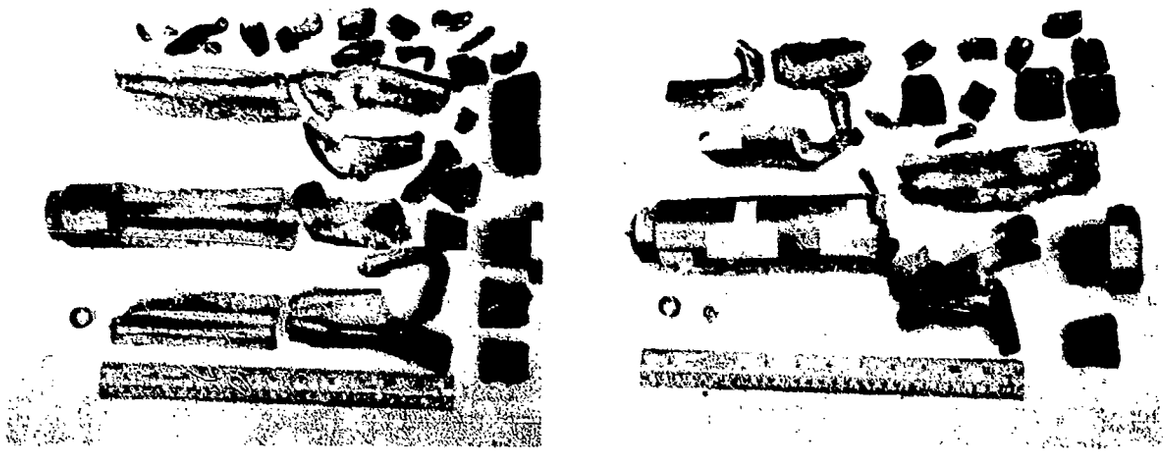

a b

FIG. 30 TUBE FRAGMENTS RECOVERED FROM 74.3% TMD 91/9 RDX/WAX EXPERIMENTS a. SHOT 304; ℓ IS 21cm (SEE FIG. 27), b. SHOT 224; ℓ IS 23cm (SEE FIG. 29)

Shot 224 something delayed the propagation of the convective front in the ignitor region. It is interesting to speculate that this factor may have also been responsible for the increased length of the predetonation column, ℓ, relative to Shot 307. Figure 30a shows that the ignitor end tube fragment from Shot 307, with its smaller value for ℓ, is comparable with its counterpart from Shot 224 (Figure 30b). Note in this figure the different fragmentation for the ignitor end in these two experiments.

Density: 1.17 g/cc (69.8% TMD) This run (Shot 225) has the lowest charge density that was prepared using the hydraulic press. Ten IPs were used but only nine discharged. The IP which didn't discharge even though the time scale was long enough was the last in the tube at 263.4 mm, a very important data point. Figure 31 shows the IP data and the SG excursion times for three SGs located at 20.3, 130.6, and 156.0 mm. The IP data define the path of a convective front propagating toward the far end of the tube. The velocity increased from 0.26 mm/μsec (t = 0) to 0.5 mm/μsec (t ~ 600 μsec). There is no evidence of a detonation front from the IP data. The SG voltage-time curves for a selected time interval are shown in Figure 32. The pressure (voltage) recorded at all SG locations increases very slowly with time until the time of the PC excursions.

An electromagnetic disturbance was observed on the 20.3 mm SG low sensitivity record at 606 μsec. We have assumed that this time represents the intersection of the convective front and the PC wave and have accordingly drawn the PC wave based upon this assumption. In this case the velocity of the PC wave is 1.9 mm/μsec, definitely supersonic with respect to the original cold explosive charge. Based upon the incomplete diagnostic data we have estimated that the onset of detonation was at 27.5 ± 1.0 cm. The tube fragments were not very helpful in locating the point of DDT because of its proximity to the far end of the tube. However, detonation appears to have occurred because the tube fragments from this experiment were very similar to those recovered at slightly higher densities (i.e., shots 224, 307 and 312).

The SG voltage-time curves of Figure 32 show that the voltage outputs for the two SG locations farthest from the ignitor exceed the output for the 20.2 mm SG location at least 50 μsec before the estimated time of onset of detonation. This pattern has been observed for all charge densities less than 78.8% TMD.

Density: 1.13 g/cc (67.3% TMD) This charge was packed by vibration to give the lowest stable charge density (Shot 221). It was the first of the low density charges fired and its diagnostic data are incomplete. Data reduction of the seven IP data covering the range of 40 to 200 mm showed that the convective front was propagating initially at a velocity of 0.26 mm/μsec, the same velocity as for the 69.8% TMD charge (Shot 225). However, it appeared to be accelerating slightly faster, as shown in Table 1. Based upon the tube fragment markings starting between 26 and 26.5 cm, detonation was judged to have started at 26.5 ± 1.0 cm.

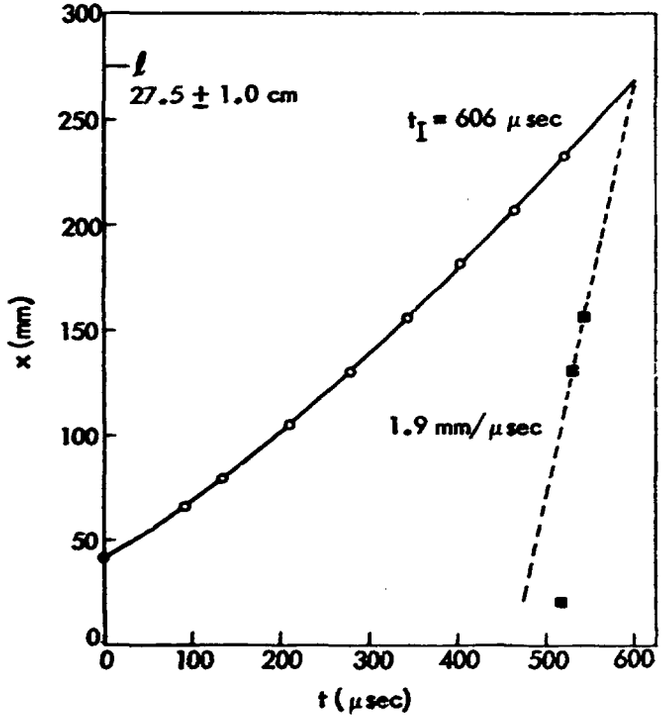

FIG. 31 DISTANCE - TIME DATA FOR 69.8% TMD 91/9 RDX/WAX (SHOT 225); DENSITY = 1.17 g/cc. (○ IP DISCHARGE TIME ⊠ SG EXCURSION TIME, t_{PC}.)

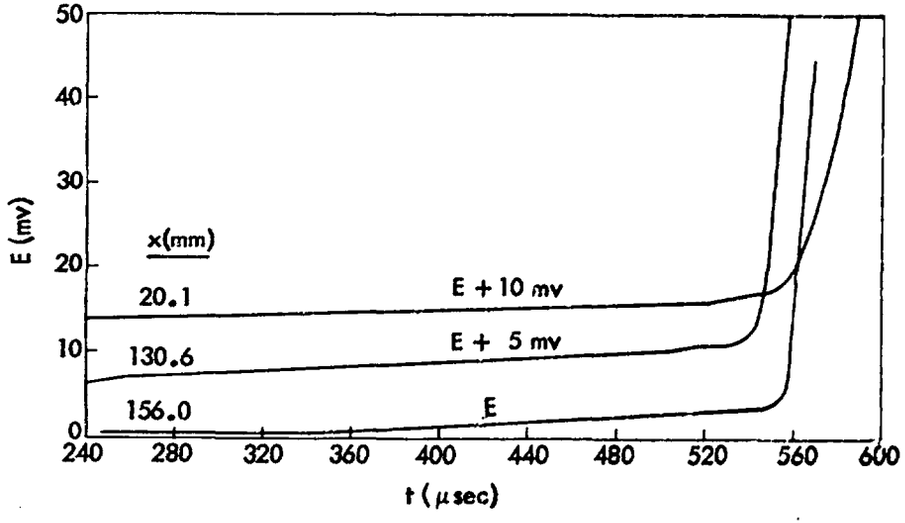

FIG. 32 STRAIN GAGE VOLTAGE - TIME CURVES FOR 69.8% TMD 91/9 RDX/WAX (SHOT 225)

b) 94/6 RDX/Wax

A single run has been made with the 94/6 RDX/Wax mixture. Shot 214 (Table 1) was handpacked to give a charge density of 1.21 g/cc (70.3% TMD). The IP data are shown in Figure 33. There are no high sensitivity complementing SG data for this run. The initial reaction front appears to be a convective front based upon its low velocity. The velocity increases from 0.36 mm/μsec at zero time to 0.47 mm/μsec at 140 μsec. Least squares analysis of the fifth IP datum, point A in Figure 33, indicated that it does not fit the projected path of the convective flame front as defined by the first four IP data. In addition, point B in Figure 33 does not appear to be associated with the steady state detonation front. When the last four points are used to calculate the detonation velocity, D from equation (3), the standard deviation, s_d, of the total fit, decreases to 0.47 from a s_d of 1.95 when the last 5 IP data points are used. Correspondingly, D increases to 6.59 ± 0.08 mm/μsec (4 data point set) from 6.36 ± 0.24 mm/μsec (5 data point set). This statistical treatment is consistent with the tube fragment wall markings. Consequently, the predetonation column length, ℓ, is estimated to be 13.5 ± 0.5 cm.

Points A and B in Figure 33 appear to be associated with a precursor wave, perhaps identical to the PC wave observed in the 91/9 RDX/Wax mixture. If we assume that points A and B define a single wave, then its velocity is 1.0 mm/μsec, very close to the estimated sonic velocity for the initial cold explosive charge.

c) 97/3 RDX/Wax

A single low density run has been made for the 97/3 RDX/Wax mixture also. Figure 34 shows the IP data for Shot 218 (ρ = 1.25 g/cc, 70.9% TMD). Only three IP data points lie in the convective flame front region and have been fitted using equation (2). The initial convective velocity, 0.44 mm/μsec, at 41 mm increases to 0.67 mm/μsec at 80 mm.

The tube fragments indicated the onset of steady state detonation at 9.5 to 10.0 cm, slightly higher than suggested by the fourth IP data point. Consequently, the last seven IP points were analyzed by least squares using equation (3). s_d was found to be 1.11, 0.72, and 0.75 when the data sets consisted of the last seven points, the last six points, and the last five points, respectively. The corresponding values for D were 6.62 ± 0.10, 6.68 ± .08, and 6.70 ± .10 mm/μsec. We have selected, therefore a tentative predetonation column length of 9.5 ± 0.5 cm for this density of 97/3 RDX/Wax.

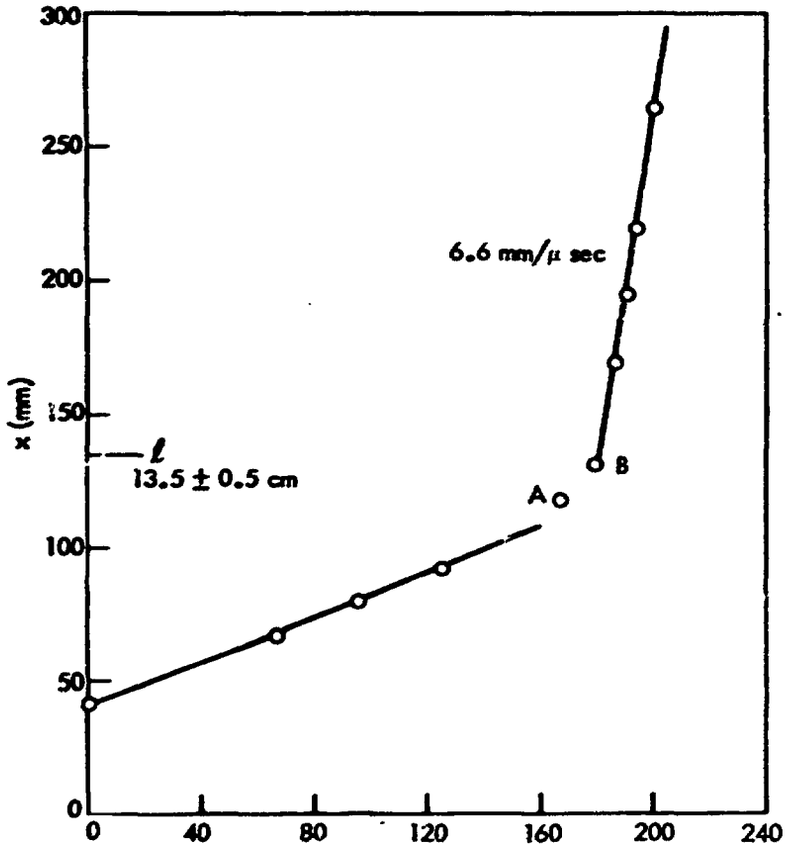

FIG. 33 DISTANCE - TIME DATA FOR 70.3% TMD 94/6 RDX/WAX (SHOT 214); DENSITY = 1.21 g/cc. (○ IP DISCHARGE TIME)

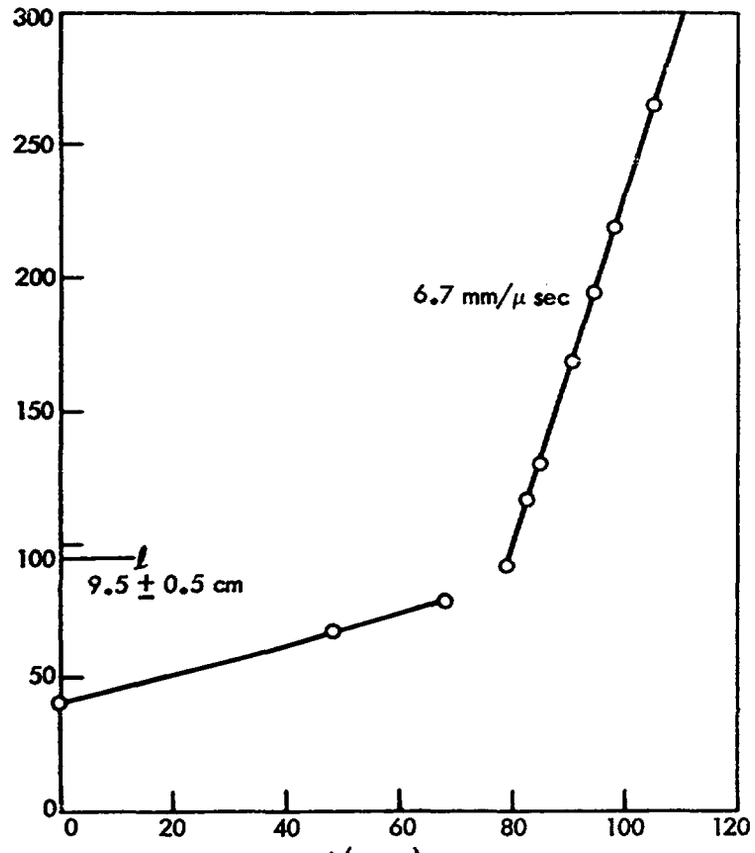

FIG. 34 DISTANCE - TIME DATA FOR 70.9% TMD 97/3 RDX/WAX (SHOT 218); DENSITY = 1.25 g/cc. (○ IP DISCHARGE TIME)

IV. DISCUSSION

A. Effect of Compaction in 91/9 RDX/Wax Mixture

1) Convective Flame Front

The experimental ionization probe data have shown that the first reaction front propagating beyond the ignition region travels at subsonic velocities (0.3 to 0.9 mm/μsec in the 70-90% TMD range). Simultaneous strain gage measurements have indicated that the pressure associated with this initial front is low (< 1 kbar). Consequently this reaction front has been classified as a convective flame front, identical to that observed by Griffiths and Groocock (5) in their work on DDT of porous, shock-sensitive explosives. Although there has been work devoted to characterizing the stability limits for convective burning, there have been no previous measurements in which the convective flame velocity has been studied as a function of charge density.

For the 91/9 RDX/Wax mixture, the convective flame velocity, r, has been found to increase with distance, x, travelled from the ignitor/explosive interface. Consequently, in comparing r as a function of charge density we must select first a value for x. We have calculated convective flame velocities from equation (4) using the values for the parameters B and C listed in Table 1. In Figure 35a the convective velocity is shown as a function of compaction for x = 41 mm. From 67 to 90% TMD, the convective velocity increases apparently linearly. However, at densities greater than 90% TMD, there is a sharp increase in slope. For values of x larger than 41 mm, the same type of behavior is observed. In Figure 35b we have plotted the convective velocity at the time of intersection of the convective front and PC wave, t_I, as a function of density. The same general trend as shown in Figure 35a is observed except that the curvature is more continuous.

Because of the sudden increase in r at densities above 90% TMD (Figure 35a), the question arises as to whether the rates above 90% TMD represent a convective flame front or a pseudo flame-front as found for the cast explosives (3). Our SG data show that the voltage-time profiles at 92.3 and 94.5% TMD (Figures 19 and 14, respectively) seem to follow the same general pattern interpreted in terms of a convective front and a postconvective (PC) wave found for lower densities. In addition, the trend from 90.1 to 94.5% TMD seems to be smooth (Figure 35a). It is of interest that the convective velocities for 92.3 and 94.5% TMD were the same at x = 41 mm and at x_I; this contrasts with the behavior at lower densities where the convective front accelerates. Our present conclusion is that convective burning occurs at all densities up to 94.5% TMD. However, as crystal density is approached, the stability of the convective front decreases sharply (due to inadequate gas reinforcement), but the rate increases due to more efficient heat transfer. This point is discussed more thoroughly at the end of this section.

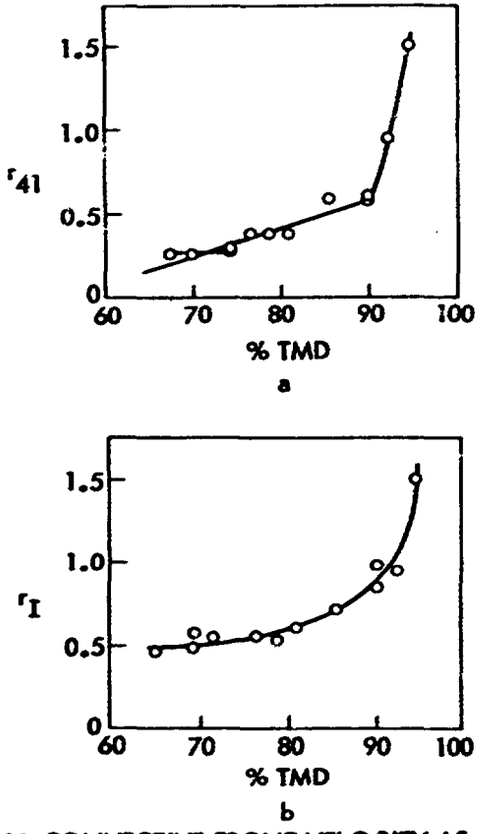

FIG. 35 CONVECTIVE FRONT VELOCITY AS A FUNCTION OF DENSITY FOR 91/9 RDX/WAX MIXTURE

a) VELOCITIES AT 41 mm b) VELOCITIES AT t_I

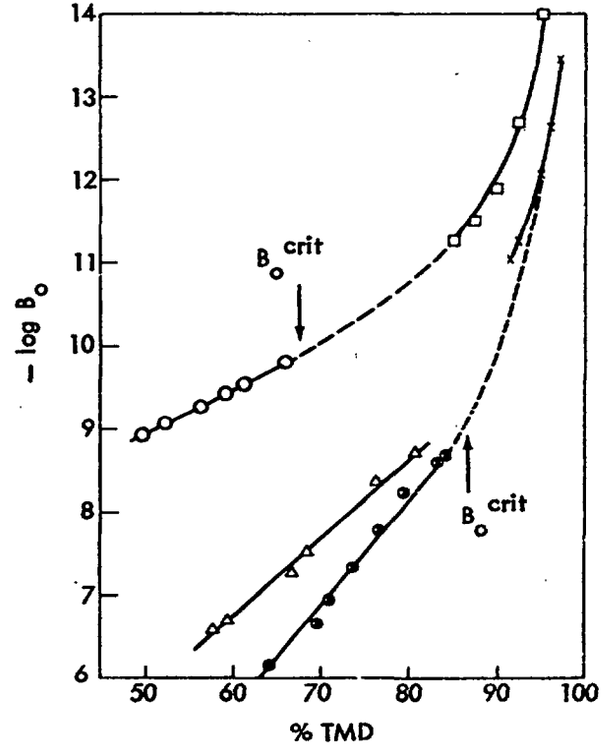

FIG. 36 EFFECT OF COMPACTION ON PERMEABILITY COEFFICIENT FOR PETN. x 550μ (REF. 7) □ 10-20μ (REF.7), O 5μ (REF. 16-AUTHORS' CURVE), △ 200μ (REF, 16), ⊗ 510μ (REF. 16)

The convective front velocities as shown in Figure 35a (i.e. at x = 41 mm) appear to be consistent with the analog of burning in a single crack or pore. Several investigators have published data on the propagation of convective burning in cracks for propellants with different compositions. Godai (21) used a polyester/-ammonium perchlorate propellant and observed that the burning rate in the crack increased as the crack separation decreased. Pressure was not held constant since propagation into the crack requires that an increasing critical pressure be exceeded with decreasing crack separation. His data were taken just beyond the critical pressure. Payne (22) used a propellant of unspecified composition but studied propagation into a crack at a constant pressure of 700 psi. He found that the flame propagation rate increased rapidly as the crack width decreased*. Bakhman (23) earlier had reported similar results for a Russian ballistic powder although his crack consisted of a separation between a glass wall and the ballistic powder. The maximum convective rate was found at a separation of 0.15 mm and it was 100 times greater than the linear (conductive) burning rate at the same pressure (0.1 kbar)**.

More recent Russian results, just available to us, extend the pressure range of the earlier studies of flame propagation in single pores. Belyaev et al (10) describe semiquantitatively the results obtained from studies of a constant pressure system which had been prepressurized with an inert gas. Without correlating results with the type of explosive or propellant studied, Belyaev et al schematically showed the variation of propagation rate along the length of closed (at the far end) and open pores. For the closed pore, the rate increases for about the first 20% of the path length before reaching a steady propagation rate. For the open pore, the rate increases to a much higher value during the first 45% of the pore length before it reaches a constant level. The authors (10) state that the propagation rate increases as the width of the pore decreases and also that increasing the length of the pore has the same effect as decreasing its width. For the constant pressure system, the authors list some propagation rates which increase from .055 mm/μsec for a 0.6 mm crack to 0.30 mm/μsec for a 0.2 mm crack. The corresponding maximum pressure at the bottom of the pore (crack) increases from 0.3 kbar to 1.8 kbar.

- - - - - - - - - - - - - - - - - - -

*At comparable crack separations, the flame velocities of Payne exceeded those of Godai by two orders of magnitude e.g., 356 mm/sec vs 2 mm/sec at a separation of 0.1 mm (pressure not constant).

**Although Bakhman did not give the linear burning rate of the ballistic powder, it is estimated to be at least 7 mm/sec.

Our convective velocity data for 91/9 RDX/Wax, as defined by the IP times, show that the velocity increases slowly with increasing distance from the ignitor/explosive interface* except for two instances, i.e., velocities at 92.3 and 94.5% TMD. This observation contrasts with the results of Belyaev at al (10) but, we think, only because our system is not a constant pressure system. The magnitude of our convective flame velocities are quite comparable to those reported by Belyaev at al (10) especially when we consider the variation in rates which may arise from compositional differences in explosives.

The literature results show that reasonably high convective burning rates can be obtained in single pores at modest pressures and that these rates increase with decreasing crack separation (or with decreasing pore size). Our data are obtained at varying densities. Since the pore size of the charges decreases with increasing density, our experimental results show that the convective velocity increases with decreasing pore size. Thus, our convective flame front velocity follows the same dependence on pore size as found for convective propagation within single pores. That is not to say that only pore size determines the convective velocity. Pressure in the pores will increase as the pore size decreases and this leads to a larger heat flux into the pore walls. Consequently, the velocity of the convective front in our study should depend, at the least, on both pore size and pressure.

The propagation of a convective flame front in a porous bed of explosive or propellant depends, in part, on the permeability of the charge (see section III.B for a more extensive discussion of convective burning). We have not made any permeability measurements as yet. However, two sets of permeability data for porous explosives are available in the Russian literature. We have taken these data, as displayed in graphical form in the translated papers, and reduced them to give the permeability measurements in consistent units as described in Appendix C of this report.

The permeability of a porous bed is characterized usually by measuring the flow of a fluid through the packed bed and calculating a permeability coefficient, B_o, as defined by the Darcy equation. The Darcy equation states that the rate of flow of a homogeneous fluid in a porous bed is directly proportional to the pressure gradient causing the flow, i.e.

$$u = \frac{Q}{At} = \frac{B_o}{\mu}\frac{dp}{dx} \qquad (8)$$

- - - - - - - - - - - - - - - - - -

*Equation (5) shows that with the selected data reduction equation (equation (2)), the convective velocity increases with the square root of the distance from the ignitor interface (i.e. $x \rightarrow \sqrt{x}$).

where u = linear fluid velocity, cm/sec
Q = volume of fluid flowing in time t, cm^3
A = cross sectional area of sample bed, cm^2
μ = viscosity of fluid flowing through the bed, g/cm sec
$\frac{dp}{dx}$ = pressure gradient across sample or increment of sample length, dyne/cm^3
B_o = permeability coefficient, cm^2

There is some confusion in the literature concerning the units of B_o. Workers in the oil industry in the early part of this century adopted a unit called the darcy, which is a mixture of cgs and other units. A darcy corresponds to the flow of one ml/sec through a cm-cube with a pressure difference of one atm/cm^2 between opposite faces, using a fluid with one centipoise viscosity. However, to avoid confusion it is best to use a consistent set of units, e.g., the cgs units. The units of B_o in equation (8) are cm^2 in the cgs units; a darcy equals 9.87×10^{-9} cm^2.

The Darcy equation, of which equation (8) is one form, is valid for viscous, laminar fluid flow. For equation (8) to be valid for gases, the pressure gradient, dp/dx, must be small to avoid compressibility corrections (see Carman (30) for a general discussion of gas flow through porous beds).

Andreev and Chuiko (16) measured a permeability coefficient for various explosives (e.g., PETN, tetryl, RDX) with various particle sizes. Their data, which covered the density range of 20 to 85% TMD, showed that the permeability decreased exponentially with increasing density, with minor exceptions. Their experimental data for 5-20μ, 200μ, and 510-550μ PETN are shown in Figure 36 (see Appendix C for a more thorough discussion and compilation of their data). The experimental technique of Andreev and Chuiko apparently met the criterion of a small pressure gradient across their samples since their pressure drop was reported in units of millimeters of Hg. Andreev and Gorbunov (27) measured a few additional permeability coefficients for a variety of explosives; these data are similarly contained in Appendix C.

Belyaev, Korotkov, and Sulimov (7) measured permeability coefficients for similar explosive systems (e.g. PETN and TNT). However, the data of Belyaev et al. were taken in the density range of 85 to 97% TMD. These data showed that the permeability coefficient decreased <u>more</u> rapidly than an exponential dependence on density in this higher density range (these data of Belyaev et al. are also compiled in Appendix C). We have plotted in Figure 36 the high density data of Belyaev et al. for 10-20μ and 550μ PETN. It is quite reasonable to join the two sets of permeability data (i.e., Andreev and Chuiko (16) and Belyaev et al. (7)) since the particle sizes are quite closely matched. The effect of particle size on B_o can be easily seen from the more complete data in Appendix C. At very small particle size ("microcrystalline") such as 5μ, B_o was independent of explosive composition at constant compaction (16).

We have connected the two sets of data in Figure 36 with a smooth dashed line. For both particle sizes it is apparent that the logarithm of B_o varies linearly with compaction for a given particle size only up to a critical density or a critical value of B_o (i.e., B_o^{crit}). Beyond B_o^{crit}, the permeability coefficient decreases very rapidly. This fact is consistent with the requirement that B_o become vanishingly small near 100% TMD. The data in Figure 36 show, in addition, that the material with the smaller particle size reaches its critical permeability coefficient at a higher porosity (lower density) than does the coarser material. This latter point is important in comparing the DDT behavior for different particle sizes and will be discussed later in section IV.A.5.

The permeability data as shown in Figure 36 are important since they can be used in the Darcy equation (equation (8)) to indicate how the laminar flow conditions change with varying compaction. For a constant pressure gradient, B_o is proportional to the gas (fluid) velocity, u, in the porous bed. Let us consider a constant pressure gradient and determine how u varies with compaction. Below B_o^{crit} u decreases slowly with increasing compaction. As B_o approaches and then becomes smaller than B_o^{crit}, the velocity of the flowing gases begins to decrease very rapidly until the flow becomes "choked" at high compaction where $B_o < B_o^{crit}$. For an increase in density from 90 to 95% TMD (where B_o decreases from 10^{-10} to 10^{-12} cm^2, respectively, for 510-550μ PETN), the flow velocity decreases by two orders of magnitude. Consequently, the term "chocked flow" is used to describe flow in the compaction region where the permeability coefficient is decreasing very rapidly (i.e., $B_o < B_o^{crit}$).

Although it is useful to define B_o^{crit} in considering the effects of charge permeability, it must be kept in mind that the Darcy equation (equation (8), which defines B_o) is valid only for conditions of laminar flow. These conditions are obviously not satisfied in the propagation of the convective flame front. For example, the order of magnitude of the gas velocity behind the convective front can be determined because the gas velocity producing convective burning must be greater than or equal to the convective flame velocity. In our experiments $u \geq r > 2 \times 10^4$ cm/sec. It is clear that the Darcy equation can not describe the pressure gradients within our system at such high flow velocities.

Carman (30) has discussed the extension of the Darcy equation to situations in which the gas flow within the porous bed is no longer laminar. As the gas velocity increases in a porous bed, the resistance to flow changes from viscous resistance to inertial resistance. The pressure gradient within the bed is related to the fluid velocity by the equation

$$dp/dx = a_o u + b_o \rho u^2 \qquad (9)$$

where a_o = viscous flow resistance coefficient = μ/B_o

b_o = inertial flow resistance coefficient

ρ = fluid density

The coefficients a_o and b_o are independent of the mechanical properties of the fluid and characterize the structure of the porous bed. The coefficient b_o is not a constant, according to limited data available, but depends weakly on u. It is apparent from equation (9) that for the evaluation of pressure gradients within the explosive beds, the permeability data of the Russians can serve to characterize one type of resistance to flow. It appears that the determination of inertial resistance is also important for a thorough evaluation of the packing of the explosive bed at conditions approaching our experimental conditions.

When the convective burning rate data, as shown in Figure 35a are considered along with the permeability correlations of Andreev et al. (16,27) and Belyaev et al. (7), one notices that the sudden increase in the convective rate starting just about 90% TMD correlates roughly with the choked flow conditions beginning at B_o^{crit}. That is, decreasing permeability coefficients parallel increasing convective flame velocities, and sharp changes in permeability coefficients (such as noted with increasingly high density) are reflected in sharp changes in the convective flame velocity and in other variables important to the buildup process necessary for DDT (see section IV.A.5). Based upon this interpretation, it appears that the permeability data obtained at very low flow velocities (laminar flow) are sufficient to characterize qualitatively the dependence of the convective flame velocity on charge compaction.

2) Detonation Velocity

In addition to measurements of the convective flame front velocity, our ionization probes discharge times have allowed us to measure the detonation velocity for experiments where DDT was observed. The detonation velocities for 91/9 RDX/Wax are shown in Figure 37 as a function of compaction. Although there is considerable scatter in the data (error bars in Figure 37 represent $\pm$ twice the standard deviation), there appears to be linear relationship between D and % TMD. A least squares treatment of the raw data (i.e., without weights) yields the equation

$$D = 0.1847 + 8.403\,\Delta \qquad (10)$$

The infinite diameter detonation velocity vs Δ ($\equiv \rho_o/\rho_v$) curve has not been characterized very well for 91/9 RDX/Wax. Working

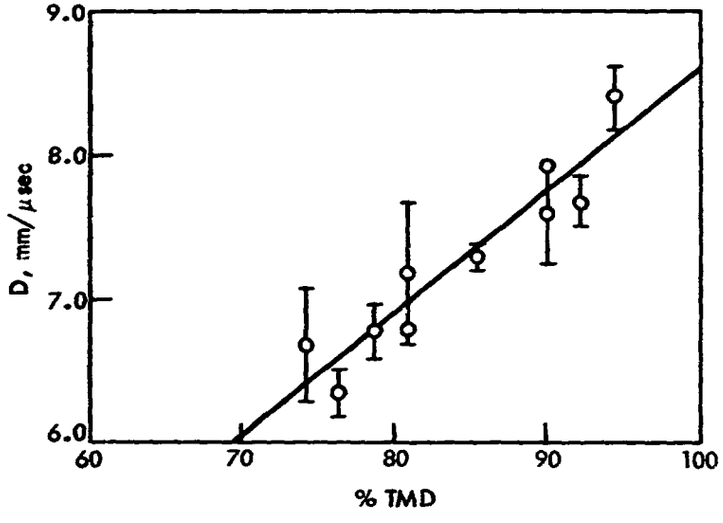

FIG. 37 DETONATION VELOCITY OF 91/9 RDX/WAX AS FUNCTION OF COMPACTION. [D = 0.1847 + 0.08403 (% TMD)]

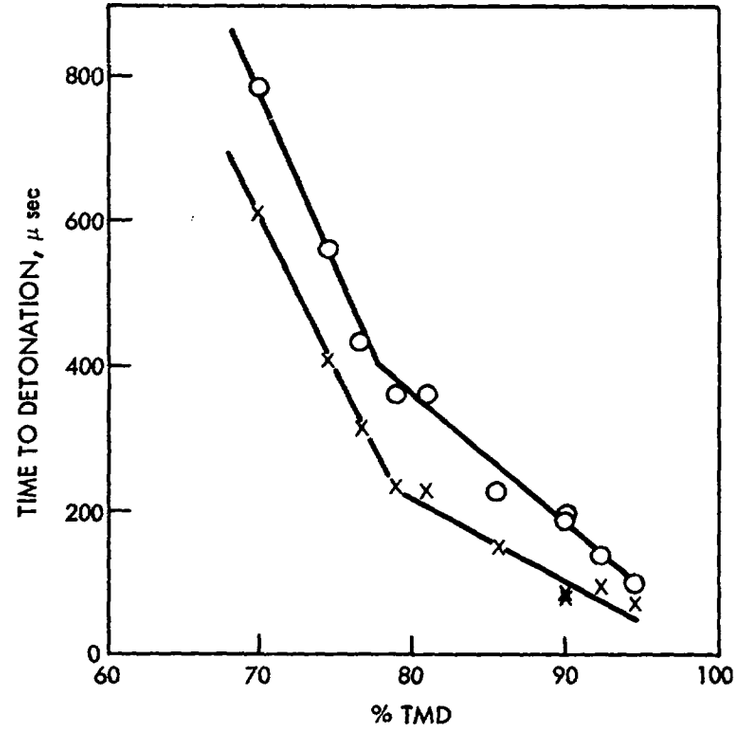

FIG. 38 TIME TO DETONATION AND RELATIVE TIME TO DETONATION FOR 91/9 RDX/WAX AS FUNCTION OF COMPACTION. (x = Δt_D, O = t_D.)

with unconfined charges in the range of 3.7 - 4.1 cm diameter and densities of 0.92 - 1.61 g/cc, Coleburn and Liddiard (14) found

$$D_i \simeq 1.62 + 6.943\ \Delta \qquad (11)$$

As the effective charge diameter decreases, the intercept value also decreases while the slope increases (8). For example in the high confinement of a steel cylinder (0.2 in. ID, 1.0 in. OD), Hampton (20) obtained the curve

$$D = -1.86 + 10.5\ \Delta \qquad (12)$$

Although we do not know the effective diameter of H.E. in the DDT tube, the earlier work suggests that the D vs Δ curve should be linear with coefficients comparable to those of equation (12) rather than equation (11). This is exactly what we have found. It should be noted that the present experimental setup is not the optimum design for precise measurement of detonation velocity. In addition, in cases where the onset of detonation is near the far end of the tube, the detonation run is relatively short, and hence, less precisely measured. The time interval associated with this detonation run is also very small and even more difficult to measure.

3) Time to Detonation

In any study of detonation phenomena, an important quantity is the time to detonation relative to the initial application of stimulus. In our case, this is the time from ignition of the explosive charge at the ignitor interface to the point at which detonation started. Unfortunately, this time to detonation cannot be accurately calculated because we have not recorded events from the ignitor/explosive interface*. However, we can calculate an approximate time to detonation by extrapolating the convective burning curve, as seen in the distance-time plane, back to the ignitor interface (i.e., x = 0). This time to detonation, t_D, is shown in Figure 38 as a function of compaction. We also have plotted in Figure 38, a relative time to detonation, Δt_D, which is the time to onset of detonation relative to the arrival of the convective flame front at 41 mm.

In Figure 38, t_D and Δt_D follow the same general trend. There appears to be two distinct linear regions in this time-compaction plane, although both regions show that increasing porosity increases the "time to detonation". The change in slope for the two regions occurs at 78 ± 2% TMD. Calling the region between 94.5 and 78% TMD the "normal" region it appears that for charge densities less than 78%, detonation occurs later than normal**. This trend is consistent

- - - - - - - - - - - - - - - - - - -

*In studies where confinement of the combustion gas is important, the ignition region should be free of instrumentation probes which may perturb the buildup process.

**If the region between 70 and 78% TMD showed a "normal" dependence of time to detonation on compaction, t_D would be zero for densities above 87% TMD!

with mechanistic considerations to be presented below in section IV.C.

The longest estimated time to detonation, 790 μsec, which occurred for a charge density of 69.8% TMD, is a very small fraction of the total time to initiate burning of the explosive charge. We have measured, in a limited number of shots, the time interval between the actuation of the ignitor current and the arrival of the convective front at x = 41 mm. This time interval varied between 10 and 20 msec. If we compute a linear (conductive) burning rate from this data, we find a linear rate for the ignitor mixture of 31 to 63 cm/sec (i.e., 6.3 mm divided by 10-20 msec). Although we do not have any burning rate data for the B/KNO_3, the computed linear rate seems very high, even for a pressure of 1 kbar. Consequently, the time interval of 10 to 20 msec appears to be associated entirely with the ignition and burning (probably turbulent burning) of the B/KNO_3 mixture.

4) Postconvective Wave

For the 91/9 RDX/Wax mixture, the strain gage voltage-time data have indicated that some time, t_E, after the passage of the convective wave at location x, the pressure at that location suddenly increases more rapidly than linearly and continues to increase well beyond 4.5 kbar*. In the earlier description of records for individual shots (section III.C.1), we found that the SG data (which gives a time of excursion, t_{PC}, for the x location of the SG) produced a linear curve which we defined as the postconvective wave. Its velocity (V_{PC}) and the corresponding charge density for each shot are listed in Table 2 and plotted in Figure 39. It is quite apparent that the data are not randomly distributed but that they suggest two different types of behavior with a cross over point at about 80% TMD.

In the distance-time plane used to evaluate the ionization probe data, the SG data suggest the propagation of a compressive wave, the PC wave, through the burning granular bed. Such a wave should propagate at the local sound velocity of the burning bed. Unfortunately these sound velocity data are not available and, indeed, there are few literature data which correlate the sound of porous explosive charges with density.

The longitudinal sound velocity of a porous bed of particles generally decreases with decreasing density. Data showing this dependence have been reported by Reese et al. (24) for ammonium perchlorate and Lindstrom (25) for tetryl. The sound velocity of ammonium perchlorate showed a large particle size effect which was not evident in companion measurements on potassium chloride by Reese et al. (24). The ammonium perchlorate data are fragmentary and do not really supply

- - - - - - - - - - - - - - - - - - -

*4.5 kbar (~35 mv) represents the upper pressure limit in our theoretical internal pressure-strain calculations (see Appendix A).

TABLE 2

SUMMARY OF POSTCONVECTIVE WAVE VELOCITIES AND ESTIMATED LONGITUDINAL SOUND VELOCITIES FOR 91/9 RDX/WAX

Shot No.	Density		Vel. of PC Wave (V_{PC})	Estimated Longitudinal Sound Velocity (Figure 40) V_L^o	$\frac{V_{PC}}{V_L^o}$
	%TMD	g/cc	mm/μsec	mm/μsec	
304	94.5	1.588	1.9_5	2.3	0.85
316	92.3	1.551	1.6	2.1_5	0.74
305	90.1	1.513	1.6_5	2.0_5	0.80
306	85.5	1.437	1.3	1.7_2	0.76
317	81.0	1.361	1.3_5	1.4_5	0.93
315	78.8	1.324	1.1	1.3_5	0.81
312	76.5	1.286	1.6	1.2_2	1.3
307	74.3	1.248	1.8	1.1	1.6
225	69.8	1.172	1.9	0.9	2.1

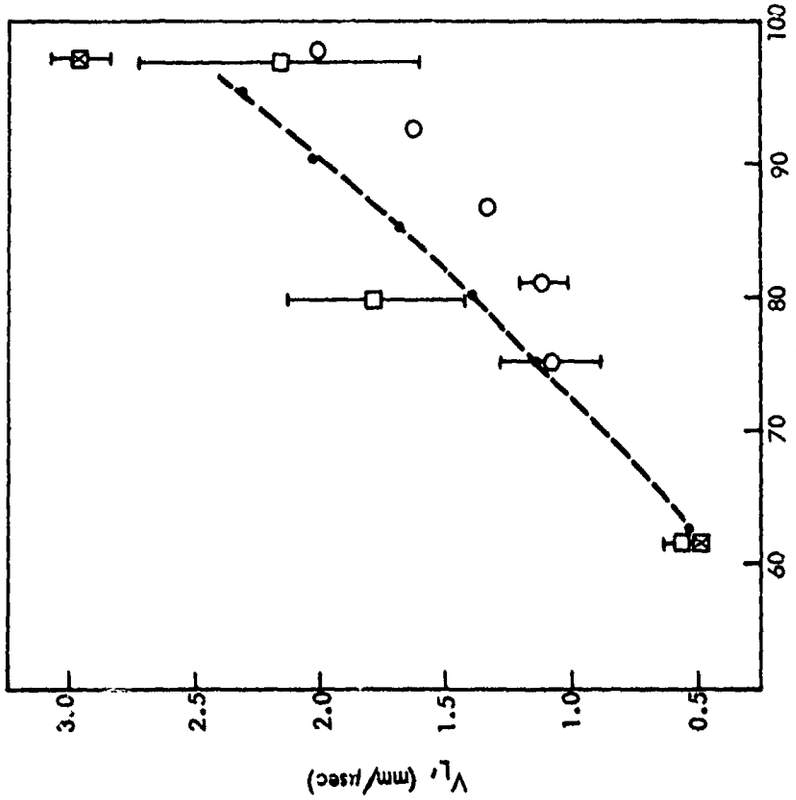

FIG. 40 LONGITUDINAL SOUND VELOCITY FOR VARIOUS EXPLOSIVES AS FUNCTION OF COMPACTION. ⊡ TETRYL (REF. 25) □ 500μ AP (REF. 24) ⊠ 76μ AP (REF. 24) ● ESTIMATED V_L° FOR RDX/WAX MIXTURES (THIS STUDY)]

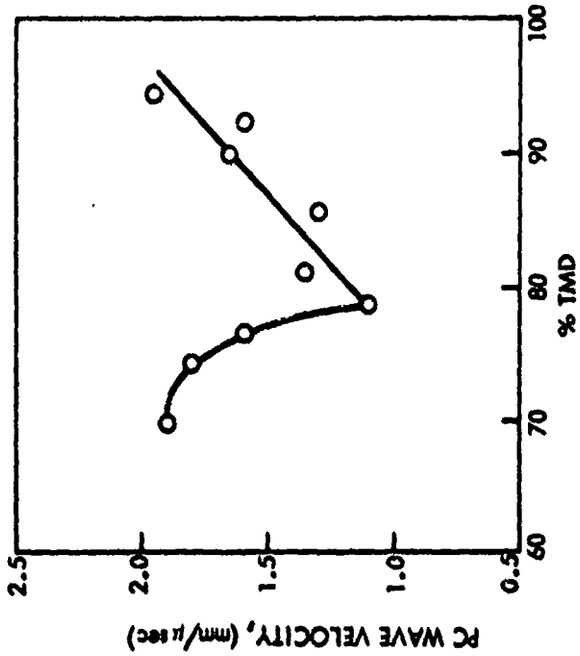

FIG. 39 POSTCONVECTIVE WAVE VELOCITY FOR 91/9 RDX/WAX AS FUNCTION OF COMPACTION.

us with very much information in the porosity region and particle size region of our experiments. The sound velocity data reported by Lindstrom in his paper on the shock initiation of porous tetryl (25) are more useful chiefly because they cover our range of porosity more thoroughly. The tetryl data show very nicely the decrease in sound speed expected with decreasing charge compaction. Lindstrom did not give a mean particle size for his material but from its photomicrograph (25), the average particle size is at least 500μ. This is greater than our estimated particle size of RDX (200μ) and the wax (125μ).

We have plotted the longitudinal sound velocity data for ammonium perchlorate (24) and tetryl (25) in Figure 40. In addition, we have used these data to estimate longitudinal sound velocities for our RDX/Wax mixtures based on porosity variations. The estimated longitudinal sound velocity curve for the RDX/Wax mixture is shown by the dashed curve in Figure 40.

Since we have a burning pressurized porous bed, we must also consider the temperature effect on sound velocity and how the sound velocity varies as the interstitual gas pressure of the porous bed increases. We have not been able to find any data for a hot, porous bed of organic particles. For nonporous solids, the general trend is that the sound velocity decreases with increasing temperature. However there are cases where there is a maximum in the sound velocity-temperature plane. We have assumed that an increase in temperature for a porous bed of particles will result in a decrease in sound velocity. We have been unable to locate any data for sound velocity in porous beds as interstitual gas pressure increases. Our assumption is that sound velocity should increase very slightly with increasing interstitual gas pressure at a constant temperature. Consequently, the overall effect on sound velocity of a porous bed of increasing the bed temperature and introducing high pressure interstitual gases should be to decrease the ratio of sound velocity in the hot pressurized bed to the sound velocity in the initial cold unpressurized bed. This reasoning is in line with the ratio of V_{PC}/V_L^o for the higher density data in Table 2*.

We have collected the data for the velocities of the PC wave and estimated longitudinal sound velocities for our initial cold bed in Table 2. It is evident that at charge densities greater than about 78% TMD, the PC wave travels at sonic or subsonic velocities. However, the PC wave velocities at 76.5, 74.3, and 69.8% TMD are definitely supersonic relative to sound velocities in the initial cold bed of explosive. The only way we can explain the high value of (V_{PC}/V_L) at the densities less than about 78% TMD is to assume that the porous bed has been compacted by the pressure gradient

- - - - - - - - - - - - - - - - - - -

*If the amplitude of the compressive wave exceeds the yield strength of the explosive, it should travel at the bulk sound speed $c < V_\ell$.

$\Delta p/\Delta x$ some time before the PC wave originates, but after the passage of the convective wave. Hence the PC wave travels through the compacted material at its sound velocity which is considerably higher than that of the initial porous material. We can measure a voltage difference (and hence calculate a pressure difference Δp) between the two strain gages at the far end of the tube for the three lowest density runs (Shots 312, 307, and 225) at times before the PC wave is formed. Unfortunately Δx is large, varying from 60 to 110 mm. The values for Δp are small, 0.1 to 0.5 kbar (assuming 5.7 mv equals 1 kbar), depending upon the time of measurement and the charge density. If we consider the pair of far SGs which was spaced more closely ($\Delta x < 50$ mm), Δp varies similarly, from 0.2 to 0.6 kbar. These pressure differentials may be considered too small to explain compaction of the charges, but this does not seem to be the case. From the few compressive strength measurements available we find that, at the same % TMD and at room temperature, tetryl is stronger by a factor of 2 (or more) than RDX which, in turn, has a greater compressive strength than 91/9 RDX/Wax. Presumably the elastic pressure limits (P_{EL}) would also show the RDX/Wax weaker than tetryl. Lindstrom (25) measured P_{EL} for tetryl at 75 - 98% TMD. From his data, the values in the range where we suggest charge collapse (i.e. 70 - 80% TMD) are 0.25 - 0.36 kbar; hence P_{EL} for RDX/Wax should be even less, and well within the range of Δp measured. To be sure, pressurized charges might be expected to have a higher P_{EL} than unpressurized, but hot pressured charges would be expected to have a lower P_{EL}. Heating RDX/Wax, 91/9, from 23°C to 71°C decreases its compressive strength to 0.15 its initial value.

In the presence of flowing combustion gases, it is conceivable that compaction of the very porous charges starts as a slow time-dependent process which accelerates with increasing time. The time interval before the PC wave is detected in these charges is 150 - 500 μsec (see Appendix B). The simple law of motion, $F = ma$, shows that this is adequate time for the observed pressure gradients to initiate compaction in charges with elastic limits of the order of magnitude of 0.1 kbar. The longer the available time, the more complete the compaction. Hence we find V_{PC}/V_L^o greatest at the lowest compaction, initially 70% TMD (see Table 2).

It remains to be explained why V_{PC}/V_L^o is less than one at % TMD ≥ 78.8. It has already been mentioned that this might be the result of temperature and pressure effects on the sound velocity of porous charges. However, in his work on porous tetryl charges, Lindstrom used the impact of a brass driver plate on a room-temperature, unpressurized charge. He found that the maximum velocity of the precursor transmitted to the charge by the elastic wave from the driver was (on the average) 0.83 times the longitudinal sound velocity of the charge. This he attributed to dispersion of the shock front by the porous charge, a factor equally probable in the present case. Lindstrom's ratio max.vel./V_L^o is close to the values of V_{PC}/V_L^o of Table 2 (% TMD ≥ 78.8), probably for much the same reason.

The strain gage records indicate that the PC wave is compressive; by the arguments given above, it propagates at the sonic velocity of the burning explosive charge. There is additional evidence that the PC wave is not only a compressive disturbance but is a part of the process of build up to the shock necessary to initiate the observed detonation. The relevant observations are (1) that IP discharge times beyond the convective wave front lie on the path of the PC wave, and (presumably in a transitional region); (2) the curvature and slope (dE/dt) of the SG curves at $t > t_{PC}$ increases with increasing x -- in other words the PC wave front appears to sharpen as it propagates. Both observations are consistent with identifying the PC front as the first detectable compressive disturbance in building up an initiating shockwave. (See last section of Appendix B.)

One characteristic of the PC wave which we have discussed only qualitatively so far is t_E, the time interval between the passage of the convective flame front and the PC wave. Since t_E decreases with increasing x, at constant charge density, we must choose a specific value of x whenever we compare t_E as a function of density. Consequently, we have selected three values of x and compared the t_E-% TMD plane for these three x values. Figure 41 shows the variation of t_E with density at 41 mm and 80 mm while Figure 42 shows this variation at $\ell/2$. Basically, the data in Figures 41 and 42 show the same feature; namely, there are two linear regions which seem to intersect near 78% TMD. Our interpretation of this behavior is that for densities lower than about 78% TMD, the PC wave is not formed as early as expected, based upon the higher density data, because it is formed, not in the usual sequence of events, but only after compaction of the porous bed has begun. This hypothesis has important mechanistic implications which are discussed in Sections IV.C.1 and 2.

5) Predetonation Column Length

The distance (from the ignitor/explosive interface) at which detonation was detected has been found, in the experimental results section, to vary with charge density. We have called this distance "the predetonation column length", ℓ, and it includes the charge length in which convective burning propagates as well as any transition zone*. Figure 43 shows the trend observed for ℓ with decreasing

- - - - - - - - - - - - - - - - - -

*It has been postulated for many years that all detonations are shock initiated. Consequently, there is a time (called an induction or delay time) and a distance (called a run-up distance) which separates, in shock to detonation transition work, the formation of a precursor shock and the onset of detonation. We classify here, for semantics sake only, a transition zone as the region beginning with the formation of the precursor shock and ending with a steady state detonation wave.

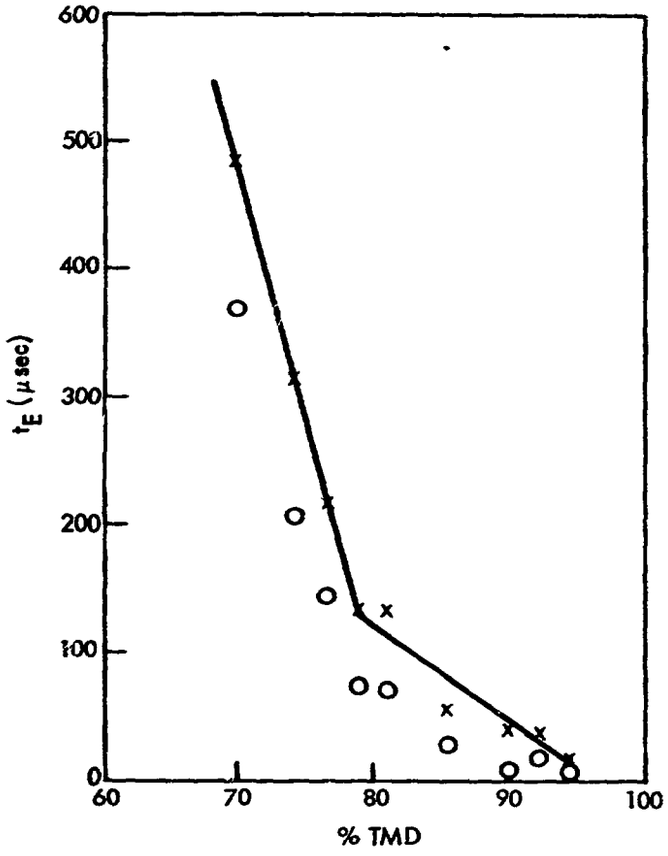

FIG. 41 TIME INTERVAL BETWEEN PASSAGE OF CONVECTIVE FRONT AND PC FRONT, t_E, FOR 91/9 RDX/WAX AS FUNCTION OF COMPACTION FOR LOCATIONS AT 41 mm AND 80 mm (x 41 mm LOCATION, O 80 mm LOCATION).

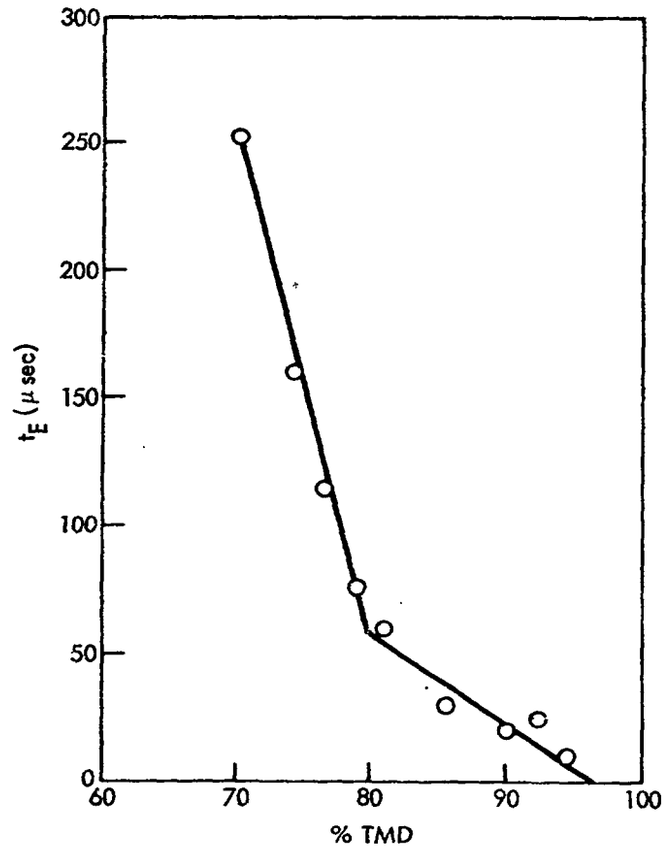

FIG. 42 TIME INTERVAL BETWEEN PASSAGE OF CONVECTIVE FRONT AND PC FRONT, t_E, FOR 91/9 RDX/WAX AS FUNCTION OF COMPACTION FOR $x = \ell/2$ LOCATION.

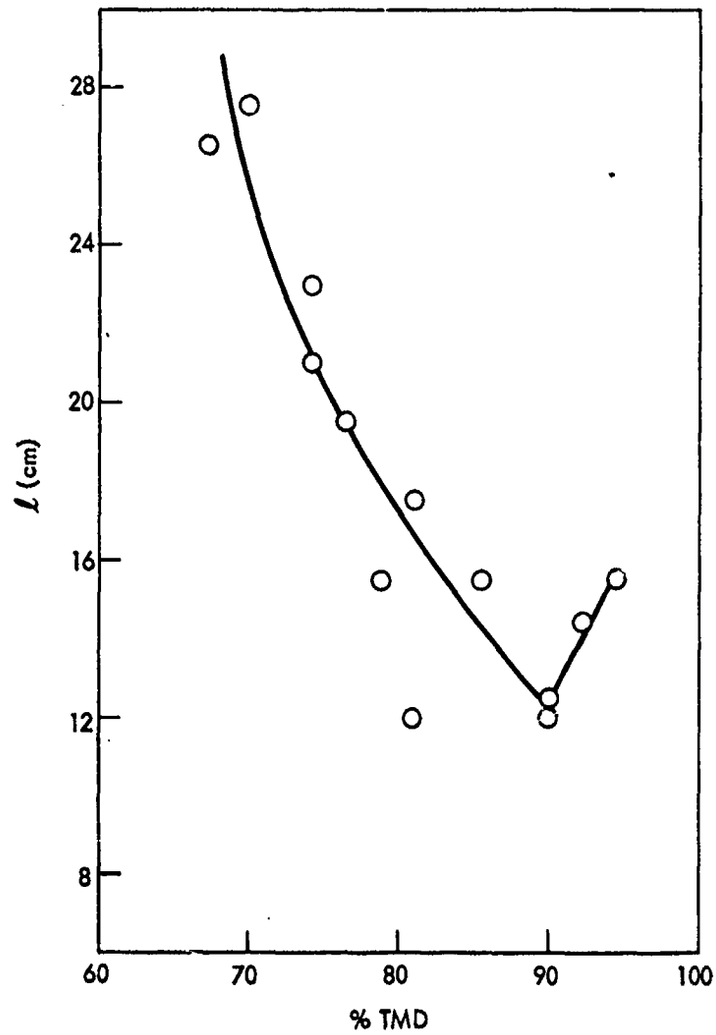

FIG. 43 PREDETONATION COLUMN LENGTH FOR 91/9 RDX/WAX AS A FUNCTION OF COMPACTION

density. The data suggest that there is a minimum at approximately 90% TMD (note that one charge at 94.5% TMD failed to show transition to detonation). However, with the present scatter in our data it is impossible to eliminate the possibility that there may be a plateau region for densities greater than 85% TMD. Nevertheless, it is quite apparent that below 85% TMD, the predetonation column length increases with decreasing density.

A minimum in the ℓ-% TMD plane at constant initial particle size was qualitatively described by Griffiths and Groocock for RDX, PETN, and HMX (5). Their explanation for the minimum in the ℓ-% TMD curve was based upon a minimum found in the correlation of ℓ with permeability for charges of different densities. Unfortunately, Griffiths and Groocock did not report how permeability varied with charge density. When we use the permeability data of Andreev et al. (16,27) and Belyaev et al. (7) (see Appendix C and Section C.1) we find that the data of Griffiths and Groocock, as shown in the "ℓ-permeability" plane, reduces to the type of curve represented by the solid lines in Figure 43. However, ℓ for these authors did not vary over such a wide range as they worked with more "sensitive" materials than we have; the minimum also appears to be at a lower density.

Korotkov et al. (28) have recently published a report on DDT in porous explosives but the translated text is not available at the present time. However, their results for PETN are very nicely summarized in a figure showing the variation of ℓ with density. The range of ℓ covered 2 to 5 cm for particle sizes of 20 μ and 500 μ! For the 20 μ material, they surmised a minimum in ℓ at 60% TMD while the minimum for the 500 μ material is at about 75% TMD. The minimum value of ℓ was 2 cm in both instance. Thus, the DDT results reported in the literature for shock-sensitive secondary explosives show conclusively a minimum in the ℓ-density plane. Whether the same holds for less shock-sensitive materials has not been unambiguously demonstrated here.

When the ℓ-% TMD data for PETN as reported by Korotkov et al. are analyzed in conjunction with the permeability data for PETN as reported by Andreev et al (16,27) and Belyaev et al. (7), we discern another type of correlation between ℓ and permeability besides that noted by Griffiths and Groocock. As mentioned earlier (Section IV.A.1) on the discussion of the convective flame rate dependence on permeability, the reported permeability data show the presence of choked flow at the lower porosities. In addition, the onset of choked flow appeared to begin at a higher porosity for the 5 - 20 μ PETN then for the 510 - 550 μ PETN. Values of ℓ for PETN as reported by Korotkov et al. had a minimum at a higher porosity for the 20 μ PETN than for the 500 μ PETN. These data suggest that a minimum in the ℓ-density curve reflects the influence of choked flow. Having defined earlier the permeability value at the onset

of choked flow as B_o^{crit}, we find the following approximations. For $B_o < B_o^{crit}$ ℓ decreases with increasing porosity (higher density region). For $B_o > B_o^{crit}$ ℓ increases with increasing porosity (lower density region). With increasing porosity, the disappearance of choked flow signals the enhanced capability of the gas phase to transport energy to the unburned explosive. Thus, the change in gas flow properties of the porous bed correlates with a change in the dependence of ℓ on compaction. We feel that a minimum in the ℓ-% TMD curve reflects a change in the buildup process leading to the precursor shock necessary to effect DDT. The role played by energy transport via the gas phase is discussed more thoroughly in Section IV.C.2.

6) Ratings for Sensitivity to DDT

Rating the sensitivity of explosive materials to DDT (i.e., to undergoing a transition from burning to detonation) is not a part of the reported work which is concerned with elucidating the DDT processes. Of course, the present experiment is capable of dividing all explosives into two groups: those capable of exhibiting DDT in the set-up of Figure 1 and those which are not. Such a single division into two large classes is hardly a quantitative rating. Moreover, the present experiment is unable to rate the various compactions of RDX/Wax, 91/9, except that they all exhibit DDT in our set-up. Because ℓ and t_D have both been erroneously used in the literature as indices of sensitivity to DDT, it seems relevant to discuss why they are not such indices.

The predetonation column length ℓ includes, as a small fraction, the "run-up length" X. We have mentioned before that X is of the order of magnitude of the small separation between the intersection of the convective front with the PC front and the point at which detonation begins. Similarly, t_D includes the "time to detonation" τ. Sufficient work has been done on the shock-to-detonation transition so that it is generally recognized that neither X nor τ alone is any measure of shock sensitivity. In other words, a very sensitive explosive and a very insensitive explosive will show the same value of X provided the initiating shock (P_i) is sufficiently stronger for the insensitive material. Thus P_i and X (or P_i and τ) must be used to obtain a shock sensitivity rating. (See, for example, Reference 25.)

In the case of DDT, the length ℓ consists chiefly of a column of ignited explosive which has been burning different lengths of time according to location along the column. Although we have followed the pressure-time history at several locations, we have as yet no way to estimate from these data, the strength of the shock that will be formed. It is the pressure-time profile of that shock which provides the stimulus to the unburned explosive and finally initiates detonation.

Some of the factors which will affect the length of column necessary to produce an initiating shock are the explosive's ignitability, its burning rate, the amount of gas it can produce, the temperature and pressure of the gas, and the flow of hot gases and available burning surface permitted by the charge permeability. For the single composition (91/9), the mass burning rate and flame temperature will be constant. If we vastly oversimplify by considering only the total energy potentially available, this should increase with increasing compaction, i.e., with an increasing amount of explosive in the column. Then to reach the same total energy in each case, ℓ should vary in some inverse fashion with compaction. As Figure 43 shows, it does just this up to 90% TMD.

So the trend observed from ℓ is reasonable, but it is not the trend for sensitivity to DDT. It has been known for some time that porous charges exhibit DDT more easily than compacted ones (4,29). This fact was confirmed by a series of measurements of burning powders in bombs fitted with membranes rupturing at different pressures and by following p-t of the burning charges in a manometric bomb*. A variant of the series of graduated blow-out discs would be to vary the confinement of the present set-up to measure minimum confinement necessary for DDT to occur. Then all explosives exhibiting DDT in the original set-up might be ordered for sensitivity in terms of decreasing critical confinement.

Another possible method of rating for sensitivity to DDT is loading insensitive materials with the burning of a non-detonating, rapid burning, gas loader; we are currently studying this technique. It is related to another possible method: determining the critical amount of gas loader (or inert material) that must be admixed with the charge to effect (or to prevent) DDT. It might also be possible to use a critical temperature (without gas loaders or heat sink components) for a rating. But in order to choose a method, and to design a test to produce quantitative sensitivity ratings, we must continue our present investigation until we better comprehend the transition processes. We intend to apply our understanding of DDT to such test design.

- - - - - - - - - - - - - - - - - - -

*These measurements did not give quantitative DDT results; it is quite possible that detonation was not achieved in every case. However, increased ability to exhibit DDT with increasing porosity is an acceptable concept because porous charges, by virtue of increased reactive surface, show much greater ease of ignition and burning.

B. DDT Behavior for RDX/Wax Series at 70% TMD and for Ammonium Picrate

From our discussions in the previous sections, it is apparent that different processes and hence different mechanisms may be operative in the predetonation period at different compactions. If we are comparing two different explosives, then in the special case where the permeability and specific surface are the same and in a region where gas flow serves as the chief mechanism of initiation, the predetonation column length ℓ or time to detonation should serve as a rating of sensitivity to DDT. This special case is approximated by the RDX/Wax series at 70% TMD since the same lot of RDX was used throughout and the percentages of wax are small.

The data in Table 1 for 97/3, 94/6, and 91/9 RDX/Wax at about 70% TMD show that both t_D and ℓ increase with increasing wax content. This observation is in line with a) decreasing chemical energy to be expected with increasing dilution with wax and b) an assumed increase of t_D with decrease in available energy released, other conditions being constant*. The large differences between 94/6 RDX/Wax and 91/9 RDX/Wax for t_D and ℓ in Table 1 suggest that a higher wax content mixture (e.g. 88/12 RDX/Wax) may be unable to undergo DDT at 70% TMD, at least in our system. It should be recalled that ammonium picrate has already been shown to be unable to undergo a transition in our system, both at 70% and 90% TMD**.

Although ammonium picrate has been found to be unable to undergo a transition to detonation with its own gas loading in our system, we have demonstrated that ammonium picrate at 70% TMD can exhibit DDT with a small layer of nondetonating gas loader located between the ignitor and ammonium picrate charge. In these early survey experiments, we used about a 9 mm layer of RDX (density about 70% TMD) as the auxiliary gas loader. The mechanism by which such a thin layer of nondetonating gas generator can induce DDT in an acceptor explosive is of prime importance in understanding DDT in porous granular explosives.

- - - - - - - - - - - - - - - - - -

*It is interesting to note that the convective velocity decreases in the order 97/3 > 94/6 > 91/9, a trend identical to that expected for linear (conductive) burning rates and in agreement with the above concepts.

**Two DDT experiments have been run at 70 and 90% TMD with porous Composition B (60/40/1 RDX/TNT/Wax) in our system. The results were ambiguous with respect to ionization probe distance-time correlations. However, the recovered tubes indicated that Composition B did not undergo DDT whereas RDX/Wax, 91/9, at comparable densities did. On the other hand, Composition B appeared to produce a more vigorous reaction than did Explosive D since the tubes were split axially into two symmetrical pieces in contrast to a simple pressure burst at the ignitor end (see Figure 2).

C. DDT Mechanisms

1. DDT Mechanism for 91/9 RDX/Wax

The experimental results of the deflagration to detonation study herein allow us to postulate a skeletal DDT mechanism for 91/9 RDX/Wax. The first step is ignition of the explosive at the ignitor interface. The burning mode observed 30 to 40 mm beyond the interface is the convective flame front discussed by Griffiths and Groocock (5). The convective flame front, at densities equal to or less than 90% TMD, propagates in a mildly accelerating manner. The pressure associated with the "head" of the convective front appears to be less than a kilobar. A disturbance, called the postconvective wave, is formed in the ignitor region sometime after the passage of the convective front. Travelling at a relatively faster velocity through the burning bed, this PC wave can and does overtake the convective flame front. [In a few experiments an ionization probe, positioned just beyond this point of intersection of the convective and PC fronts, discharged at a time consistent with the path of the PC wave.] Only after the PC wave has overtaken the convective front is detonation observed at some point beyond (detonation occurs 1 to 2 cm and 10 to 20 μsecs after the intersection of the two fronts). The precursor shock necessary to initiate the cold unburned explosive ahead of the convective front is believed to be formed behind the PC wave as a result of a coalescence of compressive waves. Consequently, the beginning of the transition zone (i.e., the point of formation of the precursor shock) is not yet exactly known. Figure 44 summarizes the DDT mechanism for 91/9 RDX/Wax based on the experimental data.

The mechanism responsible for the formation of the PC wave is also unknown. But it should be dependent upon explosive composition and, as we have seen, on density. At the higher densities, the PC wave may form as a result of the generation of gas within the pores (after the passage of the convective front). These gases may not be able to flow rapidly enough to lower pressure regions within the porous bed because of the low permeability of the bed. Consequently, an increasingly rapid pressure buildup results and produces the PC wave and, perhaps, additional compressive waves. However, for lower density charges (< 78% TMD) of 91/9 RDX/Wax, we have suggested that the formation of the PC wave involves an additional process, i.e., compaction of the porous bed. Experimental data which support this suggestion are the change in the effect of compaction on the velocity of the PC wave at about 80% TMD (Figure 39) and on the time interval, t_E (Figures 41 and 42). The fact that t_D and Δt_D show similar changes confirms our more general conclusion that the presence of the PC wave is necessary before a transition to detonation will occur. However, we have only demonstrated a PC wave in the case of 91/9 RDX/Wax. Additional experimentation is needed to test this supposition for other RDX/Wax mixtures and other shock-insensitive explosives.

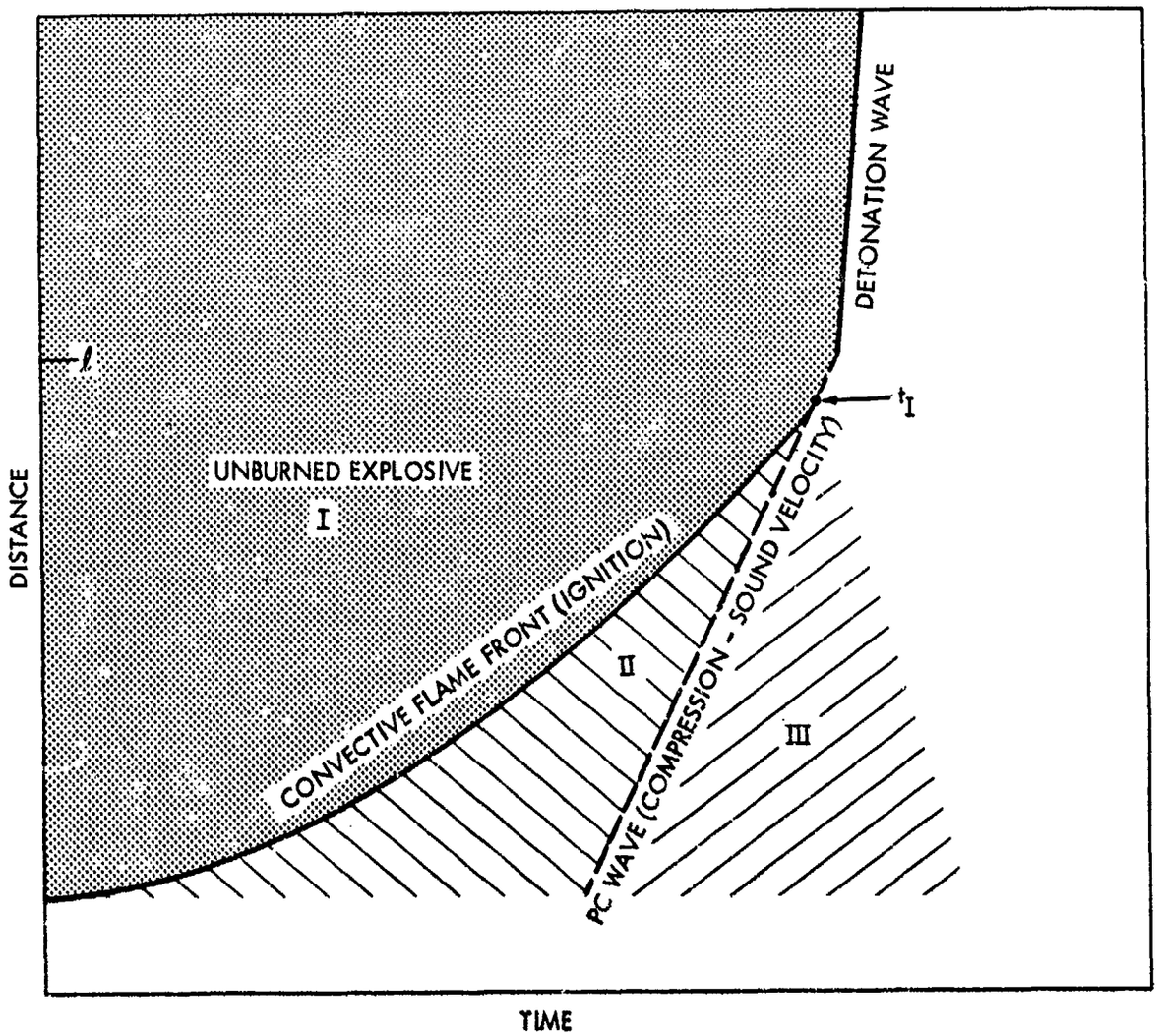

FIG. 44 PROPOSED DDT MECHANISM FOR 91/9 RDX/WAX GRANULAR CHARGE.

REGIONS:

I. UNDISTURBED GRANULAR BED AT INITIAL COMPACTION.

II. EXPLOSIVE BURNING TO GIVE LINEAR INCREASE OF PRESSURE WITH TIME; COMPACTION OCCURS WITH THE MOST POROUS CHARGES.

III. ACCELERATED BURNING AND PRESSURE BUILDUP TO FORM PRECURSOR SHOCK.

2. DDT Mechanisms for Explosives

As a result of the present experimental results, based principally on 91/9 RDX/Wax, and earlier DDT work on both porous and cast explosives, we are able to propose a fairly consistent picture for the DDT mechanisms of permeable and nonpermeable explosive charges. This presentation will be helpful in outlining areas where additional work is necessary to check our understanding of the many factors influencing DDT. We shall now consider the sequence of events as porosity is introduced into the explosive column. .

Case A (Impermeable Charges)

Subsection 1) (100% TMD and Cast Charges)

At crystal density (100% TMD) there is no porosity and, of course, the charge is impermeable; the latter is also true for cast charges. Hence, the ability of the explosive to undergo DDT will be determined by the criteria outlined in the cast explosives work (1, 3). To summarize briefly again, a) there must be a sufficiently rapid pressure rise in the ignition region caused by the generation of high product gas pressures and b) the unburned explosive beyond the ignition region must be sufficiently sensitive to be initiated by a shock wave equal in amplitude to the high pressures generated near the ignitor. Consequently, the distance to the onset of detonation, ℓ, and the time to detonation, t_D, decrease as d^2p/dt^2 increases.

The first criterion, (a), which pertains to the burning area of the charge could be more meaningfully described in terms of an energy per unit volume concept. We define φ_s as the energy per unit volume in the solid phase and φ_G as the energy per unit volume in the gas phase. Thus, the first criterion could be reworded, for our discussion, to require that $d\varphi_G/dt$ increase sufficiently rapidly enough to effect DDT for cast materials. The energy per unit volume in the gas phase will be determined by 1) the energy available in the explosive (proportional to φ_s; this depends upon the chemical composition and compaction); 2) the rate at which this energy is released (proportional to $-d\varphi_s/dt$; this depends upon the linear burning rate); and 3) the rate at which energy is lost from the ignition region (this depends upon losses to the walls, hot gases flowing out of the burning region due to permeability, either natural as in porous charges or accidental, as in poorly prepared charges having air cavities or cracks). We will use both dp/dt and the energy per unit volume concept in subsequent discussions.

Subsection 2. (Charges with $B_o \ll B_o^{crit}$)

The introduction of porosity into a charge does not mean that the charge will be permeable. The pores present may or

may not be interconnected. If the pores are connected, permeability is very low and essentially negligible. The criteria for DDT in this subsection will be the same as discussed for Subsection 1. We would expect ℓ and t_D to be smaller than in Subsection 1 because the porosity will enhance slightly dp/dt and because the critical shock initiation pressure for detonation, P_i, would be slightly lower (8). If the explosive does not undergo DDT at 100% TMD or as a cast material, it probably will not undergo DDT at these densities either. This will be the case, most likely, for highly waxed RDX composites and Composition B (60/40/1 RDX/TNT/Wax).

In this case, the mechanisms involved in DDT should be the same as those elucidated for cast explosives (2) and the model calculations (1) should also be applicable.

Case B (Charge Densities where $B_o \leq B_o^{crit}$)

As the porosity increases, the fraction of pores which are interconnected increases rapidly. However, the permeability of the charge will be quite low. The formation of an ignition front in the pores of the explosive (convective burning) can now occur and will depend upon the permeability of the charge, the adiabatic flame temperature of the explosive, the ignition characteristics of the explosive and the ability of the confinement to allow a critical "driving" pressure to be set up. The onset of convective burning indicates that nonnegligible amounts of energy can now be transported by gas flow beyond the ignition region. However, for these densities (where $B_o < B_o^{crit}$) only very small quantities of gas can flow out of the ignition area, even over a time period of 100 μsec. Even so, $d\varphi_G/dt$ in the ignitor region should be larger for this case, Case B, than for Case A because a larger surface area for additional burning has been introduced by the interconnected pores. Thus, ℓ should decrease in the order: Case A (Subsection 1) - Case A (Subsection 2) - Case B. If so, the time to detonation in Case B should also decrease, relative to Subsections 1 and 2 of Case A, but only slightly (order of magnitude of tens of μsecs).

The mechanism for DDT in this case is very similar to those in cast explosives; chief difference is the proposed ignition by a convective flame front. The model calculations for DDT in cast explosives (1) probably become inapplicable for those charge densities where B_o approaches B_o^{crit}.

Case C (Densities Slightly Below Density where $B_o = B_o^{crit}$)

As more porosity is introduced into the charge, the gas flow can no longer be described as choked. Apparently enough pores are connected to permit flow which may be described as steady state (see Section IV.A.1). The increased permeability for this case leads to smaller values of dp/dt (i.e., $d\varphi_G/dt$) and φ_s. The time to produce a rapid acceleration in dp/dt is now longer than in earlier

cases since more explosive must be burned to compensate for the energy flow (in the gas phase) out of the burning area. Hence, t_D increases relative to Cases A and B.

The point (value of x) at which this rapid acceleration in dp/dt occurs may be farther from x = 0 (at a point farther away from the ignitor interface and in the pores of the granular bed). Within the density range of Case C dp/dt should decrease with increasing porosity because of increasing permeability and smaller values of φ_s, as mentioned above. The position of onset of detonation should henceforth ($B_o > B_o^{crit}$) increase with increasing porosity, in accord with the calculations of Macek (1) which show that ℓ will depend upon d^2p/dt^2. Our experimental results have indicated that a buildup to DDT begins only after the pressure in the ignition region begins to accelerate (i.e., is capable of sending out compressive waves).

The DDT mechanism for this case is similar to that of Case B. A convective flame front propagates ahead of the compressive waves which are necessary to form a precursor shock front. In modeling DDT for this case, it is necessary to include the convective front (and its consequences) because of its influence on dp/dt in the ignition region.

Case D (Very Permeable Charges; $B_o >> B_o^{crit}$)

For the very permeable charges ($B_o >> B_o^{crit}$), ℓ increases with increasing porosity in accord with the discussion in Case C. However, the energy losses from the burning region near the ignitor can be large enough to prevent the attainment of a sufficiently large $d\varphi_G/dt$ (or dp/dt) to effect transition. Hence, the burning area is now a large region beyond the ignition region. For explosives like RDX this will be the case for charges with very large porosities and it will occur at lower porosities for less energetic explosives, such as 91/9 RDX/Wax. Thus, in Case D, the chemical composition and the linear (conductive) burning rate (as reflected in φ_s and $d\varphi_s/dt$, respectively) become increasingly important. For the more energy deficient explosives, such as ammonium picrate, pressure increases at these densities can be quite slow and nonaccelerating. The absence of an accelerating dp/dt does not mean the absence of a high pressure. Pressure may increase linearly to several kilobars but in the absence of a rapidly rising dp/dt no compressive waves eminate from the burning region.

When an accelerating dp/dt does not occur, the pressure and pressure gradient generated in the burning region are sufficient to initiate movement of the porous bed after a period of one to two hundred microseconds. Consequently, collapse of the porous structure occurs immediately beyond the edge of the burning bed (nearest the ignitor). This collapse process increases the available energy per unit volume in the compacted material (i.e., φ_s) and here an accelerating $d\varphi_G/dt$ can be attained if it could be attained at higher densities

(i.e., Case C). If an accelerating $d\varphi_G/dt$ was not observed at higher densities, it may still result after pore collapse because the temperature of the collapsed bed will be higher than that of the initially higher density cases.

The DDT mechanism for Case D is identical to that proposed for Case C. However, the model for DDT in Case D can differ from that of Case C due to compaction of the porous bed.

The above proposals of the DDT mechanisms for porous explosives are based largely upon the experimental observations using 91/9 RDX/Wax where pressure and the propagation of reaction fronts within the tube could be monitored. The same mechanisms seem applicable to the more shock sensitive explosives (e.g., RDX, PETN) based upon the limited data of Griffiths and Groocock (5), Korotkov et al (28), and Andreev et al (16). It appears reasonable to assume that the mechanisms of all porous explosives should differ in degree only.

We have found no evidence in our strain gage measurements that the pressure at the head of the convective flame front builds up very rapidly and generates the rapidly increasing dp/dt needed for formation of the precursor shock wave (this was a mechanism suggested by Griffiths and Groocock (5)). We have observed that the only time the head of the convective front attains a higher pressure is when the PC wave (with <u>its</u> high pressure) overtakes the convective flame front.

SUMMARY AND CONCLUSIONS

Ionization and strain gage data for granular charges of RDX/Wax, 91/9, have led to the proposed mechanisms of DDT illustrated in Figure 44. From the formation of the PC wave to detonation, the schedule of events is closely analogous to that observed in cast explosives. Measurements showed that pressure does not build up rapidly at the head of the convection front and hence that the precursor shock does not originate there. As Figure 44 shows, it must originate behind both the convective and the PC fronts.

The effect of compaction on DDT is summarized in Figure 45. The convective wave velocity increases moderately with compaction up to 90% TMD after which it increases very rapidly. The predetonation column decreases with increasing compaction to a minimum at 90% TMD. In both cases, the change at 90% TMD is attributed to reaching the critical value of the permeability coefficients at that compaction. Similarly the marked change of slope in the curves for V_{PC}/V_L^o, t_D, and t_E at ca. 80% TMD are attributed to the same cause--in this case, occurrence of charge compaction prior to formation of the PC wave at compactions less than ca. 80% TMD. The marked similarity between the curves, t_E vs % TMD and t_D vs % TMD, points out the strong dependence between the time to formation of the post

SYMPTOMS OF CHOKED FLOW

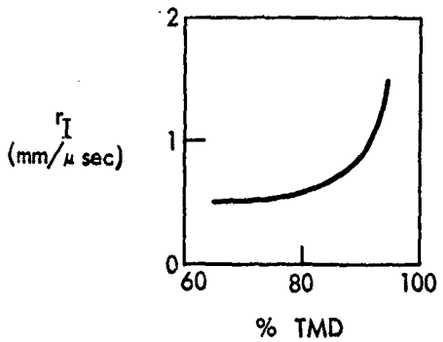

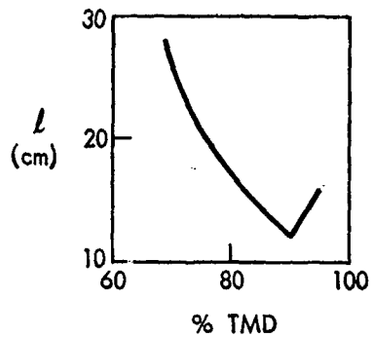

SYMPTOMS OF CHARGE COLLAPSE DURING BURNING

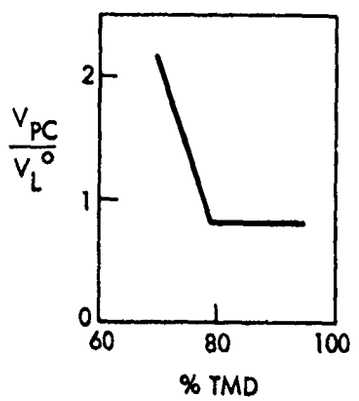

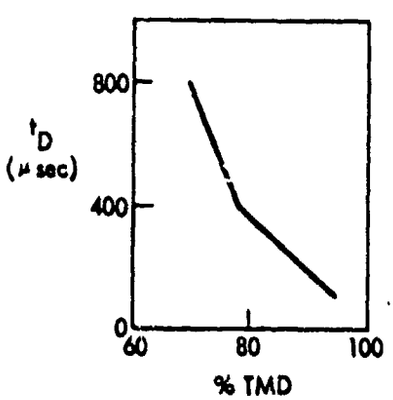

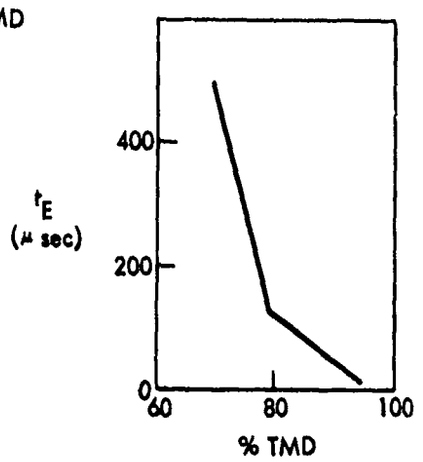

FIG. 45 EFFECT OF COMPACTION ON DDT PARAMETERS FOR 91/9 RDX/WAX.

convective wave and the time to detonation. In fact, the time to intersection of the post convective and convective wave is only 10 - 20 μsec less than t_D. Similarly the position of that intersection is only 10 - 20 mm less that ℓ. These values are of the order of magnitude of the run distances and delay times in shock-to-detonation transitions. Further analysis of the present records and additional measurements may lead to determination of these transitional parameters.

Ammonium picrate at 70% and 90% TMD exhibited a convective flame front but no transition to detonation. However, a 9 mm column of RDX interposed between the igniter and 70% TMD ammonium picrate was sufficient to effect such a transition. Quantitative study of such gas loading experiments is planned in future work.

A short series of RDX/Wax compositions at 3 - 9% wax was run at 70% TMD. The parameter ℓ increased and the parameter t_D increased with increasing wax content.

ACKNOWLEDGEMENTS

The authors wish to thank Mr. A. Robert Clairmont for reading experimental records on the telereader. Mr. John Erkman and Dr. David Edwards for discussions of experimental arrangements and Mr. Rudolph Garnett for assembling and instrumenting the explosive charges. In addition, the authors thank Dr. Paul Flynn for discussions on use of strain gages and the interpretation of his experimental results.

REFERENCES

1) A. Maček, J. Chem. Physics, 31, 162 (1959).

2) R. W. Gipson and A. Maček, Eighth Symposium (International) on Combustion. p. 847-854. Williams and Wilkins: Baltimore, 1962.

3) D. Price and . . F. Wehner, Comb. Flame, 9, 73 (1965).

4) K. K. Andreev. Explosivestoffe, 10, 203 (1962).

5) N. Griffiths and J. M. Groocock, J. Chem. Soc., 1960, 4154.

6) K. K. Andreev, Zh. Prikl. Khim., 17, 533 (1944).

7) A. F. Belyaev, A. I. Korotkov, and A. A. Sulimov, Combustion, Explosion, and Shock Waves, 2 (3), 28 (1966).

8) See for example D. Price, Eleventh Symposium (International) on Combustion. p. 693. Combustion Institute, Pittsburgh, 1967.

9) J. W. Dally and W. F. Riley. "Experimental Stress Analysis", p. 446 ff. McGraw-Hill Book Co., New York, 1965.

10) A. F. Belyaev, A. I. Korotkov, A. A. Sulimov. M. K. Sukoyan and A. V. Obmenin, Combustion, Explosion and Shock Waves, 5 (1), 8 (1969).

11) P. D. Flynn, Experimental Mechanics, 10, 297 (1970).

12) J. C. Jaeger. "Elasticity, Fracture, and Flow". p. 53. Methuen and Co., Ltd., London, 1969.

13) P. D. Flynn, private communication.

14) N. L. Coleburn and T. P. Liddiard, private communication.

15) R. W. Gipson and A. J. Maček, NAVORD Report 6867, 17 March 1960.

16) K. K. Andreev and S. V. Chuiko, Russ. J. Phys. Chem., 37, 695 (1963).

17) D. W. Culbertson, M. C. Shamblen. and J. S. O'Brasky. "Investigation of 5" Gun In-Bore Ammunition Malfunctions". NWL TR-2624 Naval Weapons Laboratory. Dahlgren, Dec. 1971.

18) B. Lewis and G. von Elbe, "Combustion, Flames, and Explosions of Gases", pp. 545-554. Academic Press Inc., New York, 1961.

19) R. Hill. "The Mathematical Theory of Plasticity". pp. 106-118. Oxford University Press, London, 1956.

20) L. D. Hampton "Detonation Velocities of Several New Explosives Measured by the Small Scale Technique", NAVORD Report 2450, 19 May 1952.

21) T. Godai, AIAA J., 8, 1322 (1970).

22) C. E. Payne, "Flame Propagation in Propellant Cracks", TR-69-66, Air Force Rocket Propulsion Laboratory, Edwards, Calif. April 1969.

23) N. N. Bakhman, Russ. J. Phys. Chem., 35, 414 (1961).

24) B. O. Reese, J. H. Blackburn, L. B. Seely, and M. W. Evans, Comb. Flame, 11, 262 (1967).

25) I. E. Lindstrom, J. Appld. Phys., 41, 337 (1970).

26) S. Timoshenko, "Strength of Materials. Part II Advanced Theory and Problems", p. 205-210, 386-392. Van Nostrand Co., Princeton N. J., 1956.

27) K. K. Andreev and V. V. Gorbunov Russ. J. Phys. Chem., 37, 1061 (1963).

28) A. I. Korotkov, A. A. Sulimov, A. V. Obmenin, V. F. Dubovitskii, and A. I. Kurkin, Fiz. Gor. Vry, 5 (3), 315 (1969).

29) K. K. Andreev, Vzryvnoye Delo., No. 52, 9 (1963), pp. 130-140, Through AD 634307.

30) P. C. Carman, "Flow of Gases Through Porous Media", Academic Press, Inc., New York. 1956.

31) D. Price, J. F. Wehner, and G. E. Roberson, "Transition from Slow Burning to Detonation: Role of Confinement, Pressure Loading and Shock Sensitivity", NOLTR 64-138, 14 Sept. 1964.

GLOSSARY

x	distance along axis of tube, relative to ignitor/explosive interface
t	time
p	pressure
E	voltage output from strain gage circuit
V	voltage of strain gage power supply
r	velocity of convective flame front
ℓ	predetonation column length
t_D	time interval between ignition of explosive column at $x = 0$ and onset of detonation
Δt_D	time interval between discharge of ionization probe at 41 mm and onset of detonation
t_E	time interval between passage of convective front and passage of the PC front
t_I	relative time of electromagnetic disturbance on strain gage records which is associated with intersection of convective and PC fronts
t_{PC}	time interval between the discharge of the IP closest to the ignitor and passage of the PC wave
P_i	critical initiation gap pressure for shock initiation
φ_G	energy per unit volume in gas phase
φ_s	energy per unit volume in solid phase
V_L	longitudinal sound velocity
V_L^o	sound velocity in porous bed at initial conditions of our charges
V_{PC}	velocity of the post convective wave
r_I	velocity of convective flame front at time of intersection of convective and PC waves
x_F	position of initial reaction front (convective front)

x_{DF} position of detonation front

s_d standard deviation

σ stress

ϵ strain

ρ_o initial density of charge

ρ_v voidless density

X run-up length to detonation from shock initiation

ABBREVIATIONS

DDT deflagration-detonation transition

IP ionization probe

SG strain gage

PC postconvective

APPENDIX A

INTERNAL PRESSURE-STRAIN CALIBRATION OF DDT TUBES

The calibration of the DDT tubes used in the earlier NOL work (1-3) was based upon static pressurization of the tubes. We shall show that calculations based on theoretical stress-strain equations for cylindrical pressure vessels approximate fairly well the experimental calibration curve found earlier (31). The calculations are extended to our present DDT tubes to establish the range over which stress and strain are linearly related and to calculate also the internal pressure-strain relationship when part of the tube wall is in the plastic region.

A. The expansion of a cylindrical tube has been treated by Timoshenko (26), Hill (19) and Jaeger (12), in addition to others. Figure A-1 shows the schematic diagram of a long hollow thick-walled cylinder subjected to an internal pressure p. The inner and outer radii of the tube are denoted as a and b, respectively. Expressions relating the internal pressure to the stress, σ, are

$$\sigma_r = -p\left(\frac{b^2}{r^2} - 1\right)/(w^2-1) \qquad \text{A-1}$$

$$\sigma_t = p\left(\frac{b^2}{r^2} + 1\right)/(w^2-1) \qquad \text{A-2}$$

$$\sigma_x = E_Y \epsilon_x + [2\upsilon p/(w^2-1)] \qquad \text{A-3}$$

where σ = stress
ϵ = strain
υ = Poissons ratio
w = wall ratio, b/a
E_Y = Young's modulus of elasticity
subscript r = radial direction
t = tangential direction
x = axial direction

The radial displacement, u_r, is given by Hill as

$$u_r = -\upsilon\epsilon_x r + \frac{(1+\upsilon)p}{E_Y r(w^2-1)}[(1-2\upsilon)r^2+b^2] \qquad \text{A-4}$$

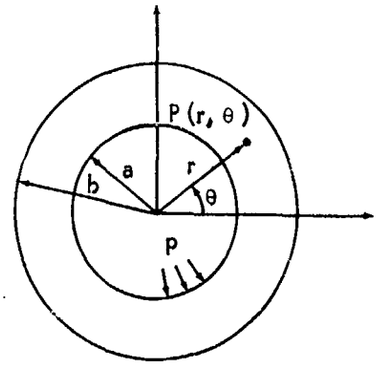

FIG. A1 CROSS SECTION OF PRESSURIZED CYLINDRICAL TUBE

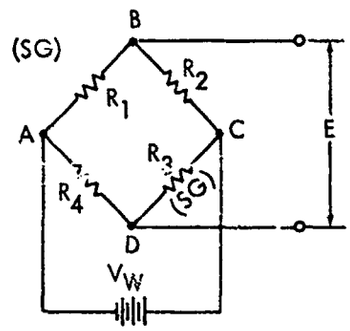

FIG. A2 THE WHEATSTONE BRIDGE CIRCUIT SCHEMATIC.

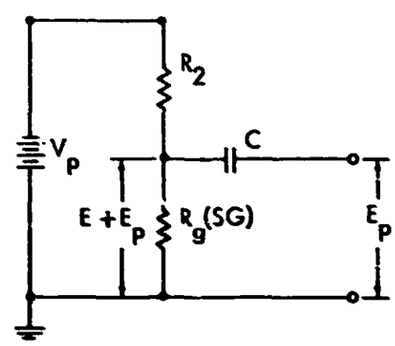

FIG. A3 THE POTENTIOMETRIC CIRCUIT SCHEMATIC.

The radial and tangential strains are defined as

$$\epsilon_r = du_r/dr \qquad \text{A-5}$$

$$\epsilon_t = u_r/r \qquad \text{A-6}$$

Hence,

$$\epsilon_t = -\nu\epsilon_x + \frac{(1+\nu)p}{E_Y(w^2-1)}\left[(1-2\nu) + b^2/r^2\right] \qquad \text{A-7}$$

However, the end conditions determine the values of ϵ_x and σ_x. Hill discusses (19) the three end conditions: a) closed end; b) open end (plane stress); and c) plane strain.

In his solution of the cylindrical pressure vessel problem Jaeger considers that the situation is one of plane strain, i.e.,

$$\epsilon_x = 0 \qquad \sigma_x = \nu(\sigma_t+\sigma_r) \qquad \text{A-8}$$

or from equations (A-1) and (A-2),

$$\sigma_x = \frac{2\nu p}{(w^2-1)} \qquad \text{(Plane strain)} \qquad \text{A-8'}$$

From equation (A-7)

$$\epsilon_t = \frac{(1+\nu)p}{E_Y(w^2-1)}\left[(1-2\nu)+ b^2/r^2\right] \qquad \text{A-9}$$

For our strain gages, the tangential strain would be, for plane strain,

$$(\epsilon_t)_b = \frac{2p}{E_Y(w^2-1)}(1-\nu^2) \qquad \text{A-10}$$

or, from equation A-2,

$$(\epsilon_t)_b = \frac{(\sigma_t)_b}{E_Y}(1-\nu^2)$$

(Plane strain)

Timoshenko (26), on the other hand, considered the pressurization of a thick-walled cylinder to be representative of plane stress, $\sigma_x = 0$. Hence, when we combine equations (A-3) and (A-7) and evaluate the tangential strain at $r = b$, we find

$$(\epsilon_t)_b = \frac{2p}{E_Y(w^2-1)} \qquad \text{A-11}$$

or, from equation A-2,

$$(\epsilon_t)_b = \frac{(\sigma_t)_b}{E_Y}$$

Plane Stress

As pointed out by Hill (19), equation A-11 represents plane stress or the situation where floating pistons allow the tube to expand freely. If the tube is closed by plugs firmly attached to the tube (condition a), the axial strain and stress are

$$\epsilon_x = \frac{(1-2\nu)p}{E_Y(w^2-1)} \qquad \text{A-12}$$

$$\sigma_x = p/(w^2-1) = 1/2(\sigma_r+\sigma_t) \qquad \text{A-13}$$

Closed End

Combining equations A-7 and A-12 yields

$$\epsilon_t = \frac{p(1-2\nu)}{E_Y(w^2-1)} + \frac{(1+\nu)p}{E_Y(w^2-1)}\frac{b^2}{r^2} \qquad \text{A-14}$$

For our strain gage location the strain relationship A-14 gives equations A-15,

$$(\epsilon_t)_b = \frac{2p}{E_Y(w^2-1)}\left(1-\frac{\nu}{2}\right) \qquad \text{A-15}$$

or

$$(\epsilon_t)_b = \frac{(\sigma_t)_b}{E_Y}\left(1-\frac{\nu}{2}\right)$$

Closed End

From the above discussion it is evident that the relationship between the internal pressure and strain at the outer wall depends upon the end conditions of the tube. However, the radial and tangential stress are independent of the end conditions, i.e., equations A-1 and A-2 are constant at a given r. Therefore, for our strain gage locations,

$$(\sigma_r)_b = 0 \qquad \text{A-16}$$

$$(\sigma_t)_b = \frac{2p}{w^2-1} \qquad \text{A-17}$$

while

$$(\epsilon_t)_b = -\upsilon\epsilon_x + \frac{2p}{E_Y(w^2-1)}(1-\upsilon^2) \qquad \text{A-18}$$

In summary, the ratio of tangential strain (at r = b) to the internal pressure for the three end boundary conditions can be reduced to a single relationship equation A-19 (derived from equations A-10, A-11 and A-15)

$$\frac{(\epsilon_t)_b}{p} = Z \cdot \Gamma \equiv \frac{\epsilon}{p} \qquad \text{A-19}$$

where

$$\epsilon = (\epsilon_t)_b$$

$$Z = 2/E_Y(w^2-1)$$

$$\Gamma = 1-\upsilon^2 \quad \text{(for plane strain)}$$

$$= 1 \quad \text{(for plane stress)}$$

$$= 1-\upsilon/2 \quad \text{(for closed end)}$$

or

$$(\epsilon_t)_b = (\sigma_t)_b\,\Gamma/E_Y \equiv \epsilon \qquad \text{A-19a}$$

B. Wheatstone Circuits

Two types of circuits were used with out strain gages. The two strain gages located in the ignition region of the DDT tube (at 20 mm, consistently) constituted two arms of a Wheatstone bridge circuit shown schematically in Figure A-2 (this circuit was used in the earlier calibration and DDT work (3,31)). Thus, R_1 and R_3 in Figure A-2 represents our SGs. R_2 and R_4 were a combination of fixed and variable resistors designed to balance the bridge and their sum equals 2000 Ω. The voltage output of the Wheatstone bridge, E_w, caused by a strain within the DDT tube is related to change in resistance of the strain gage, R_g, by the equation

$$E_w = V_w \frac{R_g R_2}{(R_g+R_2)^2} \left(\frac{2\Delta R_g}{R_g} \right) \qquad \text{A-20}$$

Since $R_1 = R_2 = R_3 = R_4 = R_g$, we obtain the relationship,

$$E_w = \frac{V_w}{2} \frac{\Delta R_g}{R_g} \qquad \text{A-21}$$

The strain gages used in this work have been calibrated by the manufacturer in terms of resistance change as shown in the equation

$$\epsilon = \frac{\Delta R_g}{R_g} \frac{1}{S_g} \qquad \text{A-22}$$

where S_g is gage factor, units of in. ohm in.$^{-1}$ ohm^{-1}. Combining equations A-19, A-21 and A-22 yields

$$\frac{E_w}{p} = \frac{S_g V_w}{E_Y(w^2-1)} \Gamma \equiv \text{S.F.} \qquad \text{A-23}$$

Using equation A-23, we can evaluate which end boundary condition yields a SG sensitivity factor, S.F., which is consistent with the experimental value (3) of 9.0 mv/kbar. For a = 0.25 in., b = 0.625 in., V_w = 30.0 volts, S_g = 3.3, $E_Y = 29.5 \times 10^6$ psi, we find that

$$\text{S.F.} = 9.26\ \Gamma$$

The value of the gage factor, S_g, for the earlier work is uncertain. Some remaining SGs from that work had a gage factor of 3.5. Most of our SGs have had a similar value but certain lots which have been obtained, but not used in this work, have factors of 3.14 or 3.27. The sensitivity factors for the three values of Γ and the three values of S_g are shown in Table A-1. It appears that conditions of either plane stress or plain strain yield relatively good agreement with the experimental sensitivity factor of 9.0 mv/kbar.

TABLE A-1

CALCULATED STRAIN GAGE SENSITIVITY FACTOR
FOR DDT TUBE USED IN EARLIER NOL WORK
(Reference 3)

S_g	3.1	3.3	3.5
$\Gamma = 1$	8.70	9.26	9.82
$\Gamma = 1-\nu^2$	7.97	8.48	9.00
$\Gamma = 1-\nu/2$	7.44	7.92	8.40

We now can use equation A-23 to calculate a sensitivity factor for our present tube where a = 0.32 in., b = 1.00 in., V_W= 29.1 volts, $E_Y = 29.5 \times 10^6$ psi and $S_g = 3.5$. The sensitivity factor is 5.7 and 5.2 mv/kbar for plane stress and plane strain, respectively. Thus, in the elastic region we should expect a pressure increase of 1 kilobar to be indicated by an output of about 5.7 mv using the Wheatstone circuit (see discussion in section D, below).

The experimental pressure-strain curve showed that the linear relationship between the voltage output and internal pressure ended at about 2.2 kbar. Beyond 2.2 kbars, the apparent sensitivity factor increased with increasing pressure. We attribute this behavior to the beginning of plastic yielding at the inner wall (r = a) above 2.2 kbar. Using the procedure outlined by Hill (19), we will show that with the assumption of plastic yielding, calculated E_W-p curves agree well with the experimental data.

Using Tresea's criterion for yielding, Hill (19) shows that yielding begins at the internal surface first at an internal pressure calculated from the equation

$$p_{YP} = \frac{Y}{2}\left(\frac{w^2-1}{w^2}\right) \qquad \text{A-24}$$

where Y = yield point stress.

Equation A-24 holds for <u>all</u> end boundary conditions. For p_{YP} equal

to 2.20 kbars, Y is 5.24 kbar or 76,000 psi. Assuming the same yield point stress for the present DDT tubes, we calculate p_{YP} to be 2.35 kbars.

To calculate the stress-strain relationship in the partially plastic region of the tube wall, we modify equations A-1 to A-3 for the plastic/elastic interface located at $r = c$ $(a < c < b)$. Thus, the stresses in the plastic region $(a \leq r \leq c)$ are

$$\sigma_r^P = -\frac{Y}{2}\frac{c^2}{b^2}\left(\frac{b^2}{r^2} - 1\right) \qquad \text{A-25}$$

$$\sigma_t^P = \frac{Y}{2}\frac{c^2}{b^2}\left(\frac{b^2}{r^2} + 1\right) \qquad \text{A-26}$$

$$\sigma_x^P = E_Y \epsilon_x + \nu Y \frac{c^2}{b^2} \qquad \text{A-27}$$

and

$$\epsilon_t^P = -\nu \epsilon_x + \frac{(1+\nu)Yc^2}{2E_Y b^2}\left[(1-2\nu) + \frac{b^2}{r^2}\right] \qquad \text{A-28}$$

The internal pressure, p', needed to produce the plastic/elastic interface at $r = c$, is given by equation A-29

$$p' = Y \ln(c/a) + .5Y(1 - c^2/b^2) \qquad \text{A-29}$$

At the interface $(r = c)$ there is a radial pressure, p_x, acting between the two regions. For the elastic region, p_x is related to the yield point stress by equation A-24 where w is replaced by the ratio, b/c, so that

$$p_x = \frac{Y}{2}\left(\frac{b^2 - c^2}{b^2}\right) \qquad \text{A-30}$$

However, the tangential stress is related to the radial pressure, p_x, by equation A-2, where again w is replaced by b/c.

$$\sigma_t^E = p_x \left(\frac{b^2}{r^2} + 1\right) / \left(\frac{b^2}{c^2} - 1\right) \qquad \text{A-31}$$

or

$$(\sigma_t)_b^E = \frac{2p_x c^2}{b^2 - c^2} \qquad \text{A-32}$$

Eliminating p_x from A-30 and A-32 yields

$$(\sigma_t)_b = Y \frac{c^2}{b^2} \qquad \text{A-33}$$

Combining equations A-19a and A-33 yields the relationship between the tangential strain on the outer surface, ϵ, and c,

$$\epsilon \equiv \frac{\Gamma}{E_Y} Y \frac{c^2}{b^2} = (\epsilon_t)_b \qquad \text{A-34}$$

There, the internal pressure, p', producing a plastic/elastic interface at r = c is related to the strain ϵ by equation A-35, which is found by eliminating c^2 from equations A-29 and A-34.

$$p' = \frac{Y}{2} \ln \left[\frac{\epsilon E_Y w^2}{Y\Gamma}\right] + \frac{Y}{2} \left[1 - \frac{\epsilon E_Y}{Y\Gamma}\right] \qquad \text{A-35}$$

Expressed in terms of experimental parameters relating ϵ and the Wheatstone bridge characteristics (e.g., equations A-21 and A-22), equation A-35 becomes

$$p' = \frac{Y}{2} \left[\ln\left(\frac{2E_W E_Y w^2}{V_W S_g Y\Gamma}\right) - \frac{2E_W E_Y}{V_W S_g Y\Gamma} + 1\right] \qquad \text{A-36}$$

Numerically, equation A-36 reduces to A-37 when we use $E_Y = 29.5 \times 10^6$ psi, $w^2 = 6.25$, $V_W = 30$ volts, Y = 76000 psi,

$$p' = 2.62 \left[\ln \frac{0.1618 E_W}{\Gamma S_g} - \frac{0.02588 E_W}{\Gamma S_g} + 1\right] \qquad \text{A-37}$$

The pressure, p', is tabulated in Table A-2 for various values of S_g and Γ. The data in Table A-2 show that plane stress analysis of the thick walled cylinder problem (i.e., $\Gamma = 1$) yields the best agreement with the experimental data. Moreover, very good agreement is obtained with plane stress analysis and a gage factor of 3.5.

TABLE A-2

COMPARISON OF EXPERIMENTAL AND CALCULATED STRAIN GAGE VOLTAGE OUTPUT FOR DDT TUBE USED IN EARLIER NOL WORK (Reference 31)

E_W (millivolt)	p^a (kbar)	$\frac{S_g \mid \Gamma}{p'}$ $\frac{3.5 \mid 1}{p'}$	$\frac{3.5 \mid 1-\nu^2}{p'^b}$	$\frac{3.3 \mid 1-\nu^2}{p'}$
0	0			
5	0.543			
10	1.105			
15	1.663			
20	2.220			
25	2.585	2.515	2.701	----
30	2.876	2.895	3.072	3.188
35	3.128	3.202	3.370	----
40	3.355	3.455	3.614	3.718
45	3.572	3.668	3.817	----
50	3.749	3.846	3.988	4.077
55	3.892	4.001	4.131	----
58	3.947	4.079	4.208	----

a) Reference 31.
b) This column of internal pressure also represents the calculated pressure for plane stress ($\Gamma = 1$) with $S_g = 3.2$.

The agreement between the calculated and experimental pressures in Table A-2 confirms the assumption that the nonlinearity of pressure - E_w observed in the static experiments is indeed due to plastic yielding of the inner wall which began at 2.2 kbar*. Consequently, equations A-23 and A-36 can be used to determine an approximate pressure-strain calibration for the present DDT tubes as discussed in section D of this appendix.

C. Potentiometric Circuits

Each of the two downstream SGs were connected to a potentiometric circuit as shown in figure A-3. The capacitor, 0.1 μf, was used to block out the dc component of the output, E, in order that small strain voltages, E_P, could be detected. R_2 is a ballast resistor, 6000 Ω, and R_g is the strain gage. The equation relating voltage output, E_P, caused by a strain within the DDT tube is

$$E_P = \frac{R_2 R_g}{(R_2+R_g)^2} \frac{\Delta R_g}{R_g} V_P \qquad \text{A-38}$$

or

$$E_P = \frac{r'}{(1+r')^2} \frac{\Delta R_g}{R_g} V_P \qquad \text{A-38a}$$

where $r' = R_2/R_g$

Since $r' = 3.0$, equation A-38 becomes for our circuits

$$E_P = \frac{3V_P}{16} \frac{\Delta R_g}{R_g} \qquad \text{A-39}$$

or

$$E_P = \frac{3V_P}{16} S_g \epsilon \qquad \text{A-40}$$

- - - - - - - - - - - - - - - - - - -

* Exact agreement is not expected, especially at the higher pressures, since equation A-29 and A-35 require the use of the inner radius under plastic conditions. We have approximated this with the initial inner radius (i.e., we have assumed the tube wall to be incompressible).

For the Wheatstone bridge circuit, the equivalent relationship is

$$E_W = \frac{V_W}{2} S_g \epsilon \qquad \text{A-40a}$$

For the same output/strain ratio, we must have the relationship

$$V_p = \frac{8}{3} V_W \qquad \text{A-41}$$

For our experimental setup, $V_W = 29.10$ volts and $V_p = 77.60$ volts. Thus, equal outputs on either type of strain gage circuit equals the same amount of strain for a constant gage factor, S_g. Consequently, equations A-23 and A-36 apply equally well to the potentiometric circuit calibration as to the Wheatstone bridge circuit calibration*.

D. Calculated Voltage -- Pressure Curve for Present DDT Tube

The relationships between strain and internal pressure for thickwalled tubes in both the elastic and plastic regions have been discussed in earlier sections of this appendix. In terms of experimental parameters, the strain and pressure are correlated by equation A-23 for the elastic region and equation A-36 for the plastic region. In section B of this appendix, we calculated that the walls should start yielding at 2.35 kbars for the present DDT tubes. Using a supply voltage, V_W, equal to 29.1 volts, $S_g = 3.5$, $E_Y = 29.5 \times 10^6$ psi, we find that up to 2.35 kbars, the sensitivity factor, S.F. (in mv output per kilobar), is calculated to be

$$5.7 \times \Gamma \quad \text{mv/kbar}$$

We shall assume that $\Gamma = 1$ (plane stress) for the elastic and plastic regions based upon the analysis of section B. Thus, S.F. is 5.7 mv/kbar in the elastic region (i.e., internal pressure less than 2.35 kbar). Therefore, it is estimated that there is a linear relationship between pressure and SG output up to about 13 mv for the present tubes.

In the plastic region the relationship between internal pressure (kbar) and voltage output (mv) is given by equation A-42 which follows from equation A-36 when $E_Y = 29.5 \times 10^6$ psi, $Y = 76{,}000$ psi or 5.24 kbar, $w^2 = 9.766$, $V_W = 29.1$ volts, and $\Gamma = 1$.

$$p' = 2.62\,[\ln(0.0744E_W) + 1 - 0.00762E_W] \qquad \text{A-42}$$

- - - - - - - - - - - - - - - - - -

* It is assumed for this discussion that the calibration is independent of position along the tube wall.

The calculated calibration data for the present DDT tube are listed in Table A-3 and shown in Figure A-4 on a semilog scale. It is interesting that the data from just below the elastic limit (i.e., 2.0 kbar) to about 4.4 kbar show a linear dependence on a semilogarithm plot. (The earlier experimental data from the static calibration in the cast explosive work (31), are also shown in Figure A-4). Consequently, the following relationships correlate internal pressure with experimental SG output (based upon a yield point at 2.2 kbar (31))

$$p = \frac{E_W}{5.7} \qquad 0 < p \leq 2.0 \text{ kbar}$$

$$p = 2.0 + \frac{1}{.195} \log \frac{E_W}{11.4} \qquad 2.0 < p < 4.4 \text{ kbar}$$

TABLE A-3

CALCULATED CALIBRATION DATA FOR INTERNAL PRESSURE LOADING OF PRESENT DDT TUBE

Gage Output (E_W), mv	Pressure (kbar)*
0	0.0
2.8_5	0.50
5.7	1.00
8.5_5	1.50
11.4	2.00
13.1	2.30
15.0	2.61
18.0	3.03
20.0	3.26
22.0	3.47
25.0	3.75
28.0	3.98
30.0	4.12
35.0	4.43
40.0	4.68

*Calculated from equation A-42, i.e.,

$$p' = 2.62\,[\ln(.0744E_W) + 1 - .00762\,E_W]$$

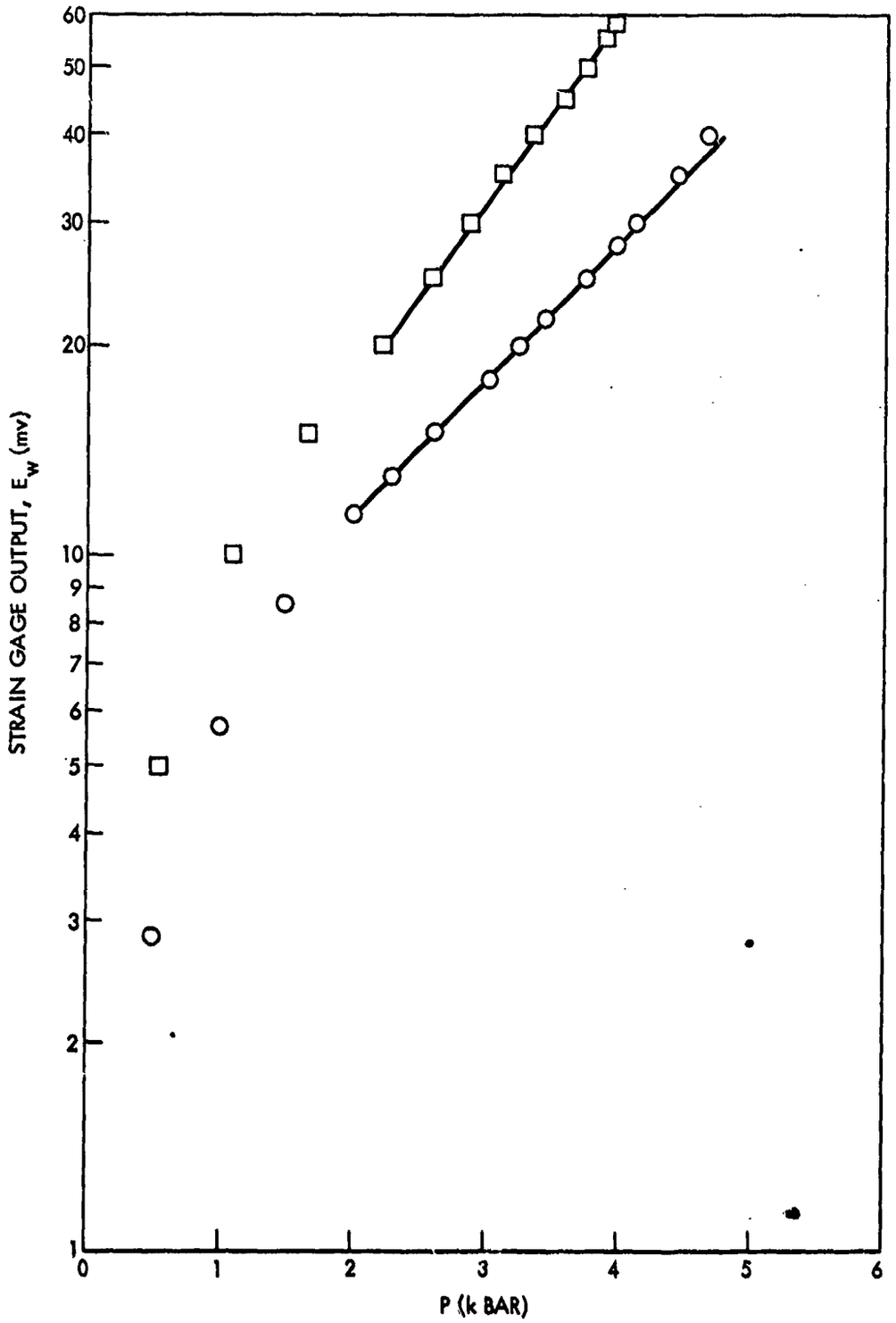

FIG. A4 STRAIN GAGE CALIBRATIONS OF DDT TUBES [○ CALCULATED DATA FOR PRESENT DDT TUBE □ EXPERIMENTAL STATIC CALIBRATION DATA FOR PREVIOUS DDT TUBE (REF. 31).]

APPENDIX B

COMPILATION OF SUPPLEMENTARY EXPERIMENTAL DATA

A. Table B-1 contains the experimental distance-time data for the ionization probes and strain gages for 91/9 RDX/Wax. The corresponding data for other miscellaneous runs are listed in Table B-2.

The particle analysis of the Class A RDX (X597) is listed in Table B-3 and the accumulative weight % vs. particle size is shown in Figure B-1.

B. The recovered tube fragments provide additional information which complements the IP and SG data. Table B-4 contains the measurement of the position and extent of permanent plastic deformation for the recovered ignitor end of the DDT tube.

C. The strain gage records for the 91/9 RDX/Wax mixture provide a pressure-time picture of the DDT buildup with the porous charges. It is sometimes more enlightening to consider the pressure profile in the tube at various times. Added incentive to do so was provided by the observations made earlier in Section IIIC1 (see Figures 28, and 32) that one or both of the SGs at locations farthest from the ignitor showed outputs which at times exceeded the output from the SG nearest the ignitor.

The voltage-distance data for Shot 306 (85.5% TMD) and Shot 315 (78.8% TMD) are shown in Figures B-2 and B-3, respectively. These pressure profiles show that the pressure gradient apparently is directed toward the far end of the tube, in accord with the concept of pressure buildup to DDT originating in the ignition region. However, when we consider charge densities below 78% TMD, we note a change in pattern at the later times. Figures B-4, B-5, and B-6 show the pressure profiles at various times for Shots 312 (76.5% TMD), Shot 307 (74.3% TMD) and Shot 225 (69.8% TMD), respectively. Figures B-4 and B-5 show that up to 40 to 60 μsec after the formation of the PC wave and about the time that the PC wave reaches the third SG (i.e., SG farthest from the ignitor), the pressure gradient is directed toward the far end of the tube (what we call a negative gradient). However, at longer times (but pressures < 4.5 kbar), we note the presence of a maximum in the E-x plane which is more prominent for the lower charge density (Figure B-5). In Figure B-6, a maximum in the E-x plane may be present at times just slightly after that at which the PC wave is first seen (i.e., at about 510 μsec).

The porous bed near the ignitor has been burning the longest and therefore its burning surface area has been depleted relative to the area available in the regions of charge which have burned a lesser time. The greater the burning area, the greater the gas and pressure

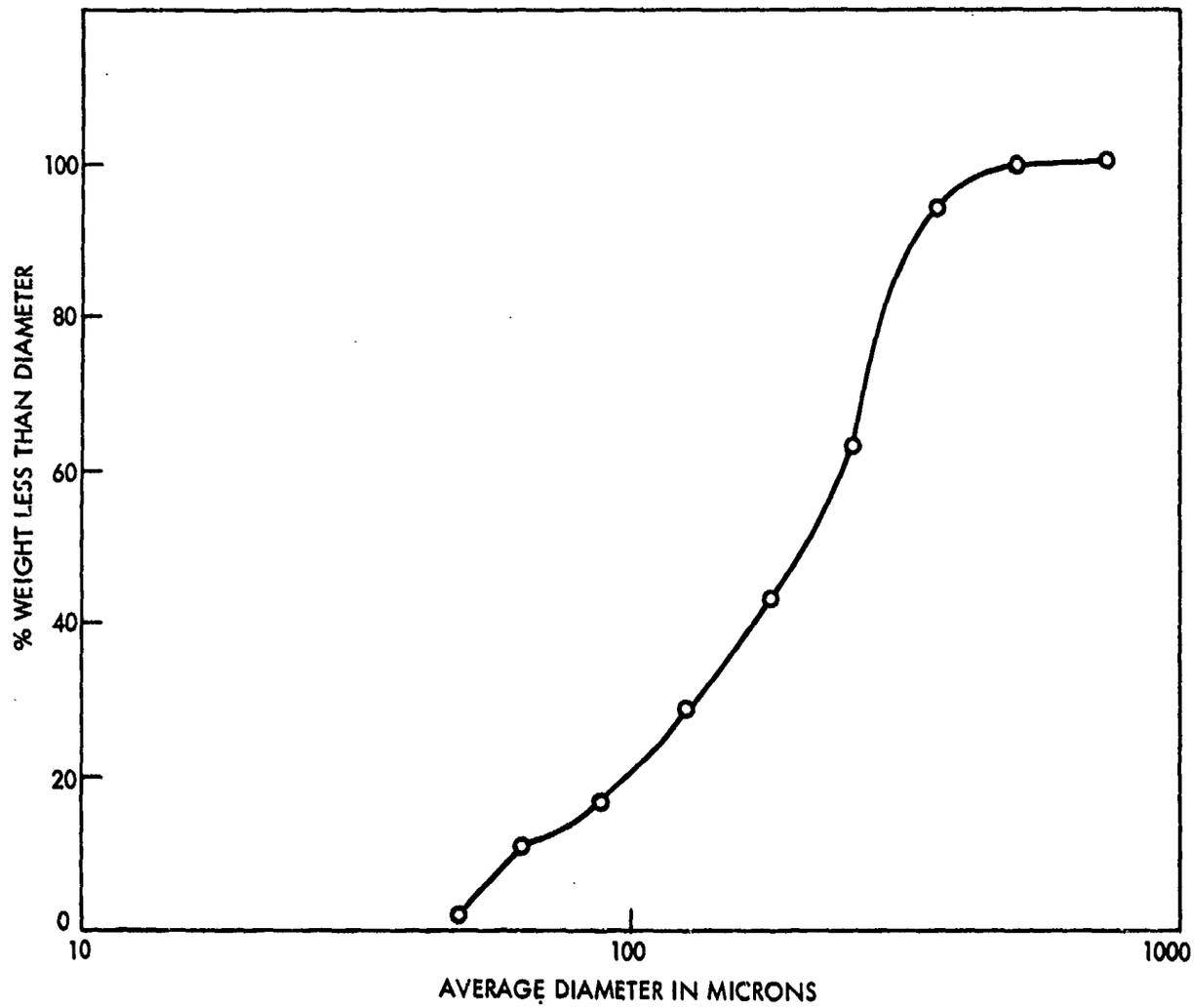

FIG. B1 PARTICLE SIZE DISTRIBUTION OF RDX (X597)

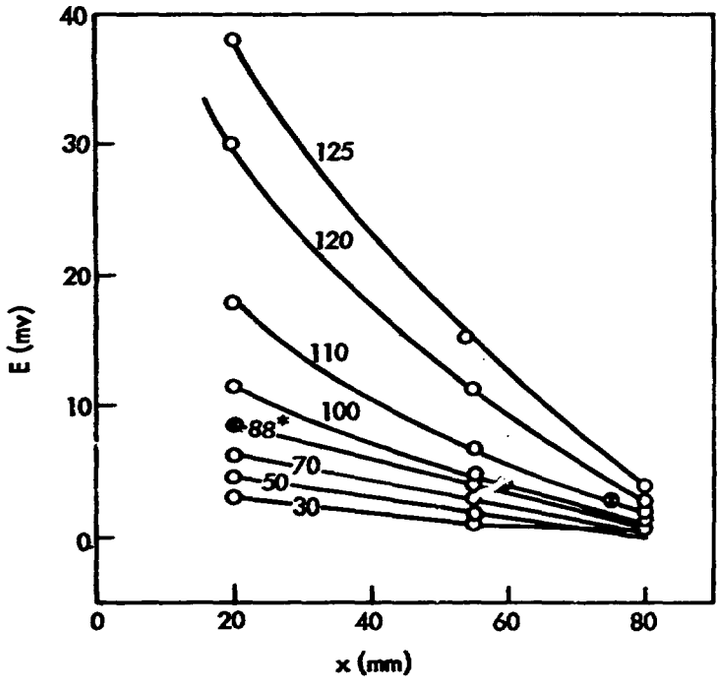

FIG. B2 STRAIN GAGE VOLTAGE - DISTANCE DATA FOR 85.5% TMD 91/9 RDX/WAX (SHOT 306).

[*TIME AT WHICH PC WAVE IS FIRST OBSERVED.
⊗ POSITION OF PC WAVE (AFTER 116 μsec, PC WAVE IS BEYOND 80 mm).]

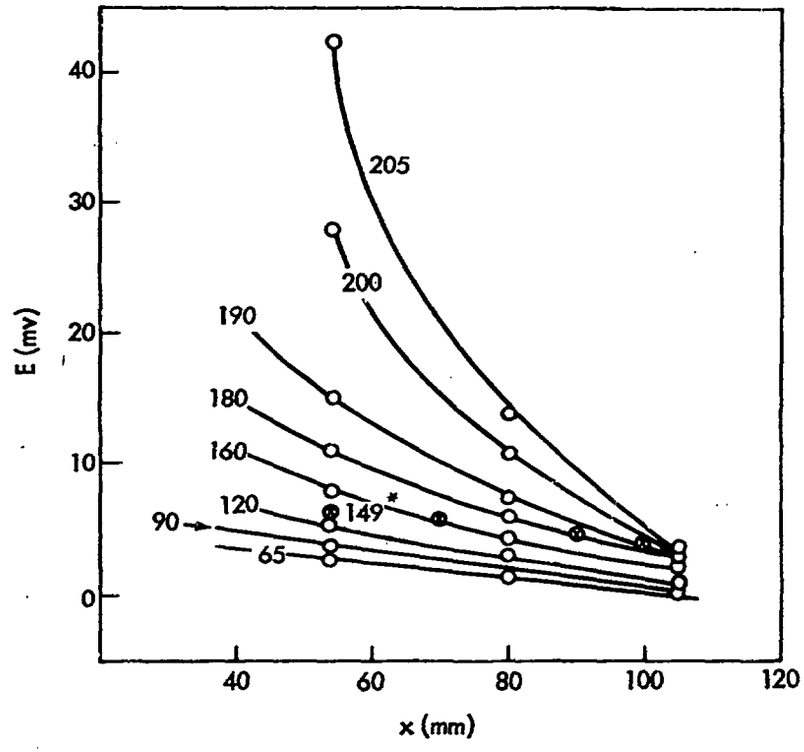

FIG. B3 STRAIN GAGE VOLTAGE - DISTANCE DATA FOR 78.8% TMD 91/9 RDX/WAX (SHOT 315).

[*TIME AT WHICH PC WAVE IS FIRST OBSERVED.
⊗ POSITION OF PC WAVE. (AFTER 197 μsec, PC WAVE IS BEYOND 105 mm).]

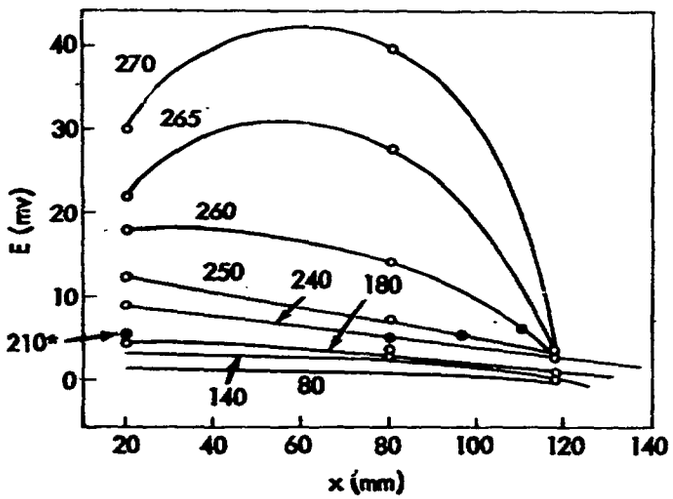

FIG. B4 STRAIN GAGE VOLTAGE - DISTANCE DATA FOR 76.5% TMD 91/9 RDX/WAX (SHOT 312) [*TIME AT WHICH PC WAVE IS FIRST OBSERVED. ● POSITION OF PC WAVE (AFTER 260 μsec, PC WAVE IS BEYOND 117 mm).]

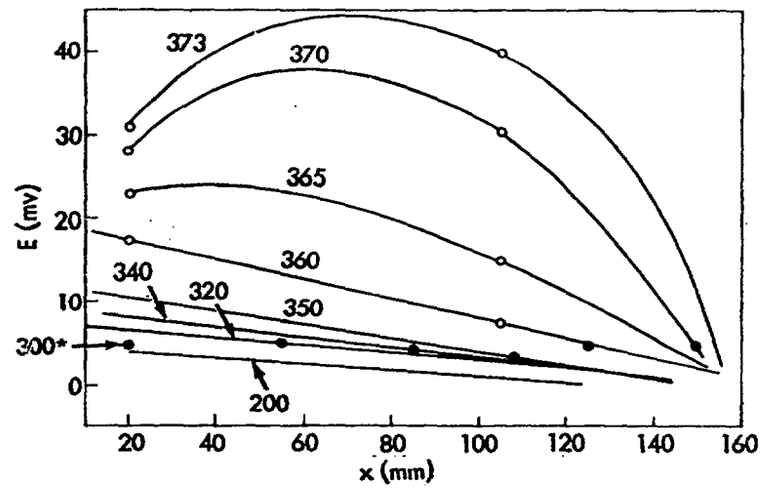

FIG. B5 STRAIN GAGE VOLTAGE - DISTANCE DATA FOR 74.3% TMD 91/9 RDX/WAX (SHOT 307) [*TIME AT WHICH PC WAVE IS FIRST OBSERVED ● POSITION OF PC WAVE (AFTER 373 μsec, PC WAVE IS BEYOND 155 mm).]

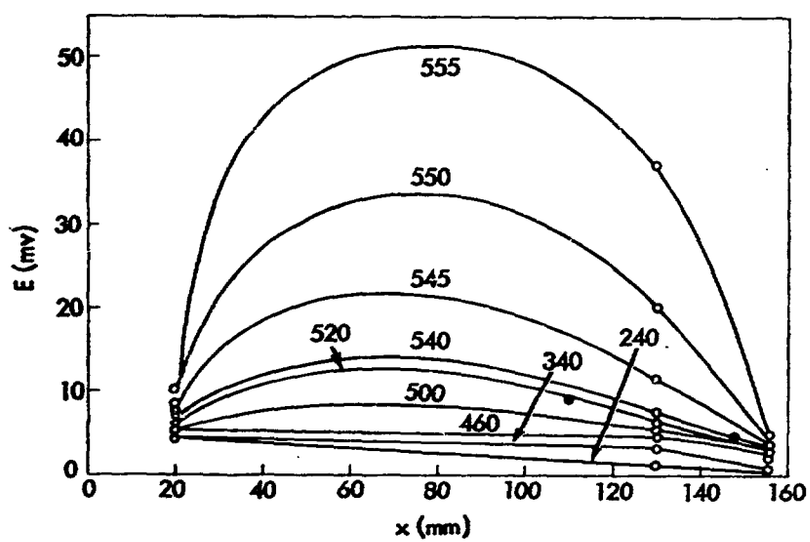

FIG. B6 STRAIN GAGE VOLTAGE - DISTANCE DATA FOR 69.8% TMD 91/9 RDX/WAX (SHOT 225) [● POSITION OF PC WAVE (AFTER 546 μsec, PC WAVE IS BEYOND 155 mm).]

production. Consequently a positive pressure gradient at 20 mm could be a natural consequence of burning in the more porous charges. However, because the maxima in Figures B-4 and B-5 only develop after the formation and propagation of the PC wave, we feel that the maxima in Figures B-4 to B-6 represent, to some degree, the effect of compaction of the porous bed [recall that compaction of the porous bed has been proposed for Shots 312, 307, and 225]. Unfortunately, there is insufficient information at present to evaluate how large or when a positive pressure gradient should arise as a result of ordinary convective burning. Consequently, the extent of the contribution to the pressure profiles in Figures B-4 to B-6 by compaction of the porous charge is unknown.

D. It has been mentioned in the text (p. 58) that the slope of the SG voltage-time (E-t) curves, at times just after the passage of the PC wave, increases with increasing x -- i.e., the PC wave front appears to sharpen as it propagates. We have measured and tabulated in Table B-5 the slope at a time shortly after the passage of the PC wave. We have selected the slope at a point on the E-t curve relative to the voltage level at the time of passage of the PC wave (E at t_{PC}). This voltage level, E_{PC}, is considered to represent voltage (pressure) due to combustion resulting from the convective wave. After t_{PC} we argue that we are observing initially the front of the PC wave. The slope of the PC wave front was measured at a voltage about 1 kbar above E_{PC} or more accurately at E_{PC} plus 5 mv.

The data in Table B-5 shows the increase in the measured slope, dE/dt, for SGs located at increasing distances from the ignitor. In addition, the tabulated results indicate that the slope dE/dt may vary with initial compaction. We were very fortunate in our selection of SG locations. If we calculate the SG location on a basis relative to the position of onset of detonation ℓ, the relative SG locations, x/ℓ, fall essentially in three groupings for all experiments: x/ℓ values of 0.36, 0.52, and 0.67. Consequently, we have plotted the data of Table B-5 as a function of initial compaction (Figure B-7) for various x/ℓ values.

From Figure B-7 it is apparent that the slope dE/dt increases with increasing x for a single compaction. However when we consider relative SG locations, we see that dE/dt increases uniformly, and perhaps linearly, with increasing initial charge density above 78% TMD. Below 78% TMD, dE/dt increases with decreasing initial charge density. The latter observation is consistent with the concept of compaction of the porous bed before the formation of the PC wave in the lower density experiments. The observation that dE/dt increases with increasing charge density means that the PC wave is being reinforced continually by reaction and pressure buildup behind the PC wave.

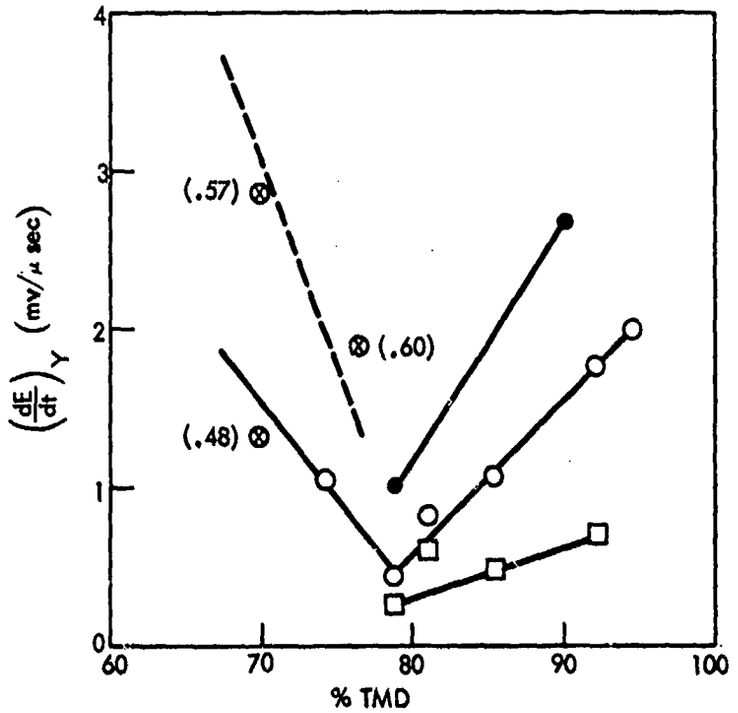

FIG. 17 VARIATION OF $(dE/dt)_Y$ NEAR FRONT OF POST-CONVECTIVE WAVE AS FUNCTION OF COMPACTION. [CURVES REPRESENT CONSTANT RATIOS OF X/ℓ □ 0.36 ○ 0.52 ● 0.67 ⊗ VARYING X/ℓ VALUES - GIVEN IN PARENTHESES. ($Y = E_{PC} + 5$ mv)]

TABLE B-1

COMPILATION OF DISTANCE-TIME DATA FOR 91/9 RDX/WAX

Density g/cc:	1.588		1.588		1.551		1.513	
%TMD:	94.5		94.5		92.3		90.1	
Shot No.:	222		304		316		215	
IP Data[a]	x	t	x	t	x	t	x	t
	41.4	0.0	28.7	0.0	41.4	0.0	41.4	0.0
	66.8	18.45	41.15	6.5	54.1	11.9	66.8	37.8
	79.5	22.9	66.55	22.45	79.5	33.4	79.5	54.3
	104.9	35.3	79.25	33.0	104.9	68.8	92.2	68.1
	130.3	45.7	104.65	49.3	130.3	91.2	117.6	87.7
	155.7	53.8	130.05	70.7	155.7	101.8	130.3	91.7
	181.1	63.8	155.45	83.0	181.1	105.0	168.4	96.5
	206.5	72.2	181.0	86.2	206.5	108.45	193.8	99.2
	231.9	80.8	206.5	89.3	231.9	111.8	219.2	102.9
	263.4	94.0	263.4	95.9	263.65	115.8	263.65	108.5
SG Data[a]	x	t_{PC}[b]	x	t_{PC}	x	t_{PC}	x	t_{PC}
	20.3	?	20.3	?	28.8	----	20.3	----
	54.4	12	79.5	43	54.0	45	206.5	----
	79.5	22	104.9	53-56	79.1	60		
	x_I	t_I[c]	x_I	t_I	x_I	t_I	x_I	t_I
	----	----	130	68.3	133	94	104	81

a) All x data are distances in mm, relative to ignitor/explosive interface. All t data are in μsec.
b) Time of PC excursion, relative to discharge of first IP (i.e., IP with smallest x value).
c) Time of large electromagnetic disturbance on SG record; associated with time of intersection of convective and PC fronts. The corresponding x value has been taken from the x - t plot of the IP and SG data (see for example Figure 5).

TABLE B-1, Cont'd.

COMPILATION OF DISTANCE-TIME DATA FOR 91/9 RDX/WAX

Density								
g/cc:	1.513		1.437		1.361		1.361	
%TMD:	90.1		85.5		81.0		81.0	
Shot No.:	305		306		220		317	
IP Data[a]	x	t	x	t	x	t	x	t
	41.3	0.0	28.7	0.0	41.4	0.0	41.4	0.0
	66.55	38.6,55.5	41.15	24.6	66.8	51.35	66.8	62.3
	79.25	54.0	54.1	45.6	79.5	83.6	79.5	89.15
	92.2	70.5	66.55	65.25	92.2	113.3	92.2	113.95
	104.65	78.5	79.25	85.8	117.6	136.4	117.5	163.4
	130.3	87.2	104.65	123.8	130.3	138.3	130.3	184.6
	155.7	90.3	130.05	156.6	168.4	144.0	168.4	226.7
	181.1	93.4	155.45	173.3	193.8	147.95	193.8	232.2
	206.5	97.4	206.5	180.4	219.2	151.4	219.2	235.6
	263.65	104.6	263.65	188.1	263.65	158.0	263.65	241.9
SG Data[a]	x	t_{PC}	x	t_{PC}	x	t_{PC}	x	t_{PC}
	20.3	23	20.2	88	20.3	----	41.7	128
	54.1	----	54.1	96			66.6	149
	79.5	63	79.8	116			92.2	170
	x_I	t_I	x_I	t_I	x_I	t_I	x_I	t_I
	92	71	122	148	----	----	----	----

a) All x data are distances in mm, relative to ignitor/explosive interface. All t data are in μsec.

TABLE B-1, Cont'd.

COMPILATION OF DISTANCE-TIME DATA FOR 91/9 RDX/WAX

Density								
g/cc:	1.324		1.286		1.248		1.248	
%TMD:	78.8		76.5		74.3		74.3	
Shot No.:	315		312		307		224	
IP Data[a]	x	t	x	t	x	t	x	t
	41.4	0.0	41.4	0.0	41.45	0.0	41.15	0.0
	66.8	65.7	66.8	65.1	66.55	83.4	66.55	100.9
	79.5	93.2	79.5	94.1	104.65	187.3	79.5	138.8
	92.1	122.3	104.9	151.3	130.05	249.6	91.95	171.9
	117.6	174.6	130.3	202.4	155.45	308.7	104.65	207.4
	130.3	201.7	155.7	250.5	181.1	365.5	130.3	269.3
	168.4	241.7	181.1	298.8	206.5	406.4	155.7	326.7
	193.8	245.3	193.8	313.4	231.9	409.5	181.1	380.8
	219.2	249.1	231.9	319.2	247.9	412.4	206.5	----
	263.65	255.6	263.65	323.9	263.5	414.3	263.4	----
SG Data[a]	x	t_{PC}	x	t_{PC}	x	t_{PC}	x	t_{PC}
	53.9	149	20.1	210	20.3	300	20.3	----
	79.9	169	79.5	240	104.9	347	105.2	----
	104.9	197	117.6	264	155.7	366-384		
	x_I	t_I	x_I	t_I	x_I	t_I	x_I	t_I
	148	235	186	310	198	398	----	----

a) All x data are distances in mm, relative to ignitor/explosive interface. All t data are in μsec.

TABLE B-1, Cont'd.

COMPILATION OF DISTANCE-TIME DATA FOR 91/9 RDX/WAX

Density g/cc:	1.172		1.13	
%TMD:	69.8		67.3	
Shot No.:	225		221	
IP Data[a]	x	t	x	t
	41.4	0.0	41.4	0.0
	66.8	93.9	66.8	78.3
	79.5	135.2	104.9	198.4
	104.9	211.1	130.3	265.1
	130.3	279.4	155.7	328.6
	155.7	344.8	181.1	386.7
	181.1	405.1	206.5	433.8
	206.5	466.2	231.9	----
	231.9	521.9	244.6	----
	263.4	----	263.6	----
SG Data[a]	x	t_{PC}	x	t_{PC}
	20.1	517	20.3	----
	130.6	532	181.6	----
	156.0	546		
	x_I	t_I	x_I	t_I
	272	606	----	----

a) All x data are distances in mm, relative to ignitor/explosive interface. All t data are in μsec.

TABLE B-2

COMPILATION OF DISTANCE-TIME DATA FOR MISCELLANEOUS EXPLOSIVES

	97/3 RDX/Wax		94/6 RDX/Wax		Ammonium Picrate	
Density						
g/cc:	1.248		1.210		1.551	
%TMD:	74.3		70.3		90.1	
Shot No:	218		214		226	
IP Data[a]	x	t	x	t	x	t
	41.4	0.0	41.4	0.0	41.4	0.0
	66.8	48.5	66.8	66.8	66.8	45.05
	79.5	68.5	79.5	95.95	79.5	93.0
	92.2	78.8	92.2	125.1	104.9	137.6
	117.6	82.9	117.6	167.7	130.3	382.3
	130.3	85.0	130.3	180.2	155.7	427.5
	168.4	90.6	168.4	186.8	181.1	471.3
	193.8	94.4	193.8	190.7	206.5	514.2
	219.2	98.05	219.2	194.6	231.9	556.5
	263.6	104.9	263.6	201.2	263.4	606.0

a) All x data are distances in mm, relative to ignitor/explosive interface. All t data are in μsec.

TABLE B-3

PARTICLE SIZE ANALYSIS OF RDX (X597)

Sieve No.	Sieve Opening (μ)	Average Particle Size (μ)	Weight % Held on Sieve	Accumulative Weight %
20	840		0.0	100.00
30	590	715	0.0	100.00
40	420	505	0.34	100.00
50	300	360	5.49	99.66
70	210	255	31.30	94.17
100	149	180	20.05	62.87
140	105	127	13.94	42.82
200	74	89.5	12.21	22.88
270	53	63.5	5.83	16.67
325	44	48.5	8.86	10.84
Pan	--	<44	1.98	1.98

Specifications for Class A RDX:

Through Sieve No.	Specifications	Experimental
20	98 ± 2	100
50	90 ± 10	94
100	60 ± 30	43
200	25 ± 20	17

TABLE B-4

MEASUREMENTS OF OUTER DIAMETER OF RECOVERED DDT TUBE (IGNITOR END)[a]

Explosive:	91/9 RDX/Wax										94/6 RDX/Wax	Ammonium Picrate
Density g/cc:	1.588	1.513	1.513	1.361	1.361	1.324	1.286	1.248	1.172	1.13	1.210	1.210
Shot No.:	304	215	305	220	317	315	312	224	225	221	214	217
Orig. Outer Dia: (in.)	2.006	2.007	2.006	2.006	2.006	2.006	2.006	2.007	2.007	2.006	2.006	2.006
Distance from Near[b] End of Tube, cm												
1		2.007	2.006	2.006	2.006	2.007	2.006	2.007	2.007	2.006	2.006	2.006
2		2.007	2.006	2.006	2.006	2.009	2.006	2.007	2.007	2.006	2.006	2.007
3		2.008	2.011	2.009	2.009	2.015	2.009	2.012	2.010	2.011	2.008	2.019
4		2.020	2.023	2.027	2.014	2.050	2.022	2.026	2.022	2.026	2.018	2.069
5		2.046	2.043	2.058	2.026	2.083	2.040	2.050	2.045	2.045	2.038	2.129
6		2.072	2.060	2.085	2.037	2.091	2.056	2.065	2.060	2.061	2.058	2.182
7		2.094	2.072	2.097	2.047	2.083	2.064	2.068	2.066	2.070	2.067	2.197
8		2.106	2.081	2.105	2.052	2.069	2.062	2.061	2.064	2.069	2.068	2.184
9		2.111	2.086		2.056	2.069	2.059	2.052	2.052	2.062		2.140
10		2.120	2.108		2.058	2.076	2.053	2.036	2.038	2.047		2.092
11					2.062	2.093	2.053	2.026	2.024	2.053		2.056
12					2.067	2.114	2.061	2.022	2.018	2.023		2.039
13					2.079		2.075	2.024	2.012	2.018		2.028
14					2.102		2.092	2.036	2.012	2.017		2.028
15							2.116	2.058	2.018	2.018		2.029
16								2.080	2.034	2.025		2.030
17									2.054	2.039		2.034
18									2.076	2.058		2.039
19									2.096	2.081		2.044
20										2.106		2.048
21										2.127		2.051
22												2.054
23												2.050
24												2.049
25												2.046
26												2.040

a) Due to splitting of some tubes, it was not possible to measure the ID of the recovered ignitor fragment for all shots.

b) Ignitor/explosive interface at 47.5 mm, relative to this edge.

TABLE B-5

MEASURED VALUES OF dE/dt ASSOCIATED WITH THE FRONT OF THE PC WAVE FOR 91/9 RDX/WAX

Density (% TMD)	Shot No.	SG Location x (mm)	x/ℓ	E_{PC} (mv)	$(dE/dt)_Y^*$ mv/μsec	SG Location x (mm)	x/ℓ	E_{PC} (mv)	$(dE/dt)_Y^*$ mv/μsec
94.5	304	20.3	.131	?	----	79.5	.513	3.0	2.0
92.3	316					54.0	.372	4.5	0.71
90.1	305	20.3	.169	10.5	0.70				
85.5	306	20.2	.131	7.5	0.51	54.1	.350	4.0	0.50
81.0	317	41.7	.239	5.0	0.41	66.6	.381	2.7	0.63
78.8	315	53.9	.348	7.0	0.27	79.9	.516	4.5	0.45
76.5	312	20.0	.103	5.5	0.59	79.5	.409	5.0	0.65
74.3	307	20.3	.097	5.5	0.37	104.9	.500	3.5	1.05
69.8	225	20.1	.073	6.0	0.67	130.6	.475	6.0	1.33

* $Y = E_{PC} + 5$ mv (i.e., about 1 kbar above E_{PC}).

TABLE B-5, Cont'd.

MEASURED VALUES OF dE/dt ASSOCIATED WITH THE FRONT OF THE PC WAVE FOR 91/9 RDX/WAX

Density (% TMD)	Shot No.	SG Location x (mm)	x/ℓ	E_{PC} (mv)	$(dE/dt)_Y^*$ mv/μsec
94.5	304	104.9	.677	-2.5	2.2_2
92.3	316	79.1	.546	3.5	1.7_8
90.1	305	79.5	.663	3.0	2.6_7
85.5	306	79.8	.516	2.5	1.0_8
81.0	317	92.2	.528	2.5	0.82
78.8	315	104.9	.677	3.0	1.0_0
76.5	312	117.6	.602	3.5	1.9_0
74.3	307	155.7	.741	0.5	6.6_7
69.8	225	156.0	.567	3.5	2.8_6

* $Y = E_{PC} + 5$ mv (i.e., about 1 kbar above E_{PC}).

TABLE B-6

TIME INTERVAL BETWEEN PASSAGE OF CONVECTIVE FRONT AND PC WAVE AT VARIOUS LOCATIONS FOR 91/9 RDX/WAX

Density (% TMD)	Shot No.	$(t_E)_{41}$ μsec	$(t_E)_{80}$ μsec	$(t_E)_{\ell/2}$ μsec
94.5	304	18	10	10
92.3	316	37	20	25
90.1	305	40	9	21
85.5	306	57	30	30
81.0	317	133	72	61
78.8	315	134	76	76
76.5	312	217	146	114
74.3	307	312	208	161
69.8	225	485	370	253

APPENDIX C

PERMEABILITY MEASUREMENTS OF GRANULAR EXPLOSIVES

A. Andreev and Chuiko (16) measured the permeability coefficients for various explosives as a function of compaction and particle size. Their permeability coefficient, η, was the coefficient relating "the quantity of air filtered under laminar conditions through one cm^2 cross-section in one sec with unit pressure drop per cm" (16). The dimensions of η are $cm^2\ [mm(Hg)]^{-1}\ sec^{-1}$.

η is related to the Darcy equation [equation (6)] through the relationship

$$\eta = B_o/\mu \qquad \text{C-1}$$

where B_o is the permeability coefficient in cm^2
μ is the viscosity of the air, 1.80×10^{-4} g/cm sec

Andreev and Chuiko used cgs units for the Darcy equation except for dp which they gave in mm(Hg). Thus, equation C-1 yields values of B_o in cm^2 when corrections are made for the different units of pressure and the incorporation of the viscosity term.

$$B_o(cm^2) = \eta\mu = \eta \cdot \frac{cm^2}{mm(Hg)sec} \times \frac{7.50 \times 10^{-4}\ mm(Hg)}{1\ dyne/cm^2} \times$$

$$1.80 \times 10^{-4} \frac{g}{cm\ sec} = 13.5 \times 10^{-8}\ \eta \qquad \text{C-2}$$

We have used a reproduction of Figure 1 from reference 16. The abscissa is relative density which is %TMD/100. We have read on the telereader the individual experimental data points as shown in that figure and also selected points along the solid lines drawn by the authors. These data are listed in Table C-1 only for densities above 30 %TMD. The values of B_o were calculated from the $1/\eta$ values using equation C-2.

TABLE C-1

DEPENDENCE OF PERMEABILITY COEFFICIENT ON COMPACTION
(Data From Reference 16)

CURVE 1 -- MICROCRYSTALLINE MATERIALS

Experimental Data			Selected Points on Authors' Line		
%TMD	$1/\eta$	$B_o \times 10^8$ (cm^2)	%TMD	$1/\eta$	$B_o \times 10^8$ (cm^2)
32.4	14.3	0.944	31.3	11.8	1.14
32.1	19.0	0.711	34.0	16.6	0.813
35.4	17.4	0.776	36.6	23.3	0.579
35.9	19.1	0.707	38.9	30.9	0.437
39.8	26.1	0.517	42.0	44.3	0.305
40.5	34.2	0.395	44.3	58.1	0.232
40.2	47.7	0.283	46.7	79.2	0.170
48.4	80.8	0.167	50.0	118	0.114
48.0	96.2	0.140	52.4	158	0.0854
53.3	135	0.100	56.2	249	0.0542
52.9	179	0.0754	58.9	346	0.0390
53.8	215	0.0628	61.1	455	0.0297
59.1	204	0.0662	66.0	810	0.0167
61.7	506	0.0267			

CURVE 2 -- TETRYL 130 μ

48.2	0.485	27.8	46.6	0.375	36.0
53.6	0.863	15.6	49.3	0.614	22.0
54.7	1.64	8.23	54.1	1.45	9.31
60.0	3.93	3.44	58.5	3.33	4.05
65.2	12.0	1.12	63.0	7.45	1.81
			68.6	21.4	0.631

CURVE 3 -- POLYDISPERSE RDX

63.8	2.70	5.01	61.4	1.66	8.13
65.9	4.00	3.38	63.1	2.35	5.74
65.9	5.06	2.67	64.7	3.33	4.05
69.0	7.41	1.82	66.7	5.11	2.64
70.1	8.49	1.59	68.0	6.60	2.05
70.9	15.1	0.896	70.0	9.97	1.35
			74.0	22.8	0.592

TABLE C-1, Cont'd.

CURVE 4 -- PETN 200 μ

Experimental Data			Selected Points on Authors' Line		
%TMD	1/η	$B_o \times 10^8$ (cm^2)	%TMD	1/η	$B_o \times 10^8$ (cm^2)
57.8	0.530	25.5	54.8	0.243	55.6
59.4	0.6765	20.0	58.9	0.592	22.8
66.7	2.56	5.28	65.3	2.44	5.53
68.5	4.58	2.95	69.9	6.65	2.03
76.3	31.8	0.424	74.1	16.9	0.799
80.7	70.9	0.190	76.4	27.9	0.484
			81.1	77.7	0.174
			85.0	184	0.0734

CURVE 6 -- PETN 360 μ

60.2	0.201	67.2	60.8	0.228	59.2
68.1	1.06	12.7	64.0	0.514	26.3
70.9	3.05	4.42	69.7	2.31	5.84
74.1	6.47	2.085	74.3	7.64	1.77
76.2	14.9	0.908	76.1	11.9	1.13
79.4	28.5	0.474	78.3	21.2	0.637
81.9	49.3	0.274	82.1	54.7	0.247
86.7	176	0.0769	83.9	84.7	0.159
			86.2	152	0.0888
			88.1	235	0.0574

CURVE 7 -- PETN 510 μ

64.1	0.187	72.4	63.6	0.168	80.4
69.7	0.624	21.6	66.2	0.364	37.1
71.0	1.19	11.4	71.8	1.81	7.46
73.7	2.95	4.57	73.2	2.67	5.06
76.6	8.31	1.63	76.5	7.23	1.87
79.5	24.1	0.559	78.9	14.1	0.957
83.4	55.4	0.244	80.5	22.4	0.603
84.2	62.9	0.215	84.7	75.4	0.179
			86.0	105	0.129

TABLE C-1, Cont'd.

CURVE 8 -- PETN 730 μ

Experimental Data			Selected Points on Authors' Line		
%TMD	$1/\eta$	$B_o \times 10^8$ (cm^2)	%TMD	$1/\eta$	$B_o \times 10^8$ (cm^2)
66.2	0.225	60.1	66.8	0.163	82.8
73.9	1.42	9.52	69.3	0.372	36.3
75.3	2.54	5.31	73.3	1.27	10.6
79.8	10.9	1.24	75.0	2.25	6.00
83.6	16.6	0.815	79.7	10.0	1.35
83.4	30.8	0.438	82.9	26.3	0.513
86.3	68.0	0.198	84.1	37.1	0.364
88.4	173	0.0782	86.5	79.0	0.171
			90.0	233	0.0579

B. Andreev and Gorbunov (27) reported a few permeability coefficients for a variety explosives. The authors used the same units as Andreev and Chuiko (16) except that their time interval was 60 seconds. Andreev and Gorbunov (27) reported their data in terms of a specific resistance, r, whose units were mm(Hg)cm^{-3}.

$$r = \frac{\Delta p}{V} \qquad \text{C-3}$$

From equation (6), we note that

$$r = \frac{dp}{V} = \frac{\mu}{B_o}\frac{dx}{At} \qquad \text{C-4}$$

Since dx = 1 cm, A = 1 cm^2 and t = 60 sec

$$r = \frac{\mu}{60\ B_o}\frac{1}{\text{cm sec}}$$

or

$$B_o = \frac{\mu}{60\ r[\text{mm(Hg)/cm}^3]}\frac{1}{\text{cm sec}}$$

$$= \frac{\mu}{60\,r}\frac{\text{cm}^2}{\text{mm(Hg)sec}}$$

Changing pressure units to cgs units and using $\mu = 1.8 \times 10^{-4}$ g/cmsec produces

$$B_o = \frac{(1.8 \times 10^{-4})(7.50 \times 10^{-4})}{60\ r} = \frac{0.225 \times 10^{-8}}{r}\ (\text{cm}^2) \qquad \text{C-5}$$

Table C-2 contains the experimental values of r and the calculated values of B_o.

TABLE C-2

PERMEABILITY COEFFICIENTS FOR MISCELLANEOUS EXPLOSIVES
(Data From Reference 27)

Explosive	%TMD	Particle Size μ	$r\left(\frac{mm(Hg)}{cm^3}\right)$	B_o (cm^2)
TNT	73	50-60	5.8	3.88×10^{-10}
	67	50-60	2.5	9.00×10^{-10}
Picric Acid	81	10-20	21	1.07×10^{-10}
RDX	93	50-60	110	2.05×10^{-11}
PETN	82	10	400	6.625×10^{-12}
Mercury Fulminate	89	50-100	1900	1.18×10^{-12}

C. Belyaev et al (7) reported some permeability measurements for PETN, TNT and a TNT/NH_4ClO_4 mixture. The authors provided very little information about their experimental arrangement. Since their permeability coefficient, k, is reported in darcies, the calculation of values of B_o from their data is straightforward. As before, we used a reproduction of Figure 6 from reference 7. The abscissa is porosity, m, which is related to %TMD by the relationship, m = 1 - %TMD/100. The individual data points were read on the telereader and these, in addition to the corresponding $B_o(cm^2)$ values, are listed in Table C-3.

D. Discussion of Permeability Coefficients Measurements

The most comprehensive study of permeability coefficients for explosives was made by Andreev and Chuiko (16). Their data (see Table C-1 and Ref. (16)) show that (a) the permeability decreases with decreasing particle size for a given relative density (%TMD) of an explosive (b) the permeabilities of microcrystalline explosives (e.g. 5μ particle size) are essentially identical for a given compaction (c) the relationship between log $1/B_o$ and relative density is linear in the region from 50 - 85 %TMD for particle sizes at least greater than 130 μ and (d) the slope, $d(\log 1/B_o)/d(\%TMD)$, decreases with decreasing particle size.

TABLE C-3

PERMEABILITY COEFFICIENTS FOR MISCELLANEOUS EXPLOSIVES
(Data From Reference 7)

CURVE 1 PETN 10 - 20 μ

%TMD	-log K	K (darcy)	B_o (cm^2)
85.1	3.26	5.45×10^{-4}	5.37×10^{-12}
87.5	3.51	3.12×10^{-4}	3.08×10^{-12}
90.0	3.90	1.25×10^{-4}	1.23×10^{-12}
92.6	4.68	2.07×10^{-5}	2.05×10^{-13}
95.1	6.01	9.77×10^{-7}	9.64×10^{-15}

CURVE 2 TNT/NH_4ClO_4 10 - 20 μ

87.0	3.23	5.82×10^{-4}	5.75×10^{-12}
90.0	3.71	1.94×10^{-4}	1.91×10^{-12}
92.6	4.37	4.29×10^{-5}	4.23×10^{-13}
95.1	5.50	3.16×10^{-6}	3.12×10^{-14}

CURVE 3 TNT 10 - 20 μ

87.9	3.08	8.33×10^{-4}	8.22×10^{-12}
90.0	3.49	3.22×10^{-4}	3.18×10^{-12}
92.5	4.12	7.59×10^{-5}	7.49×10^{-13}
95.1	5.18	6.66×10^{-6}	6.57×10^{-14}
96.0	6.04	8.93×10^{-7}	8.81×10^{-15}

CURVE 4 PETN 550 μ

91.5	3.05	8.95×10^{-4}	8.84×10^{-12}
92.5	3.26	5.48×10^{-4}	5.41×10^{-12}
95.0	4.06	8.65×10^{-5}	8.53×10^{-13}
96.2	4.60	2.48×10^{-5}	2.45×10^{-13}
97.1	5.45	3.52×10^{-6}	3.48×10^{-14}

The permeability data for PETN are very interesting and important for the analysis of DDT mechanisms. Unfortunately, the two sets of data for PETN, one from Andreev et al (16,27) and the other from Belyaev at al (7), do not overlap. However, there is one data point for 10 μ PETN as measured by Andreev and Gortunov (27) which can be compared with the 10 - 20 μ PETN data of Belyaev. In Table C-2, the B_o value, 5.6×10^{-12} cm^2, for 10 μ PETN at 82% TMD compares quite favorably with the 10 - 20 μ PETN data as listed in Table C-3 for Curve 1. This agreement gives added weight to the validity for the curves which were drawn in Figure 36, joining the two sets of data.